

Nataliya Strokina

## **MACHINE VISION METHODS FOR PROCESS MEASUREMENTS IN PULPING**

Thesis for the degree of Doctor of Science (Technology) to be presented with due permission for public examination and criticism in the Auditorium 1382 at Lappeenranta University of Technology, Lappeenranta, Finland on the 15th of November, 2013, at noon.

Acta Universitatis  
Lappeenrantaensis 543

- Supervisors Professor Heikki Kälviäinen  
Assistant Professor Lasse Lensu  
Dr. Tech. Tuomas Eerola
- Machine Vision and Pattern Recognition Laboratory (MVPR)  
Department of Mathematics and Physics  
LUT School of Technology  
Lappeenranta University of Technology  
Finland
- Reviewers Distinguished Professor Josef Kittler  
Department of Electronic Engineering  
University of Surrey  
United Kingdom
- Professor Risto Ritala  
Department of Automation Science and Engineering  
Tampere University of Technology  
Finland
- Opponents Distinguished Professor Josef Kittler  
Department of Electronic Engineering  
University of Surrey  
United Kingdom
- Professor Risto Ritala  
Department of Automation Science and Engineering  
Tampere University of Technology  
Finland

ISBN 978-952-265-493-9  
ISBN 978-952-265-494-6 (PDF)  
ISSN-L 1456-4491  
ISSN 1456-4491

Lappeenrannan teknillinen yliopisto  
Yliopistopaino 2013

*To my dearest parents.*



## Preface

The research presented in this dissertation was carried out in the PulpVision project between 2010 and 2013. The project was a joint effort of the Machine Vision and Pattern Recognition Laboratory at Lappeenranta University of Technology, the FiberLaboratory at the Mikkeli University of Applied Sciences, Center for Measurement and Information Systems (CEMIS-OULU) at the University of Oulu, and the Color Research Laboratory at the University of Eastern Finland.

This thesis would not have been possible without the guidance of my supervisors Professor Heikki Kälviäinen, Assistant Professor Lasse Lensu, and Dr. Tech. Tuomas Eerola. Thank you, first of all, for teaching me by example what it means to carry out scientific research. You encouraged me to extend my knowledge, develop my skills, and think more widely searching for solutions. With patience you treated my new ideas and helped in their implementation. Thank you for pointing out important aspects and motivating me to concentrate and get things done.

I wish to express my gratitude to the pre-examiners Distinguished Professor Josef Kittler and Professor Risto Ritala for their valuable comments to improve the manuscript.

I would like to thank the whole MVPR laboratory, both former and present members, for the warm atmosphere and help: Lauri Laaksonen, Ekaterina Riabchenko, Jukka Lankinen, Ekaterina Nikandrova, Dr. Teemu Kinnunen, Professor Ville Kyrki, Tatiana Kurakina, Mikhail Sorokin, Dr. Leena Ikonen, Assistant Professor Arto Kaarna, and Dr. Jarmo Ilonen. Special thanks to Tarja Nikkinen, Ilmari Laakkonen, Petri Hautaniemi, Paula Haapanen, and Anne Makkonen for great support in solving organizational and technical problems.

Starting from April 2011, there has been an ongoing collaboration with the Center for Machine Perception (CMP) in Czech Technical University in Prague which influenced my doctoral research considerably. It was a precious experience to stay in a new environment and to work with a group of talented and devoted scientists. I would like to express gratitude to Professor Jiří Matas who was co-supervising me during the research stay at the CMP. You shared with us your enthusiasm and special view on the research tasks making me think outside the box. Thanks to the members of the laboratory who created a fruitful atmosphere for development: Eva Matysková, Professor Václav Hlaváč, Pavla Marešová, Radka Kopecká, Dr. Ondra Chum, Dr. Michal Perd'och, Dr. Hongping Cai, Dr. Filip Korč, Michal Bušta, Dmytro Mishkin, Andrej Mikulík, James Pritts, Kostiantyn Antoniuk, Matěj Šmíd, Michal Uříčář, and Tomáš Vojří.

Thanks to the Image and Video Processing Group of Brno University of Technology for their collaboration, especially to Professor Pavel Zemčík, Associate Professor Adam Herout, Dr. Roman Juránek, and Martin Musil.

For financial support I would like to thank PulpVision project partners, Finnish Funding Agency for Technology and Innovation (TEKES), European Union, Andritz AG, Wetend Technologies Ltd., Oy LabVision Technologies Ltd., Janesko Oy, Diranet Oy/Savled Oy, Pixact Ltd., Cavitar Ltd., and Teknosavo Oy. For partial financial support in 2013 I would like to acknowledge the East Finland Graduate School in Computer Science and Engineering (ECSE). In 2012, the research was partially supported by the Finnish Foundation for Technology Promotion (TES). In 2011, the Finnish Cultural Foundation made it possible to start a productive collaboration with the Center

for Machine Perception at the Czech Technical University in Prague.

Separately I would like to thank people who provided the data and the expert knowledge about the application area: Aki Mankki, Heikki Mutikainen, Dr. Jari Käyhkö, and Dr. Tapio Tirri from the FiberLaboratory, Dr. Kaarina Prittinen, and Kyösti Karttunen from CEMIS-Oulu.

During these years I was surrounded by great people. They inspired, motivated me, and helped a lot in professional and private matters. Thank you very much my dear friends!

Finally, I would like to thank my wonderful family for their unconditioned and limitless love.

Lappeenranta, November 2013

*Nataliya Strokina*

## Abstract

Nataliya Strokina

### **Machine vision methods for process measurements in pulping**

Lappeenranta, 2013

97 p.

Acta Universitatis Lappeenrantaensis 543

Diss. Lappeenranta University of Technology

ISBN 978-952-265-493-9

ISBN 978-952-265-494-6 (PDF)

ISSN 1456-4491

The papermaking industry has been continuously developing intelligent solutions to characterize the raw materials it uses, to control the manufacturing process in a robust way, and to guarantee the desired quality of the end product. Based on the much improved imaging techniques and image-based analysis methods, it has become possible to look inside the manufacturing pipeline and propose more effective alternatives to human expertise. This study is focused on the development of image analyses methods for the pulping process of papermaking. Pulping starts with wood disintegration and forming the fiber suspension that is subsequently bleached, mixed with additives and chemicals, and finally dried and shipped to the papermaking mills. At each stage of the process it is important to analyze the properties of the raw material to guarantee the product quality.

In order to evaluate properties of fibers, the main component of the pulp suspension, a framework for fiber characterization based on microscopic images is proposed in this thesis as the first contribution. The framework allows computation of fiber length and curl index correlating well with the ground truth values. The bubble detection method, the second contribution, was developed in order to estimate the gas volume at the delignification stage of the pulping process based on high-resolution in-line imaging. The gas volume was estimated accurately and the solution enabled just-in-time process termination whereas the accurate estimation of bubble size categories still remained challenging. As the third contribution of the study, optical flow computation was studied and the methods were successfully applied to pulp flow velocity estimation based on double-exposed images. Finally, a framework for classifying dirt particles in dried pulp sheets, including the semisynthetic ground truth generation, feature selection, and performance comparison of the state-of-the-art classification techniques, was proposed as the fourth contribution. The framework was successfully tested on the semisynthetic and real-world pulp sheet images. These four contributions assist in developing an integrated factory-level vision-based process control.

Keywords: image processing and analysis, machine vision, papermaking, pulping, fiber segmentation, bubble detection, dirt classification, flow analyses, ground truth

UDC 004.932.2:004.93'1:630\*86:621.397.3

|            |  |
|------------|--|
| CCA        | Concentric Circular Arrangements                                     |
| CCD        | Charged-Coupled Device   |
| CEMIS-OULU | Center for Measurement and Information Systems of University of Oulu |
| CHT        | Circular Hough Transform   |
| CPU        | Central Processing Unit  |
| FN         | False Negative   |
| FP         | False Positive   |
| FQA        | Fiber Quality Analyzer   |
| GMM        | Gaussian Mixture Model   |
| GMMem      | Gaussian Mixture Model with expectation maximization                 |
| GMMfj      | Gaussian Mixture Model with Figueiredo-Jain criteria                 |
| GT         | Ground Truth   |
| HS         | Horn and Schunk method   |
| HSI        | Hue, Saturation, Intensity color space                               |
| HT         | Hough Transform  |
| IPIP       | Interrogation Particle Image Pattern                                 |
| ISO        | International Organization for Standardization                       |
| K-NN       | K-Nearest Neighbor classifier  |
| LBP        | Local Binary Patterns  |
| LDA        | Laser Doppler Anemometry   |
|            | Linear Discriminative Analysis                                       |
| MRF        | Markov Random Field  |
| NMRI       | Nuclear Magnetic Resonance Imaging                                   |
| PC         | Personal Computer  |
| PIP        | Particle Image Pattern   |
| PIV        | Particle Image Velocimetry   |
| PTV        | Particle Tracking Velocimetry  |
| RANSAC     | Random Sample Consensus  |
| RBF        | Radial Basis Function  |
| RGB        | Red, Green, Blue colour space  |
| SCAN       | System Centered Analysis   |
| SPIP       | Search Particle Image Pattern  |
| Std        | Standard deviation   |
| SVM        | Support Vector Machine   |
| TAPPI      | Technical Association of the Pulp and Paper Industry                 |
| TP         | True Positive  |
| TPR        | True Positive Rate   |
| TPS        | Thin Plate Spline  |
| UVP        | Ultrasound Velocity Profiling  |

|          |  |           |
|----------|--|-----------|
| <b>1</b> | <b>Introduction</b>  | <b>11</b> |
| 1.1      | Research questions . . . . .   | 11        |
| 1.2      | Contributions and publications . . . . .                                 | 13        |
| 1.3      | Structure of the thesis . . . . .  | 14        |
| <b>2</b> | <b>Pulping measurements and machine vision</b>                           | <b>17</b> |
| 2.1      | Pulping process . . . . .  | 17        |
| 2.2      | Pulping process measurements . . . . .                                   | 18        |
| 2.2.1    | Pulp suspension measurements . . . . .                                   | 19        |
| 2.3      | Machine vision . . . . .   | 22        |
| 2.4      | Existing solutions . . . . .   | 23        |
| 2.5      | Summary . . . . .  | 25        |
| <b>3</b> | <b>Fiber detection and characterization</b>                              | <b>27</b> |
| 3.1      | Problem statement and previous work . . . . .                            | 27        |
| 3.2      | Fiber detection framework . . . . .                                      | 28        |
| 3.2.1    | Oriented edge map computation . . . . .                                  | 28        |
| 3.2.2    | Pixel saliency estimation . . . . .                                      | 29        |
| 3.2.3    | Pixel polarity estimation . . . . .                                      | 29        |
| 3.2.4    | Linking and fiber separation . . . . .                                   | 30        |
| 3.2.5    | Fiber characterization . . . . .   | 32        |
| 3.3      | Experiments and discussion . . . . .                                     | 33        |
| 3.3.1    | Data and results evaluation . . . . .                                    | 33        |
| 3.3.2    | Results and discussion . . . . .   | 34        |
| 3.4      | Summary . . . . .  | 37        |
| <b>4</b> | <b>Gas volume estimation in pulp suspension</b>                          | <b>41</b> |
| 4.1      | Problem statement and previous work . . . . .                            | 41        |
| 4.1.1    | Geometry-based approaches . . . . .                                      | 43        |
| 4.1.2    | Appearance-based approaches . . . . .                                    | 44        |
| 4.1.3    | Drawbacks of the existing methods . . . . .                              | 44        |
| 4.2      | Detection of bubbles as Concentric Circular Arrangements (CCA) . . . . . | 44        |
| 4.2.1    | Oriented edge map computation . . . . .                                  | 45        |
| 4.2.2    | CCA hypothesis generation, optimization, and selection . . . . .         | 46        |
| 4.3      | Experiments and discussion . . . . .                                     | 48        |
| 4.3.1    | Gas volume estimation in the pulp bleaching process . . . . .            | 48        |
|          | Data and method performance evaluation . . . . .                         | 48        |
|          | Results and discussion . . . . .   | 51        |
| 4.3.2    | Gas volume estimation with a sliding window approach . . . . .           | 53        |
| 4.3.3    | CCA performance on oil dispersion images . . . . .                       | 55        |
| 4.3.4    | Wet foam images with dense dispersion . . . . .                          | 57        |
| 4.4      | Summary . . . . .  | 57        |
| <b>5</b> | <b>Pulp flow characterization</b>  | <b>59</b> |

|          |   |           |
|----------|---|-----------|
| 5.1      | Problem statement and previous work . . . . .   | 59        |
| 5.2      | Pulp flow velocity estimation . . . . .   | 61        |
| 5.2.1    | Estimation of the global displacement . . . . .   | 61        |
| 5.2.2    | Estimation of the local displacement . . . . .  | 61        |
| 5.3      | Synthetic data generation . . . . .   | 64        |
| 5.4      | Experiments and discussion . . . . .  | 65        |
| 5.4.1    | Synthetic data . . . . .  | 65        |
| 5.4.2    | Real world test data . . . . .  | 66        |
| 5.5      | Summary . . . . .   | 67        |
| <b>6</b> | <b>Dirt particle detection and classification in dried pulp sheets</b>  | <b>69</b> |
| 6.1      | Problem statement and previous work . . . . .   | 69        |
| 6.2      | Framework for developing dirt particle classification . . . . .   | 71        |
| 6.2.1    | Workflow description . . . . .  | 71        |
| 6.3      | Semisynthetic ground truth generation . . . . .   | 72        |
| 6.3.1    | Segmenting images of sheets with dirt . . . . .   | 72        |
| 6.3.2    | Background generation . . . . .   | 73        |
| 6.3.3    | Inclusion of dirt particles . . . . .   | 73        |
| 6.4      | Dirt features and their use in classification . . . . .   | 74        |
| 6.4.1    | Feature extraction and evaluation . . . . .   | 74        |
| 6.4.2    | Classification methods . . . . .  | 75        |
| 6.5      | Experiments and discussion . . . . .  | 76        |
| 6.5.1    | Data and performance evaluation . . . . .   | 76        |
| 6.5.2    | The semisynthetic data and the statistical evaluation of the generated back-<br>ground . . . . .                                | 76        |
| 6.5.3    | The effect of the semisynthetic procedure on segmentation . . . . .   | 77        |
| 6.5.4    | Dirt classification and the effect of the semisynthetic procedure on clas-<br>sification . . . . .                              | 78        |
| 6.5.5    | Method performance introducing an unknown dirt type . . . . .   | 80        |
| 6.5.6    | Segmentation and classification of dirt particles in the real pulp sheets<br>based on the semisynthetic training data . . . . . | 81        |
| 6.6      | Summary . . . . .   | 83        |
| <b>7</b> | <b>Discussion and future work</b>   | <b>85</b> |
| 7.1      | Methods and results . . . . .   | 85        |
| 7.2      | Future work . . . . .   | 87        |
| 7.2.1    | Fiber characterization . . . . .  | 87        |
| 7.2.2    | Gas volume estimation . . . . .   | 87        |
| 7.2.3    | Pulp flow characterization . . . . .  | 88        |
| 7.2.4    | Dirt particle classification . . . . .  | 88        |
| <b>8</b> | <b>Conclusion</b>   | <b>89</b> |
|          | <b>Bibliography</b>   | <b>90</b> |

To optimize its production processes, the pulp- and papermaking industry is searching for intelligent solutions to assess and control product quality. Optimization, in this context, can be defined as building resource-efficient and environmentally sound production with known quality, using less raw material, water, and energy. This optimization is not easy since the pulp- and papermaking process consists of a large number of stages where the treatment of the material can have a significant impact on the properties of the final product. Therefore, it is important to know how the important characteristics of the product are formed at each stage.

The properties of pulp and paper are traditionally evaluated in a laboratory where the procedures follow the standards related to quality control and the properties of the raw material or end-product are measured from samples taken from the process [55]. Since traditional quality control is time-consuming and does not allow the direct control of the production process, the industry is interested in transferring the laboratory measurements to the in-line process. In this scenario, the measurements of the material will be taken directly during the process to reduce the delay in obtaining quantitative quality information and even enable real-time process control. Real-time in this context mean that depending on the process, the time between the event and the action is restricted. The amount of produced pulp and paper on the industrial scale is considerable, since the in-line solution can offer significant benefits for the industry, allowing it to adjust the process according to the information obtained from the process measurement. This would considerably reduce the risk of producing a large amount of products with undesired properties. However, difficult conditions and large variation of material properties in pipelines make the development of the in-line solutions challenging.

## **1.1 Research questions**

The focus of this thesis is the development of machine vision-based methods for analysis and understanding of the images from the pulping process. Provided an image or video as an input, the machine vision method processes it to enhance its quality, detect wanted and unwanted matter, and obtain the statistical description of the data. The data were provided by the FiberLaboratory of

Mikkeli University of Applied Sciences and the Center for Measurement and Information Systems (CEMIS-OULU) at the University of Oulu. The FiberLaboratory offers the facilities and the environment for the experimental research work on the pulp suspension at the mill and the pilot scale. CEMIS-OULU focuses on measurements in the mining, the renewable chemical, and the forestry industries.

In this thesis, there are four main directions in which the research was carried out, including (i) fiber characterization in pulp suspension, (ii) gas volume estimation at the bleaching stage of pulping, (iii) pulp flow characterization, and (iv) dirt particle classification in dried pulp sheets. The collaborating laboratories provided data and expert knowledge on the above mentioned topics. The data included the novel data from the industrial process as well as the images obtained in laboratory conditions simulating industrial processes. Example images can be seen in Fig. 1.1. Since some data, for instance, gas dispersion from bleaching (see Fig. 1.1(b)), was never obtained before, the results of computer vision methods help the papermaking specialists to understand the phenomena.

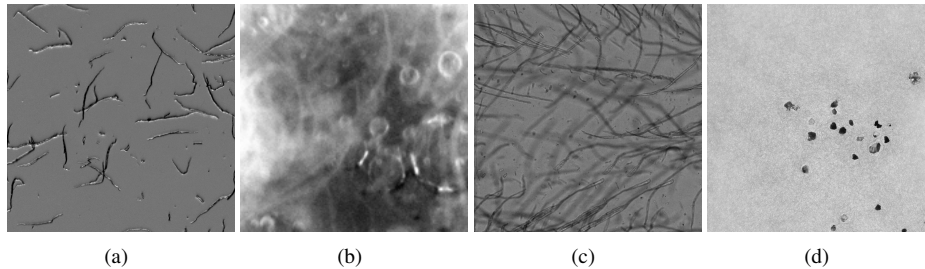


**Figure 1.1:** Examples of the pulping process data: (a) Pulp suspension for fiber characterization (CEMIS-OULU); (b) Pulp suspension at bleaching stage for gas volume estimation (FiberLaboratory); (c) A double-exposure image of pulp suspension for flow characterization (CEMIS-OULU); (d) Dried pulp sheet for dirt classification (FiberLaboratory).

The following research questions were addressed:

- Q1: What machine vision methods can assist in understanding the data from the pulping stages in the four main research directions: fiber characterization, gas volume estimation, pulp flow analysis, and dirt classification?
- Q2: In each of the tasks, how can the problem of the ground truth be solved: is there a reference measurement or can an expert provide the data? If not, is it worthwhile to generate the ground truth automatically?
- Q3: What are the limitations of the developed methods?

The following research tasks were carried out for each of the four main research directions:

- understanding the material visual properties, imaging technology, and evaluation of imaging performance,

- development of the proper methods for image preprocessing and image restoration,
- development of the appropriate methods to detect, track, and classify visible particles, and
- appropriate methods to characterize the material or process.

## 1.2 Contributions and publications

As illustrated in Fig. 1.2, pulping consists of several stages at which wood is chemically and mechanically processed. In the beginning, wood is chipped and transformed into a pulp suspension that is subsequently washed, bleached, and finally dried to be transported to a paper mill [28]. In this thesis, both images from the pulp suspension and dried pulp sheets were analyzed. The research was carried out in four main directions: fiber characterization in pulp suspension, gas volume estimation at the bleaching stage, pulp flow characterization, and dirt particle classification in dried pulp sheets. The developed methods were reported in one journal article [86] and in five conference papers [83, 85, 52, 87, 84]. All the publications are published in peer reviewed forums with an international referee practice. The Machine Vision and Applications journal holds an impact factor.

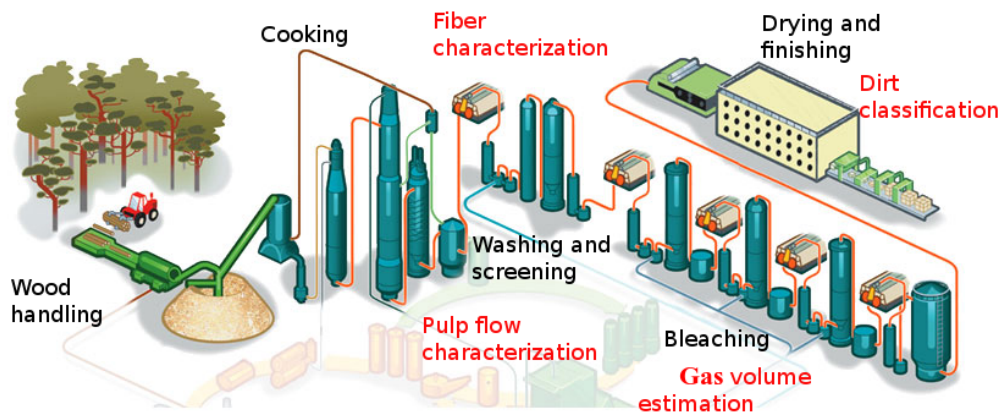


**Figure 1.2:** Pulping process, modified from [73]. The thesis contributions are marked in red.

The main contributions are summarized as follows:

1. **Fiber characterization.** The main raw material used in pulping is pulp suspension that is a diluted mixture of wood fibers, chemicals, and other additives. Measuring the properties of pulp suspension (e.g., length/width distribution of fibers) allows the operator to check the quality of material which later affects the quality of the end product [55]. Therefore, fiber characterization is one of the most important contributions of the thesis. In [84], the method of fiber detection and characterization was introduced based on the preliminary experiments in [50]. The fiber length/width distribution and curl index were estimated from the detected fibers. The preliminary experiments on image enhancement and fiber segmentation were performed in [51] and were reported in [52].

2. **Gas volume estimation.** At the delignification stage that precedes bleaching, gas is fed into the fiber suspension that manifests as bubbles in the images. Gas volume in pulp suspension, estimated here from the size and number of detected bubbles, is an important factor in the decision to terminate the bleaching stage of the papermaking process [12]. This has the potential for significant economic impact as the just-in-time termination of the pulp bleaching process saves energy and raw materials considerably. The method for gas volume estimation was introduced first in [87] and later the work was extended by including a review of related works, experiments on an extended set of pulp suspension images, and experiments on two additional data sets: oil dispersion and wet foam images.
3. **Pulp flow characterization.** The information about the fiber suspension flow is useful in the development of the pulping equipment. It can also signal the malfunctioning of the production line. As preliminary research in this thesis, two correlation-based methods were compared to compute the 2D dense velocity vector field of the pulp suspension from the double-exposed images. A framework utilizing global and local techniques for pulp flow velocity estimation was proposed, where a synthetic image set and a real-world image set were used for testing in [81].
4. **Dirt classification.** The detection and classification of dirt in dried pulp sheets is an important part of pulp and paper quality assessment. Dirt causes undesired surface properties in subsequent processing, negatively affects the surface appearance, and can impair the printability of paper. Within the scope of the dirt classification task, the problem of ground truth generation was considered. The identification of specific dirt particles can be a very difficult task even for experts, and the large amount of data required makes collecting the ground truth a very laborious and time-consuming process. In [85], a solution for a semisynthetic ground generation was proposed and an adaptive framework for dirt particle classification was first introduced in [83]. The work was extended with additional experiments, literature overview, and a more detailed description of the method in [86].

### 1.3 Structure of the thesis

The thesis is organized as follows. In Chapter 2, an overview of the pulping process is given as well as the description of pulp suspension properties, and the measurements that are needed for pulping process control and product analyses. The fundamental steps of the Machine Vision systems are outlined, discussing the typical issues that should be addressed (i.e., ground truth formation and methods evaluation). An overview of the existing vision-based methods for pulping process is provided and the motivation for the development of the new methods is given. The following chapters introduce the proposed methods for the main tasks of the thesis.

Chapter 3 introduces the method for fiber detection and characterization. The proposed approach starts with an edge detection algorithm after which the task of object detection becomes a problem of edge linking. A state-of-the-art local linking approach called tensor voting is used to estimate the edge point saliency describing the likelihood of a point belonging to a curve, and to extract the end points and junction points of these curves.

Chapter 4 presents the framework for bubble detection as Concentric Circular Arrangements (CCA). The CCAs are recovered in a hypothesize-optimize-verify framework. The hypothesis

generation is based on sampling from the partially linked components of the non-maximum suppressed responses of oriented ridge filters, and is followed by the CCA parameter estimation. Parameter optimization is carried out by minimizing a novel cost-function.

The method for pulp flow characterization is described in Chapter 5. The correlation-based methods, the autocorrelation method and the Particle Image Pattern (PIP) technique, are applied to solve the problem and the performance of the methods is compared based on the manually created ground truth.

Dirt particle detection and classification as well as the method for semisynthetic ground truth generation can be found in Chapter 6. To classify the dirt particles, a set of features is computed for each image segment. Sequential feature selection is employed to determine a close-to-optimal set of features to be used in classification. The results are discussed in Chapter 7 and the conclusions are drawn in Chapter 8.



---

## Pulping measurements and machine vision

---

### 2.1 Pulping process

The main raw material in papermaking is wood consisting of fibers, wood cells that are kept together by a complex chemical compound called lignin, and hemicellulose [20]. The properties of the papermaking products are influenced considerably by the raw material used in the production. Wood is divided into two groups: softwood and hardwood. Softwood, such as pine and spruce fibers, are long and slim, whereas hardwood fibers, for instance, oak and birch fibers, tend to be short and contain vessel elements. Even within one tree the properties of fibers can vary. The properties depend on the growth periods: intensive growth in the summer and slower in the autumn and the winter. The fiber dimensions also vary depending on their location within a tree. The length increases from the root up towards the middle of the trunk and decreases from the middle of the tree up to the top. Large variation in wood properties allows to produce different types of paper products. Softwood is usually utilized for producing containers, corrugated boxes, paper bags; products requiring good strength and tensile qualities. Hardwood, providing good optical properties, such as gloss and opacity, is commonly used for writing and printing paper manufacturing.

To make use of the wood fibers, the lignin bonds need to be broken and the fibers released forming a fiber suspension [82]. The papermaking process starts with pulping (wood disintegration) in order to release fibers that later are fed into the paper machine to form a paper web. There are two ways to separate fibers [61]: either chemically, when the lignin is dissolved with special chemical treatment, or disintegrated using mechanical forces. The way the fibers are disintegrated also affects the properties of the material, leading to certain qualities of the final product. For example, mechanical pulp is too stiff to produce smooth and strong paper, and therefore it is used for the products requiring good optical properties. In practice, in order to manufacture a product with desired properties and quality, a mixture of softwood and hardwood is used as well as a combination of processing methods.

The thesis is focused on the analysis of measurements from the pulping process. Fig. 1.2 illustrates a chemical pulping fiber line [28]. Wood is mechanically debarked and chipped. After further chemical disintegration (cooking), the fibers form the main material to be analyzed, pulp

suspension, consisting of fibers, fillers, and additives. Fibers need to create the bonds in the paper web, and therefore in the process of cooking they are beaten and refined. Pulp suspension can also contain impurities, knots, incompletely delignified wood, and ink (in the case of recycled pulp). Subsequently pulp is screened and washed and the rejects are usually reprocessed. In order to produce white paper, the pulp suspension is bleached. At the bleaching stage the lignin is removed and the material loses its light absorbing property. Pulping can be performed either at a separate mill, after which the pulp is shipped to a paper mill, or it can be integrated into the papermaking process. In Fig. 1.2 the operation of a nonintegrated pulp mill is illustrated. The end product of such a mill is dried pulp sheets or rolls that are shipped to a paper mill.

## 2.2 Pulping process measurements

Pulping is a complicated process that includes multiple stages of wood processing. An important part of pulping and papermaking is process control that includes both process and product analysis [55]. The papermaking industry invests significant resources in quality analysis, quality control, inspection and monitoring systems. It is difficult for a human operator to control a complicated process continuously. Loss of attention and limited reaction time can become a negative factor at a crucial moment. Furthermore, differences between operators can lead to varying quality of a product. Physically heavy and dangerous operations also require automation. Computerized support is required when analyzing long sequences of data and choosing the optimal parameters of the process. Traditionally, material testing is performed at a laboratory level where a parameter set that correlates well with the property of the product is measured. Today, the industry is searching for solutions that will transfer laboratory tests to in-line measurements.

In this thesis, the material is pulp suspension (see Fig. 2.1) and the end product is dried pulp that is provided to the paper mill and is further utilized in papermaking. The pulp suspension measurements allow to perform process and product analyses.

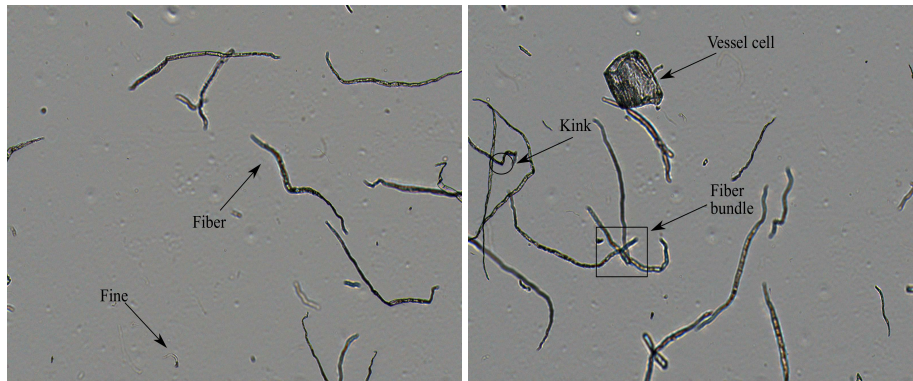
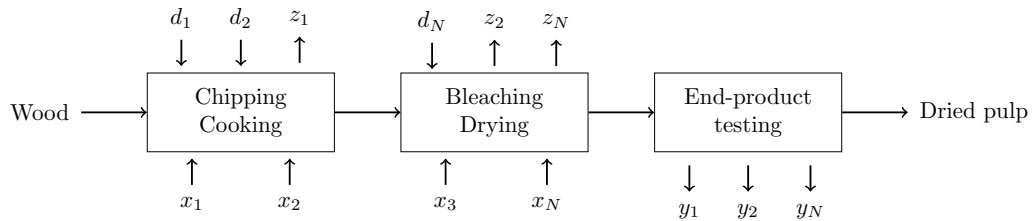


**Figure 2.1:** Pulp suspension elements imaged using non-polarized light microscopy (provided by CEMIS-OULU).

**Process analysis.** As illustrated in Fig. 2.2, the quality of the product is described by the product state variables  $y_1, \dots, y_N$ . The process state variables  $z_1, \dots, z_N$  characterize certain aspects of the manufacturing process. Furthermore, the product state variables and the process state variables

depend on the control variables  $x_1, \dots, x_N$  and on the process disturbances  $d_1, \dots, d_N$ . An example of a process variable is a volume of gas that is fed into the pulp suspension for delignification. It affects the efficiency of the bleaching process and the properties of the end-product.



$x_1, \dots, x_N$  - control variables  
 $y_1, \dots, y_N$  - product state variables  
 $z_1, \dots, z_N$  - process state variables  
 $d_1, \dots, d_N$  - process disturbances

**Figure 2.2:** Pulping process with the variables involved in a testing strategy, modified from [55].

Process analysis searches for a pair of critical variables that are Pareto optimal with respect to the system: if one variable changes in a desired direction the other changes in an undesired direction. It also identifies control variables using which to choose the optimal critical variables. There are three main purposes of process control [54]: i) to control the process variables, such as temperature and pressure, maintaining them at a desired level, ii) to perform the controlled changes, such as changing the temperature according to a predetermined program, and iii) to define the optimal values of the variables analyzing the current state of the process.

**Product analysis.** According to [55], product analysis provides numerical measures for the significant properties of the material concerning the functional behavior or the use of the product. Practically, a matrix is computed where one dimension is the functional requirements to the product or material and the other dimension is the measurable properties of the material. The reasons for product analysis are summarized in [55]. First of all, in order to keep the product quality at the same level, the process variables, such as temperature and pressure, should be regulated automatically according to the properties of the material. Secondly, product analysis helps in the development of new equipment. Finally, product analysis tests characterize the products, allowing to evaluate its functional properties (e.g, strength and opacity).

### 2.2.1 Pulp suspension measurements

Both product and process analysis require measurements of pulp suspension properties. What measurements to perform depends on the characteristics to be analyzed, on the process from which the measurement is carried out and the limitations that the process environment introduces. In [55], the following groups of pulp properties are presented: single fiber properties, papermaking properties of pulp, and chemical characteristics of pulp. In this section, first, the single fiber properties are summarized, since fibers are the main component of pulp suspension. Second, the papermaking properties of pulp are presented. Utilizing this information the specialists can judge about the material behavior in papermaking. Third, the chemical analysis is discussed briefly as

this is not the focus of the thesis. Finally, the pulping process condition measurements are discussed, which is especially important if the aim is to develop in-line measurements. Table 2.1 summarizes the pulp suspension measurements showing to which groups the methods developed in this thesis are referred to.

**Table 2.1:** Pulp suspension measurements.

| Measurements  | In this thesis  |
|---|---|
| Papermaking properties of pulp:<br>- dried pulp sheets analysis (e.g., optical properties, strength)<br>- pulp suspension analysis (e.g., drainage resistance)                            | Detection and classification of dirt particles (Chapter 6)<br>Fiber width/length distribution (Chapter 3) |
| Single fiber properties:<br>- fiber properties (e.g., wall porosity, stiffness)<br>- identification of pulp fibers (e.g., hardwood/softwood)<br>- fiber dimensions (e.g., wall thickness) | Fiber curl index (Chapter 3)<br>Fiber width/length distribution (Chapter 3)                               |
| Chemical analysis of pulp (e.g., surface strength)  | Not studied   |
| Pulping process conditions<br>(e.g., drainability of pulp suspension)   | Gas volume at delignification (Chapter 4)<br>Pulp flow characterization (Chapter 5)                       |

**Single fiber properties.** Since the paper web is formed by fiber bonds, it is important to measure the single fiber properties described in [55]. The single fiber properties are divided into three subgroups: pulp identification, fiber dimension measurements, and fiber properties. Pulp fiber identification aims at determining the wood species or the type of pulp (hardwood/softwood). The identification of pulp type utilizes morphological features of fibers (e.g., curl and coarseness). Fiber dimension measurements, including fiber length, width, and wall thickness, are important since they change during the pulping process and have an impact on paper tensile and folding properties [90]. Fiber properties include stiffness, wall porosity, and fiber deformation (curl index and kink index). Kink is an abrupt change in fiber curvature that affects the formation of paper and its strength properties. Fiber curl and kink indices influence tensile stiffness, tear index, porosity, and absorbency. In this thesis, a method to compute fiber morphological properties, such as average length and curl index, was developed.

**Papermaking properties of pulp.** The second group of measurements is related to the papermaking properties of pulp, for example:

- suspension consistency (fiber concentration),
- proportion of fines (short fibers, most commonly produced during mechanical pulping); fines enhance the optical properties of paper, but impair the strength,
- presence of cells and their morphology: the size, character, and number of vessel cells can be utilized for species identification,

- presence of fiber bundles, which affect the formation of the paper web, and
- presence of impurities.

According to [55], traditionally, these measurements are performed at the laboratory level simulating the papermaking process in a standardized way. In practice it means that instead of being measured directly in the process line, the papermaking properties of pulp are measured from dried pulp sheet samples. There is a correlation between the real fiber properties that would be measured online in the process, and the laboratory measurements, but it is difficult to establish. The stages of the laboratory simulation are as follows [55]:

1. disintegration of the dried pulp sheets in water,
2. beating of pulp in the laboratory beater,
3. testing of pulp properties, such as drainage properties and fiber length,
4. preparation of the laboratory sheets,
5. pressing, drying, and conditioning of the laboratory sheets, and
6. measuring the sheet properties, such as strength, structural properties, and optical properties.

A method for dirt particle detection and classification developed in this thesis can assist in estimating papermaking properties of pulp since the presence of dirt particles affect the formation of the paper web.

**Chemical analysis.** Chemical analysis focuses on the total composition of pulp, which allows judgement on the surface properties, strength, and folding endurance of the product. The chemical properties of lignin and extractives are studied as well as the carbohydrate content of pulp. It also includes tests on color reversion, where pulp is exposed to temperature changes, high humidity, and visible or ultraviolet light. The behavior of pulp properties indicates how the properties of the end-product will change in such conditions. The nature of the dirt particles (e.g., shives, bark, plastic) is studied in the scope of chemical analysis as well. Many methods of chemical characterization are standardized by ISO, TAPPI, and SCAN organizations.

**Pulping process conditions.** Although it simulates the stages of the pulping process, laboratory testing does not provide a clear view of the papermaking potential of pulp [55]. Therefore there is an ongoing development of intelligent methods for in-line measurements where the process condition measurements is one of the important aspects. The measurements for process conditions characterization depend on the stage of the process. For example, in Table 2.1 drainability of pulp suspension is shown as an example of a measurement that indicates the condition of the beating process: whether it should be stopped or not. Another example is measuring the gas volume distribution as a decisive factor in the termination of the bleaching process. Analysis of pulp flow, such as velocity or presence of anomalies in the flow, tells about the condition and the state of the process as well.

### 2.3 Machine vision

Machine vision methods have provided efficient and robust tools in industrial applications that require automated control and product analyses (e.g., [42] and [13]). The application of machine vision methods enable the collection of important numerical information from the industrial process, but also the visualization of the phenomena for its better understanding. In some cases there are no other possible measurements available except from laborious manual work.

Based on [27], the main steps of a machine vision system are summarized in Fig. 2.3. The first step is the imaging of the process phenomena. Imaging is a separate difficult problem that should consider the physical conditions and the material specifics in order to provide images of a sufficient quality appropriate for further processing. After the images are acquired they can be enhanced by noise removal or illumination correction, for example. This step makes the target objects more distinct in the images and removes the artifacts that produce false detections. In Fig. 2.3, the illumination of the original image from pulp bleaching process was modeled and compensated, making the bubbles detectable near the edges of the image. Subsequently, the machine vision methods are utilized to segment the required objects. After that, the objects are characterized by computing a set of features distinctive for this type of object. The final step depends on the application. It can be either estimation of a parameter, such as concentration of fibers, or classification (e.g., hardwood vs. softwood). In Fig. 2.3, the bubbles are characterized by their radius and center coordinates and then the total volume of the gas in the image is computed.

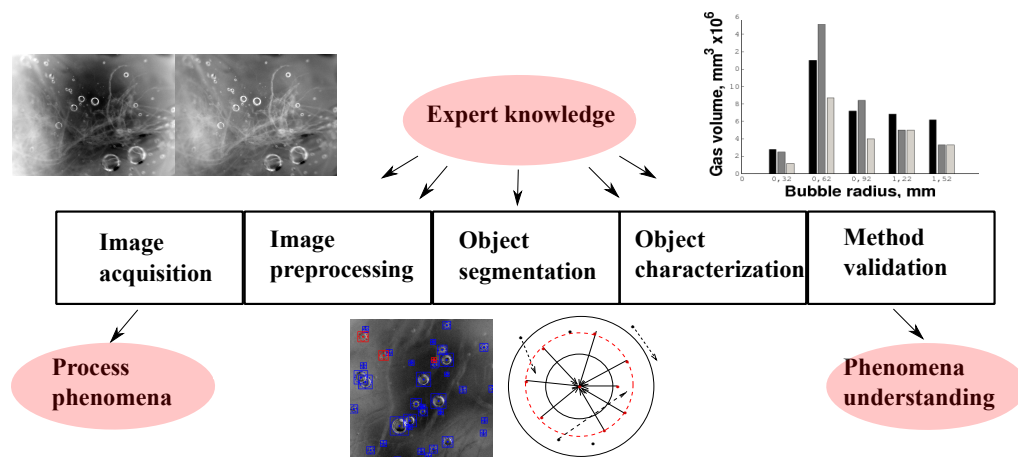


**Figure 2.3:** Fundamental steps of machine vision.

The obtained results need to be verified in order to evaluate the accuracy of the method. If there is no reference measurement to compare against the results, then expert knowledge (ground truth) plays a very important role in machine vision system development. In the beginning, the expert knowledge gives an introduction to the topic, providing the understanding of the material properties. In order to validate the system, the results obtained with the automated method are compared to the provided ground truth. In the cases when the training of the system is needed the expert knowledge is used as well. However, the crucial questions are: who can provide the data, in what

form, and is it possible to model it. Typically, an expert from the application field is asked to mark the objects of interest or give a numerical description of the material. Since data can sometimes be very difficult (e.g., it is not always clear if there is a bubble to be marked or not), the ground truth can vary from expert to expert. There is a human factor that if the amount of data is large an expert can lose focus.

There are several ways to address the ground truth problem. Data provided by several experts can be modeled to get rid of a bias. A semi-automatic method can be designed to help the expert. Finally, the ground truth obtained with an automatic method can be verified by an expert. In the last case, however, the expert can get biased towards the automatically marked ground truth. The complexity of the data determines what method to use for ground truth generation.

Once provided with the ground truth, the performance of the machine vision system can be evaluated using several metrics. In this thesis, the following metrics were used when a parameter was estimated from the detected objects. The accuracy of a parameter  $P_{est}$  estimation provided the ground truth value  $P_{gt}$ , for  $M$  images is computed as the mean relative error  $\frac{1}{M} \sum_{i=1}^M \left( \frac{|P_{est_i} - P_{gt_i}|}{P_{gt_i}} \right)$ . The precision of the measurement is  $\frac{1}{M} \sum_{i=1}^M \left( \frac{P_{tp_i}}{P_{est_i}} \right)$ , where  $P_{tp_i}$  is the measure corresponding to the correctly detected objects. To estimate the detection results, for instance, what is the detection rate of fiber detection, the following notation is used:

- percentage of correctly detected objects, True Positives (TP),
- percentage of objects that were not detected, False Negatives (FN), and
- percentage of objects that were detected, but were not marked by an expert, False Positive (FP).

Depending on the application, different metrics can be applied. Another important factor is the computation time that should satisfy the technical requirements. When developing a machine vision method, a trade-off between computational time and accuracy should be taken into account as well.

## 2.4 Existing solutions

The work on process control automation and in-line material analysis using image-based techniques has been performed earlier [32]. This section describes the relevant mostly vision-based existing solutions for the four main tasks of the thesis.

**Fiber characterization.** According to the review of Hirn and Bauer [31], several commercial fiber analyzers exist such as FiberLab [14], MorFi [5], FS200 [14], and Fiber Quality Analyzer (FQA) [94]. These analyzers typically take a pulp sample and analyze it in laboratory conditions. This is time-consuming and does not allow real-time monitoring and control during the production. Some analyzers (e.g., FQA) incorporate a cytometric flow cell that orients and positions fibers for more precise measurements [94]. However, the existing solutions usually use highly diluted pulp suspension. The difficulty of the in-line measurement, besides the hard physical conditions, is the high consistency of fibers. Furthermore, it is needed not only to estimate the single properties of fibers, but also to characterize the connected fiber network. Therefore further work on this topic is needed.

**Gas volume estimation.** At the bleaching stage of pulping, there is a need to estimate the volume of the gas fed into the suspension. Gas manifests itself as bubbles in the images. Another important factor is gas volume distribution with respect to bubble size. In [32] a similar problem of bubbles detection is concerned, but the imaging setup is different which produces different kind of images than in the present thesis. Moreover, the processes in [32] and in the current work are different. The images that were utilized in this thesis are novel and the author is not aware of the previous work performed on this task that would involve vision-based approaches. It is worth to mention that there are other than image-based gas content measurements in pulp and paper industry, for example, a commercial device based on ultrasound propagation [2], that is, however, limited to 2% consistency.

**Pulp flow characterization.** Magnetic flow meters are currently used at the pulp mills to measure a time dependent velocity averaged over 2D cross section, for example a flow meter by KROHNE [1]. Providing reasonable cost and accuracy, this measurement, however, does not allow to take into account local variations and anomalies of the flow. Other common methods for pulp flow characterization include a Laser Doppler Anemometry (LDA) method [40], a method of Nuclear Magnetic Resonance Imaging (NMRI) [57], and the method of Ultrasound Velocity Profiling (UVP) [101]. The NMRI technique is used to measure an average velocity of the pulp flow and it is highly dependent on the pulp consistency. The method can be applied only to the pulp flow with a low concentration, whereas this is not necessarily the case in the in-line measurements, where consistency is usually high. Additionally, in order to apply the UVP and LDA methods, it is necessary to use expensive equipment that is difficult to embed. DANTEC Fiber-Flow Series 60X is a device designed on the basis of the LDA method. It connects two specter analyzers, for example, DANTEC 57N10 which interprets the Doppler signal to compute velocity. This tool is controlled by software from Burst Ware [98]. In [32] the study is focused on various aspects of measuring the fluid dynamics and dispersed phase morphology in multiphase flows. However, in [32] different kind of data is utilized and the industrial processes are different.

The UVP and LDA methods enable estimation of velocity for pulp flow with a concentration greater than the concentration allowed for the NMRI method. However, both methods require sophisticated and expensive equipment, which is complicated to configure, install, and operate.

**Dirt classification.** Dirt detection and counting has been studied earlier but the problem of dirt particle classification was not addressed. For example, Fastenau et al. [21] presents a laser system for dirt counting at the industrial scale. The paper gives the motivation for the automation of the dirt counting process, explaining the difficulties of the manual procedure. Based on the shape of the obtained signal, the system was capable to perform dirt particle categorization by the size of particles. Sutman [89] presents a method for measuring the testing precision. The effect of the sample size on the dirt count test precision was not well understood and it was the motivation for the research. Rosenberger [78] showed that the threshold for dirt counting should be selected automatically as well to be able to adapt for different lighting conditions as well as paper and dirt particle properties.

Juntunen et al. [42] introduced an automated analysis system for colored ink particles in recycled pulp. The samples were prepared with a known percentage of ink. A microscope with an attached color video-camera was used to image the samples. Thresholding was performed separately for three HSI channels, followed by the connectivity analysis. The system allowed the dirt counts to be obtained and the size distribution of the particles to be measured. Since the ground truth did not contain the information on the location of the particles, there was no opportunity to judge about the spatial distribution of the dirt.

In [70], the "Pulp Automated Visual Inspection System", that segments and counts dirt particles as areas in an image with an intensity lower than a certain threshold, is introduced. Another example InsPulp, an on-line visual inspection system, is presented in [8]. The paper is imaged by a CCD camera and the dirt is segmented using a local dynamic threshold, which allows the system to segment and detect the impurities in pulp with a low error rate. These methods only count the dirt particles and do not address the more challenging problem of dirt particle classification.

The industrial dirt counter system by VERITY IA [3] can divide the particles into a few groups based on their shape, but is still not able to identify the specific dirt types. The accurate classification of particles would be a great benefit. Savings in chemical and energy consumption could be attained by adjusting bleaching and screening, the aim of which is to eliminate the impurities in the material. In a production problem situation, fast and precise information on the type of particles present in the process can reveal the source of the problem, and the process can be adjusted accordingly.

## 2.5 Summary

In this chapter, an introduction to the pulping process was given together with the description of pulping process measurements that allow process control and product analyses. The machine vision methods provide the tools for material analyses allowing the experts to understand the process and control it in the automated way. The steps of a typical machine vision system were described, including a discussion about the importance of the expert knowledge and the ways of system evaluation. For the main research tasks of the thesis, outlined in Section 1, the existing machine vision solutions were discussed giving a motivation for the research carried out in the thesis.



---

## Fiber detection and characterization

---

### 3.1 Problem statement and previous work

The automated analysis of suspension images can enable in-line monitoring and control for pulping and papermaking instead of the current off-line laboratory analyses. Fiber properties [55], such as the length and the curl index, affect the formation of the paper web, which makes it important to monitor these properties during the papermaking process.

Fibers appear in the images (see Fig. 3.1) as curvilinear objects, which motivates the detection of fibers as curvilinear structures. A typical approach to implement curvilinear structure detection is to detect salient points belonging to the curvilinear structures followed by a grouping procedure [69]. In [41], curvilinear structures were recovered from the skeletons of the grayscale images that were extracted by a distance transform utilizing edge maps of the images. In [33], the matched filter technique was applied to detect vessel segments in retinal images and an iterative threshold probing scheme was used to determine which pixels in the segments belong to vessels. The matched filter technique convolves an image with multiple filters that are designed to detect desirable features. In [19], spatial context in the solar images was modeled with Markov Random Fields (MRF) extracting salient contours. The MRF based approaches applied to contour completion, such as [64], assign initial labels to the salient points, formulate a cost-function based on the label, and optimize it by relabeling the pixels, which provides the final solution.

The framework proposed in this thesis is based on tensor voting presented by Medioni et al. in [63]. In tensor voting, each pixel is associated with a tensor encoding the pixel orientation or the most probable orientation of a curve in that pixel. After an initialization, pixels cast votes in their neighborhood, described by a voting field, iteratively increasing the saliency of their neighbors belonging to the same curve. As a result of voting, a saliency map is obtained, and it indicates the probability of the pixels belonging to the curvilinear structures. Additionally, the tensor voting provides pixel junction and polarity maps, showing which pixels belong to the junctions and which to the end points. The main advantage of the approach is that there is no need to optimize an explicitly defined complicated objective function.

In [84], the method of fiber detection and characterization was introduced based on the prelimi-

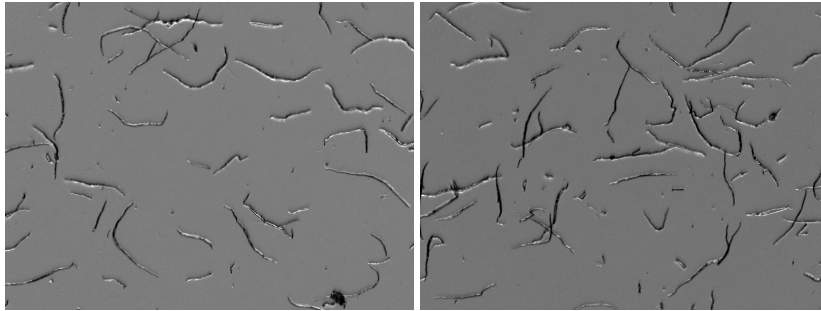


**Figure 3.1:** Examples of the pulp suspension images (provided by CEMIS-OULU). The image contrast has been increased for illustrative purposes.

nary experiments in [50]. The fiber length/width distribution and curl index were estimated from the detected fibers. The preliminary experiments on image enhancement and fiber segmentation were performed in [51] and were reported in [52].

### 3.2 Fiber detection framework

The curvilinear objects are recovered using the framework introduced in Fig. 3.2. A grayscale image is reduced to an edge map by an edge detection method based on direction-sensitive filtering. Next, the tensor voting is applied to the edge map to retrieve the point saliency, end points, and junction points. Finally, the curves are grown from the most salient points utilizing the novel linking algorithm.

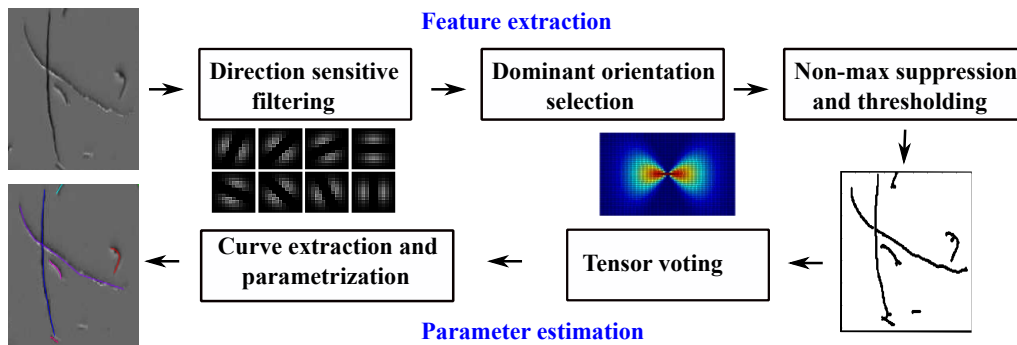


**Figure 3.2:** Framework for curve extraction and parameterization.

#### 3.2.1 Oriented edge map computation

To compute the edge map, an image is filtered by a second derivative zero-mean Gaussian filter in eight directions with the filter masks shown in Fig. 3.2. The dominant orientation of the edge nor-

mal in each pixel is computed as the maximum of the eight filter responses [59]. Non-maximum suppression in the dominant orientation of the edge normals is performed together with hysteresis thresholding as described in [9].

### 3.2.2 Pixel saliency estimation

Saliency [63], in the context of curvilinear structure detection, indicates the probability of a pixel belonging to a curvilinear structure. To determine the saliency for each pixel, the tensor voting approach is applied. First, each pixel is associated with a tensor  $\mathbf{T}$  that encodes the curve orientation of this pixel. The tensors are initialized as a matrix

$$\mathbf{T} = \begin{bmatrix} \cos(d)^2 & \cos(d)\sin(d) \\ \cos(d)\sin(d) & \sin(d)^2 \end{bmatrix}, \quad (3.1)$$

where  $d$  is a pixel orientation. After being initialized, each pixel votes for its neighbors in its voting field, supporting the assumption that they belong to the same curve. The voting field (see Fig. 3.3(a)) is oriented along the tangent to the curve in the pixel. It weights the pixels in the neighborhood, giving a higher weight to the pixels that are located along the curve. The size of the voting field  $w \times w$  [62] is computed using a parameter  $\sigma$ , scale of voting, as

$$w = \frac{-16\log(0.1) \cdot (\sigma - 1)}{\pi^2}. \quad (3.2)$$

The coefficient of the voting field in the pixel  $p$  is computed as

$$\mathbf{F}(l, \theta, \sigma) = \exp\left(-\left(\frac{s^2 + ck^2}{\sigma^2}\right)\right) \begin{bmatrix} -\sin(2\theta) \\ \cos(2\theta) \end{bmatrix} \begin{bmatrix} -\sin(2\theta) & \cos(2\theta) \end{bmatrix} \quad (3.3)$$

where  $s = \frac{\theta l}{\sin(\theta)}$ ,  $k = \frac{2\sin(\theta)}{l}$ ,  $l$  is the distance to the voter,  $\theta$  is the angle (see Fig. 3.3(b)), and  $c$  is a constant which controls the decay with high curvature. In the voting process, a voter's tensor is added to the tensors of the pixels in the voting field multiplied by the field coefficient. After the voting procedure, the saliency of a pixel is the difference between the larger and the smaller eigenvalues of its tensor. The smaller eigenvalue indicates how likely it is that a pixel is a junction point. The whole process to obtain the saliency map is summarized in Algorithm 1.

### 3.2.3 Pixel polarity estimation

The previous step produces the saliency and junction point maps. To find the end points, information on the pixel polarity can be exploited [93]. A polarity vector indicates the direction from which the majority of the votes come. If most of the votes come from one direction, the point is likely to be an end point. Pixel polarity is computed as presented in Algorithm 2, using first-order voting. Unlike in second-order voting used in pixel saliency estimation, where the voting is done by matrices, in first-order voting the votes are cast by vectors. A voter casts a vote to each pixel in its voting field as a vector oriented towards the voter (see Fig. 3.4(a)). As a result of voting, a polarity vector in each pixel is the sum of the vectors pointing to all the voters. Therefore, as illustrated in Fig. 3.4(b), polarity vectors of the end pixels are oriented towards the inner part of the curve. The polarity value is computed as the length of the polarity vector's projection on the vector tangent to the curve (perpendicular to the normal vector).

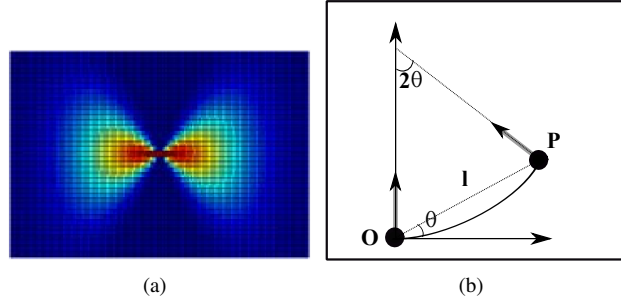


**Figure 3.3:** Voting field: (a) Example of a voting field oriented horizontally (the color corresponds to the field coefficient, with red representing a high and blue representing a low value); (b) Votes cast by a stick tensor located at the origin  $O$  (see the text for explanations of other symbols).

---

**Algorithm 1** Second-order tensor voting for edge saliency estimation

---

**Input:** a set of edge pixels  $\mathbf{P} = \{\mathbf{p}_i = [x_i, y_i, d_i]\}$  where the position of a pixel is described by its coordinates  $x_i, y_i$  and its orientation by angle  $d_i$ .

**Output:** a saliency map  $\mathbf{S}$ , a junction map  $\mathbf{J}$ .

**Parameters:** a scale of voting  $\sigma$ .

- 1: **for** each edge point  $\mathbf{p}_i$  **do**
  - 2:     Initialize the second order tensor as  $\mathbf{T}_i = \begin{bmatrix} \cos(d_i)^2 & \cos(d_i)\sin(d_i) \\ \cos(d_i)\sin(d_i) & \sin(d_i)^2 \end{bmatrix}$ .
  - 3: **end for**
  - 4: **for** each edge point  $\mathbf{p}_i$  **do**
  - 5:     Compute the tensor field coefficients  $\mathbf{F}_i$  as in Eq. 3.3.
  - 6:     Perform eigenvector decomposition of the tensor  $\mathbf{T}_i$  to obtain eigenvalues ( $\lambda_{1_i}, \lambda_{2_i}$ ) and eigenvectors ( $\mathbf{e}_{1_i}, \mathbf{e}_{2_i}$ ).
  - 7:     **if**  $\lambda_{1_i} - \lambda_{2_i} > 0$  **then**
  - 8:         **for** each edge point  $\mathbf{p}_j$  in the voting field  $\mathbf{F}_i$  **do**
  - 9:             Compute a new tensor matrix  $\mathbf{T}_i = \mathbf{T}_j + \mathbf{T}_i\mathbf{F}_i(\mathbf{p}_j)$ .
  - 10:         **end for**
  - 11:     **end if**
  - 12: **end for**
  - 13: **for** each edge point  $\mathbf{p}_i$  **do**
  - 14:     Perform eigenvector decomposition of the tensor  $\mathbf{T}_i$  to obtain eigenvalues ( $\lambda_{1_i}, \lambda_{2_i}$ ) and eigenvectors ( $\mathbf{e}_{1_i}, \mathbf{e}_{2_i}$ ).
  - 15:     Assign  $\mathbf{S}(p_i) = \lambda_{1_i} - \lambda_{2_i}$  and  $\mathbf{J}(p_i) = \lambda_{2_i}$ .
  - 16: **end for**
- 

### 3.2.4 Linking and fiber separation

The pixel saliency estimation and pixel polarity estimation steps produce the curve saliency, junction saliency, and end points maps. The final step is to extract the curvilinear structures from the image based on this information. For this, a curve growing method is used. According to [62],

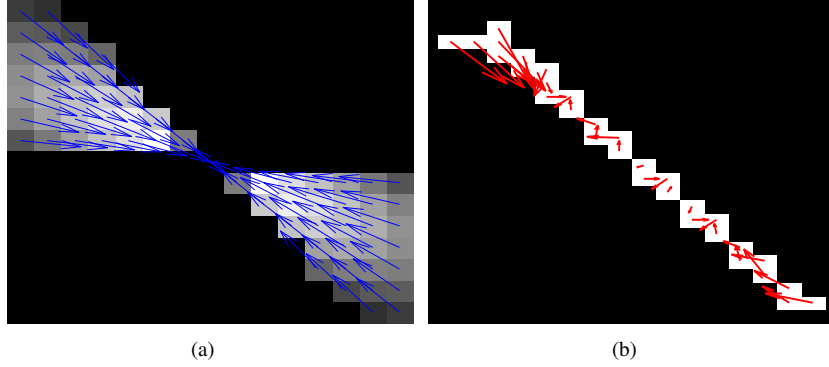


**Figure 3.4:** An example of the polarity map computation: (a) The polarity vectors generated by one voting pixel; (b) The map.

---

**Algorithm 2** First order tensor voting for polarity estimation

---

**Input:** a set of edge pixels  $\mathbf{P} = \{\mathbf{p}_i = [x_i, y_i, d_i]\}$  where  $x_i, y_i$  are the pixel coordinates and  $d_i$  its orientation.

**Output:** a polarity matrix  $\mathbf{R}$ .

**Parameters:** a scale of voting  $\sigma$ .

- 1: Initialize a polarity matrix  $\mathbf{R}$  and a matrix of polarity vectors  $\mathbf{P}$  by zero elements.
  - 2: **for** each edge point  $\mathbf{p}_i$  **do**
  - 3:     **for** each edge point  $\mathbf{p}_j$  in a voting field of size  $w$  (Eq. 3.2) **do**
  - 4:         Compute a vector  $\mathbf{t}$  oriented toward the edge point  $\mathbf{p}_i$ .
  - 5:          $\mathbf{P}(\mathbf{p}_j) = \mathbf{P}(\mathbf{p}_j) + \mathbf{t}$ .
  - 6:     **end for**
  - 7: **end for**
  - 8: **for** each edge point  $\mathbf{p}_i$  **do**
  - 9:     Compute  $\mathbf{R}(\mathbf{p}_i)$  as a length of the projection of vector  $\mathbf{P}(\mathbf{p}_i)$  on the tangent vector in the point  $\mathbf{p}_i$ .
  - 10: **end for**
- 

the curve growing starts by choosing an unprocessed seed point of high saliency and iteratively growing the curve following the estimated tangent direction. A next point is added to the curve if it is a point with maximum saliency in the tangent direction. In [66], the importance of junction point and end point detection is emphasized and an approach for contour completion based on tensor voting is presented. However, the approach does not provide instructions for the separation of two or more intersecting curvilinear structures. In Algorithm 3, a method for curvilinear structure extraction is presented, where the curves are recovered as a set of pixels from the saliency map utilizing the information about the junction points and the polarity of the points. When the curve growing algorithm reaches a region of a junction selected by using a threshold  $T_j$ , the direction of growing stays as it was before the junction because in the junction region there is no certainty of the pixel orientation. In this thesis global thresholds are used because the fibers are located in the same plane and they are distinct in the images.

**Algorithm 3** Curve extraction algorithm

**Input:** a set of edge pixels  $\mathbf{P} = \{\mathbf{p}_i = [x_i, y_i, d_i]\}$ , where  $x_i, y_i$  are the pixel coordinates,  $d_i$  its orientation, a matrix of tensors  $\mathbf{T}$ , a polarity matrix  $\mathbf{R}$ , a saliency matrix  $\mathbf{S}$ , a junction matrix  $\mathbf{J}$ .

**Output:** a list of curves  $\mathbf{Q} = \mathbf{q}_m$ .

**Parameters:** a threshold for seed points selection  $T1_s$ , a saliency threshold  $T2_s$ , minimal polarity of an end point  $T_e$ , a threshold for junction points  $T_j$ .

- 1: Select a subset of seed points  $\mathbf{P1} = \{\mathbf{p}_i\}$  with the saliency value  $\mathbf{S}_i > T1_s$ .
- 2: **for all** salient points  $\mathbf{p}_i$  from the set  $\mathbf{P1}$  **do**
- 3:     Perform eigenvector decomposition of the tensor  $\mathbf{T}_i$  to obtain eigenvalues  $(\lambda1_i, \lambda2_i)$  and eigenvectors  $(\mathbf{e1}_i, \mathbf{e2}_i)$ .
- 4:      $\mathbf{q1} = \text{CURVE\_GROWING}(\mathbf{S}, \mathbf{J}, \mathbf{R}, \mathbf{p}_i, \mathbf{e1})$ .
- 5:      $\mathbf{q2} = \text{CURVE\_GROWING}(\mathbf{S}, \mathbf{J}, \mathbf{R}, \mathbf{p}_i, -\mathbf{e1})$ .
- 6: **end for**
- 7: Join two parts of the curve  $\mathbf{q} = [\mathbf{q1}, \mathbf{q2}]$ .
- 8: Add the curve to the list of the curves  $\mathbf{Q} = [\mathbf{Q}, \mathbf{q}]$ .

- 1: **function** CURVE\_GROWING( $\mathbf{S}, \mathbf{J}, \mathbf{R}, \mathbf{p}, \mathbf{e}$ )
- 2:     Current seed point  $\mathbf{p}_{\text{curr}} = \mathbf{p}$ .
- 3:     **while**  $(\mathbf{R}(p_{\text{curr}}) < T_e)$  and  $(\mathbf{S}(p_{\text{curr}}) < T2_s)$  **do**
- 4:          $\mathbf{d}_{\text{curr}} = \mathbf{e}$ .
- 5:         **if**  $\mathbf{J}(\mathbf{p}_{\text{curr}}) > T_j$  **then**
- 6:              $\mathbf{d}_{\text{curr}} = \mathbf{d}_{\text{pred}}$ .
- 7:         **end if**
- 8:          $\mathbf{p}_{\text{curr}} =$  the most salient point in the  $\mathbf{d}_{\text{curr}}$  direction.
- 9:         Add  $\mathbf{p}_{\text{curr}}$  to the curve  $\mathbf{l}$ .
- 10:          $\mathbf{d}_{\text{pred}} = \mathbf{d}_{\text{curr}}$ .
- 11:     **end while**
- 12:     **return**  $\mathbf{l}$
- 13: **end function**

**3.2.5 Fiber characterization**

A term "fiber morphology" [31] denotes a set of fiber properties that describe a structural appearance of fibers. It commonly includes five parameters: length, width, coarseness, kink, and curl. In this thesis only fiber length and curl are computed.

The fiber length is defined as the fiber contour length  $L$  or as an end-to-end (projected) length,  $l$  [94] as illustrated in Fig. 3.5.  $L$  can be computed as a length of a spline approximating a fiber curve, while  $l$  is computed as a distance between end points. When computing an average fiber length, instead of the average length of all fibers a length-weighted mean is computed in order to take fines into account [31]. The length-weighted average fiber length [14] is computed as follows:

$$\hat{L} = \frac{\sum_{i=1}^N L_i^2}{\sum L_i}, \quad (3.4)$$

where  $\hat{L}$  is the length-weighted average length,  $L_i$  is the length of a fiber and  $N$  is the number of fibers.

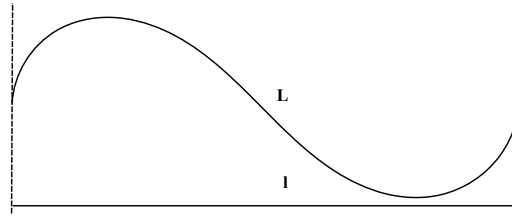


**Figure 3.5:** Fiber length [90].

The fiber curl index provides information about the fiber curvature. The curl index is calculated for each individual fiber as:

$$CI = \frac{L}{l} - 1. \quad (3.5)$$

The curl index describes the degree of fiber curvature but it gives no information whether a fiber is a smooth or an abrupt curve [31]. A curl index of zero indicates that no curl is present [90].

### 3.3 Experiments and discussion

#### 3.3.1 Data and results evaluation

The proposed approach to fiber detection and characterization was tested on a set of pulp suspension images, provided by the CEMIS-OULU Laboratory of the University of Oulu. The images were captured with a setup consisting of a CCD camera and optics with 2.5x magnification. The set consists of 50 grayscale acacia pulp suspension images with a resolution of 800x600 pixels. The concentration of fibers was 0.05 ... 0.10 g in 1 liter of water. Forty randomly selected images (on the average 50 fibers per image) were used for testing and 10 images for learning the method parameters. Examples of the images are presented in Fig. 3.1. The fiber detection and characterization were evaluated based on the spatial ground truth (GT) data verified by an expert. The end points and points of high curvature were marked for each fiber. Examples of the GT markings are presented in Fig. 3.6.

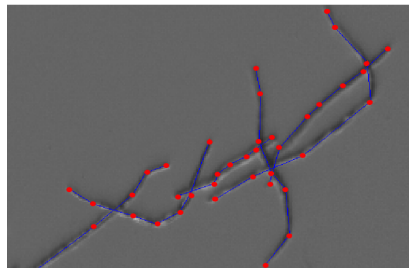


**Figure 3.6:** Examples of the ground truth markings.

### 3.3.2 Results and discussion

**Fiber detection and characterization.** Examples of the computed saliency map, junction map, and polarity map are presented in Fig. 3.7. The more prominent the pixel is, the brighter it is on the map. For example, the brighter pixels on the polarity map correspond to the pixels that are more likely to be end points.

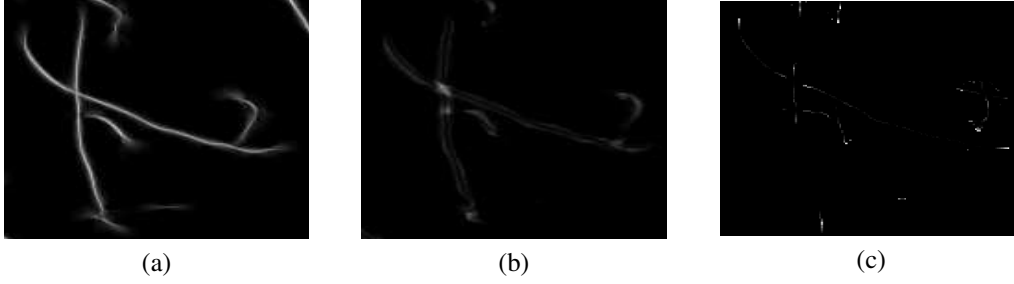


**Figure 3.7:** Examples of saliency maps and polarity: (a) saliency map; (b) junction map; (c) polarity map.

Examples of the detection results are presented in Fig. 3.8. While Fig. 3.8(a) and Fig. 3.8(b) illustrate successful performance, Fig. 3.8(c) and Fig. 3.8(d) reveal difficulties. In Fig. 3.8(c), the fiber separation was performed incorrectly because the fibers intersect at a small angle. In Fig. 3.8(d), the algorithm failed because of the high number of intersecting fibers.

To validate the detection results, for each GT fiber presented by a set of points  $P_{gt} = \{p_1, \dots, p_N\}$ , where  $N$  is the number points, we find a corresponding set  $Q = \{(q_1, l_1), \dots, (q_N, l_N)\}$ , where  $q_i$  is the closest detected point for  $p_i$  and  $l_i$  is the label of a fiber the point  $q_i$  belongs to (see Fig. 3.9). The detection error in pixels is computed as the average euclidean distance between the GT points and the corresponding (closest) detected points  $E = \frac{1}{N} \sum_{i=1}^N (\|p_i - q_i\|)$ . A fiber is detected correctly if  $E < 6$ . We distinguish the following detections:

- the percentage of correctly detected fibers ( $TP$ ),
- the percentage of fibers that were fully detected but in several pieces ( $TP_M$ ), where  $M$  is the number of pieces, and
- the percentage of the detected fibers that are not even a part of a GT fiber ( $FP$ ).

The results are shown in Fig. 3.10. Of the fibers detected 62% were detected correctly in one piece. Moreover, 90% percent of fibers were fully detected in one or two pieces and almost all the fibers were fully detected in maximum of 4 pieces per fiber. The  $FP$  detection rate was 19.2% providing a precision of 80.8%. The average detection error  $E$  equalled to 3.8 pixels.

The length of a fiber presented by a sequence of pixels  $\{(x_1, y_1), \dots, (x_N, y_N)\}$  is computed as the sum of distances between the curve points [90] as

$$L = \sum_{i=2}^N \sqrt{(x_i - x_{i-1})^2 + (y_i - y_{i-1})^2}. \quad (3.6)$$

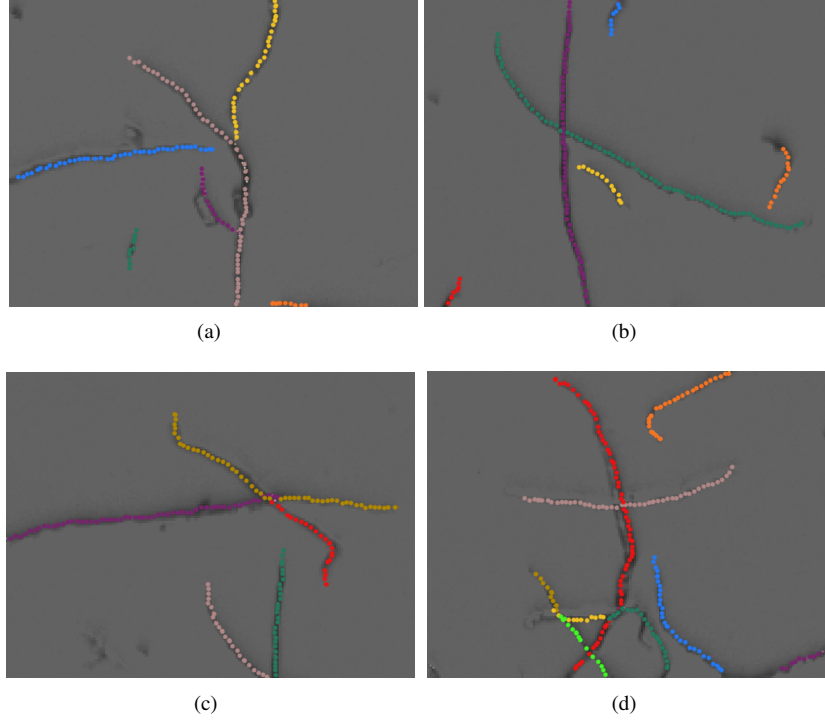


**Figure 3.8:** Examples of fiber detection. The colors are used only for illustrative purposes to visually separate the fibers.

The projected length of a fiber is estimated as the distance between the curve end points [90] as

$$l = \sqrt{(x_n - x_1)^2 + (y_n - y_1)^2}. \quad (3.7)$$

The curl index is calculated using Eq. 3.5. The fiber parameters were computed as average values per image and the accuracy of the fiber parameter estimates was computed as the mean absolute error  $(1 - \frac{P_{GT}-P}{P_{GT}}) \cdot 100\%$ , where  $P_{GT}$  is a GT parameter value and  $P$  is a estimated parameter value. As the result, the fiber length was estimated with an accuracy of 71.5% and the fiber curl index with an accuracy of 70.7%.

**Parameter selection.** The method parameters were selected based on the method performance on 10 randomly selected suspension images. Test set contained the rest of the images. Length accuracy computation was selected as the performance criteria. The experiment was repeated four times and the results are presented in Table 3.1. The length estimation accuracy does not vary significantly in the presented experiments. The parameters selected at each iteration are shown in Table 3.2. The scale of voting determines the size of the voting field and affects the size of the gaps allowed in the curvilinear structures. The average length of fibers was 99 pixels. With the voting scale equal to 10, the biggest allowed gap is about 30 pixels. The thresholds for saliency, polarity, and junction maps affect the process of curve growing. The lower the saliency threshold, the longer the curve. The lower the polarity threshold, the sooner the growing is stopped. The junction threshold determines when the region of intersection starts.

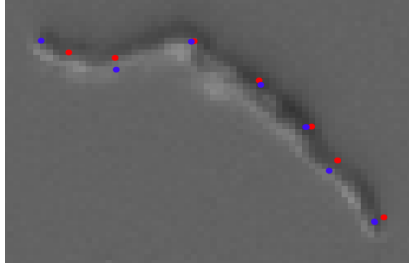


**Figure 3.9:** Example of the ground truth points (red color) and the closest detected points (blue color).

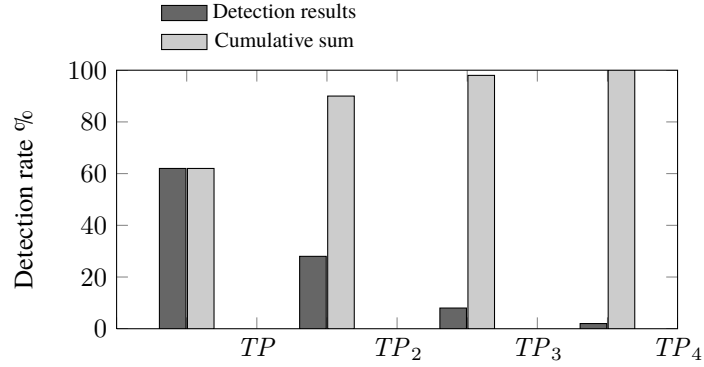


**Figure 3.10:** Detection results.

**Table 3.1:** Accuracy of fiber length computation for parameter selection.

| Experiment                      | 1    | 2    | 3    | 4    |
|---------------------------------|------|------|------|------|
| Training set, mean accuracy (%) | 72.3 | 72.6 | 72.9 | 71.4 |
| Training set, Std (%)           | 9.9  | 6.5  | 8.6  | 9.3  |
| Test set, mean accuracy (%)     | 70.2 | 70.1 | 70.4 | 69.8 |
| Test set, Std (%)               | 6.9  | 7.8  | 7.3  | 6.9  |

**Table 3.2:** Fiber detection method parameters.

| Parameter  | Notation | Exp. 1 | Exp. 2 | Exp. 3 | Exp. 4 |
|--|----------|--------|--------|--------|--------|
| Scale of voting                                  | $\sigma$ | 10     | 10     | 15     | 10     |
| Saliency threshold for seed points selection     | $T1_s$   | 50     | 50     | 50     | 50     |
| Saliency threshold for curve growing termination | $T2_s$   | 10     | 10     | 10     | 10     |
| Minimal polarity of end points                   | $T_e$    | 50     | 45     | 50     | 50     |
| Threshold for junction points                    | $T_j$    | 40     | 40     | 40     | 40     |

In order to show how the accuracy of length and curl index computation varies depending on the parameters, an experiment was performed, fixing all parameters but two (e.g., scale of voting and the saliency threshold) and estimating the length and curl index. Fig. 3.11 demonstrates that the scale of voting and the saliency threshold for growing termination affect most significantly the result. The selected parameters are marked by red color. Since the length accuracy estimation was utilized as a criteria for parameter selection the selected parameters not always guarantee the highest accuracy of the curl index estimation (e.g., in the experiment varying the saliency threshold and the scale of voting). In some cases (e.g., in the experiment varying the saliency threshold and the junction threshold), the accuracy of the length estimation varies only insignificantly. It means that when the fixed parameters are set to a certain value, the effect of the varying parameters is not dramatic. Another possibility is that the parameter value sampling could be more dense or the interval could be extended to reveal more information. However, only slight variation of the results in some cases could also mean that the results would not change significantly when the parameters are varied.

### 3.4 Summary

A general framework for curvilinear structure detection including a novel linking method was presented. The framework was applied to fiber characterization in pulp suspension images. The method was shown to detect all the fibers in the set of used images but 38% of them in multiple pieces leading to a true-positive rate of 62%. The demonstrated precision of fiber detection was 80.8%. The average fiber length was estimated with an accuracy of 71.5% and the average fiber curvature with an accuracy of 70.7%. Problems occur when a single fiber is detected as several pieces causing false positive detections and the fiber parameter to be computed incorrectly. The fiber consistency was still quite low in this research. Therefore, if the method is used in an industrial application with higher consistencies additional testing and possible method development are needed. Future work will include the further development of the curve growing algorithm and the application of the framework to other similar problems.

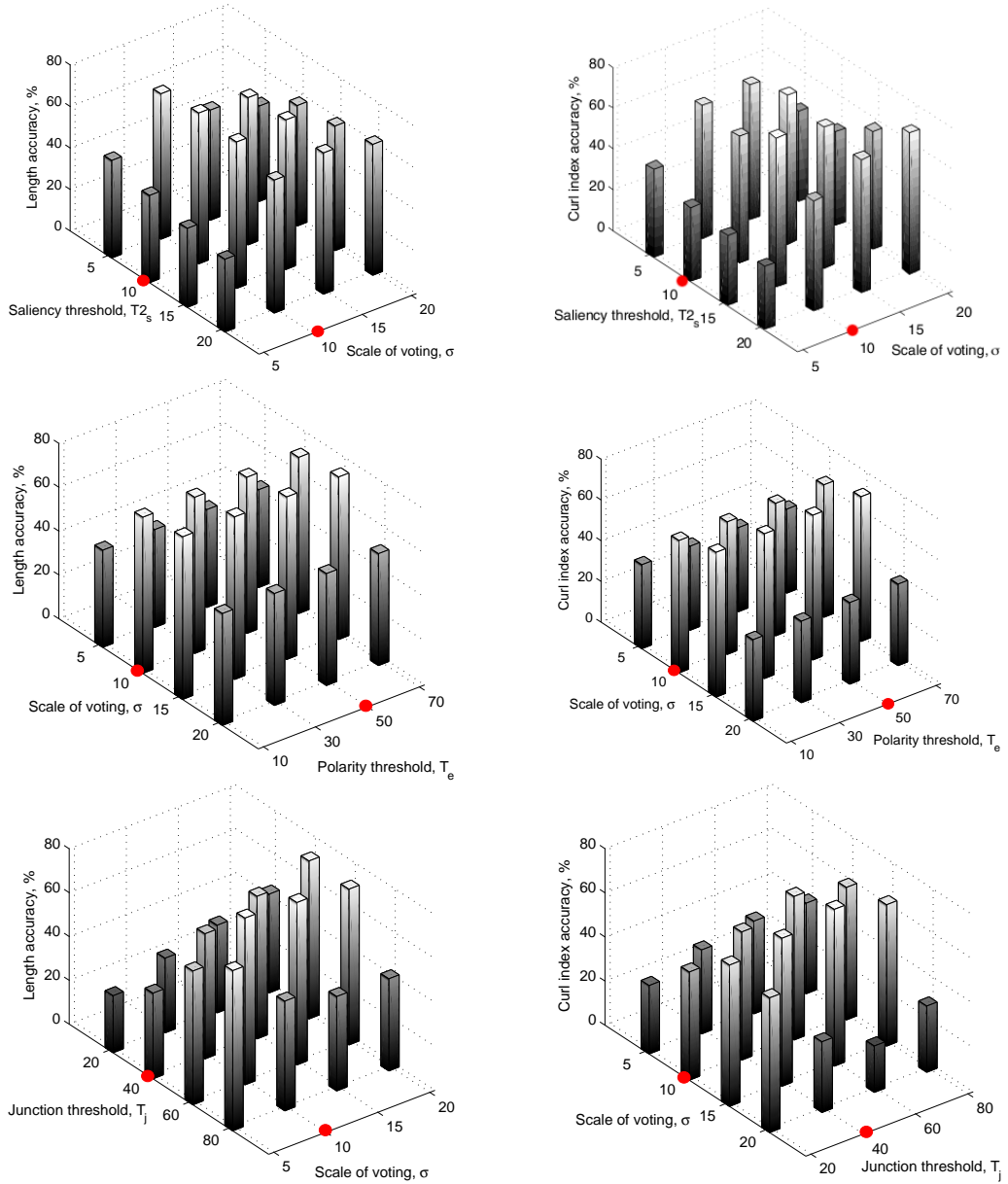


**Figure 3.11:** Parameter sensitivity experiments varying only two parameters at a time. The selected parameter values are marked by red color.

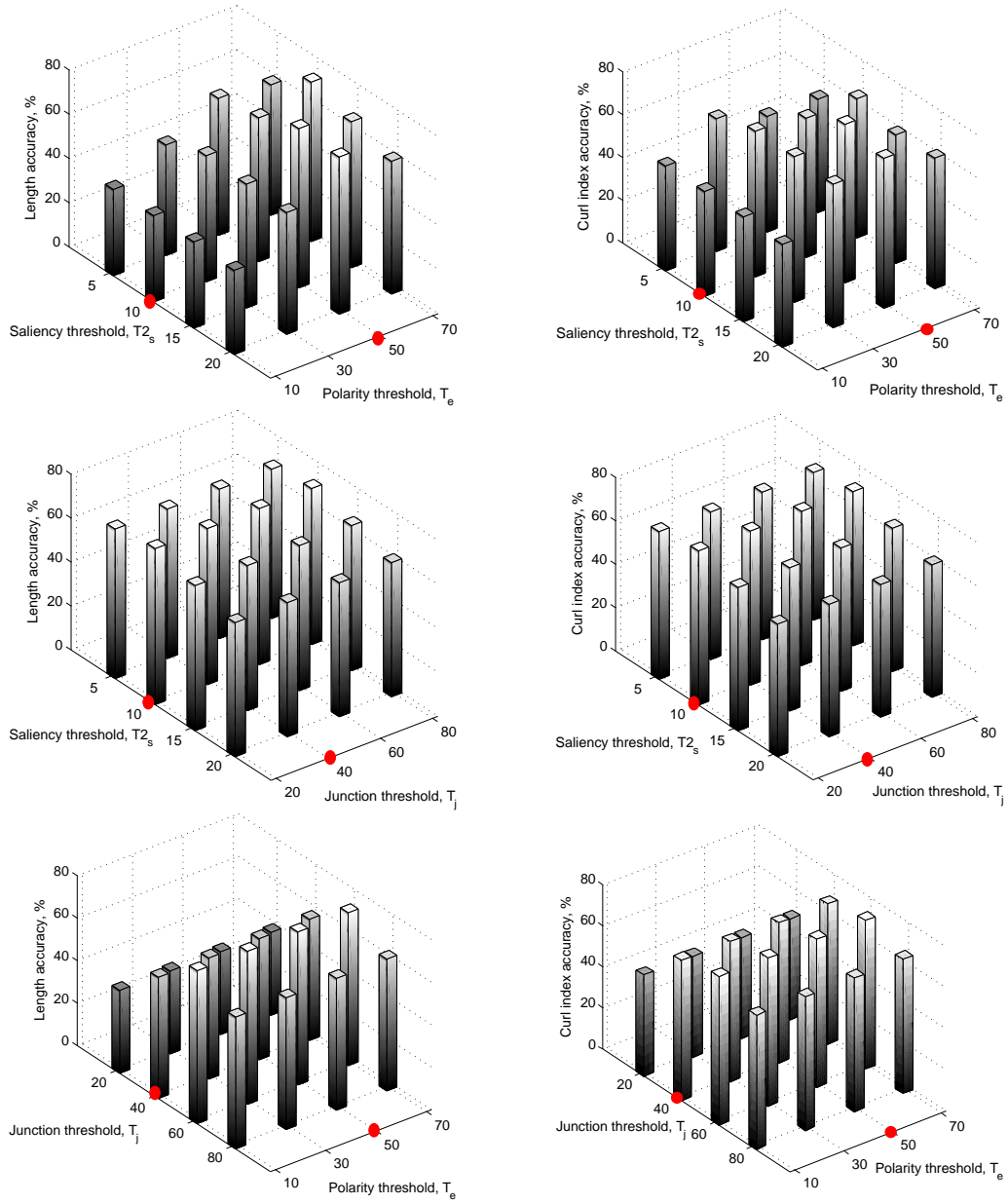


**Figure 3.11:** (Continued) Parameter sensitivity experiments varying only two parameters at a time. The selected parameter values are marked by red color.



---

## Gas volume estimation in pulp suspension

---

### 4.1 Problem statement and previous work

Gas volume in pulp suspensions is an important factor in the decision to terminate the bleaching stage of pulp processing [12]. The imaging of pulp bleaching at the industrial scale is a recent technique and the author is not aware of prior work in the area. Such imaging, together with automatic image analysis, has the potential to significantly impact the pulp production economy as the just-in-time termination of the pulp bleaching process considerably saves energy and materials.

In pulp suspension the gas is contained in bubbles, as can be seen from the examples in Fig.4.1. This motivates the author to solve the task of volume estimation as a bubble detection problem. Under different lighting conditions, the appearance of bubbles varies from a pair of ring-like, bright ridge edges to blurred dark edges with contrast reversal and multiple inter-reflections. Experiments show that oriented filter responses caused by such objects are well modeled by con-

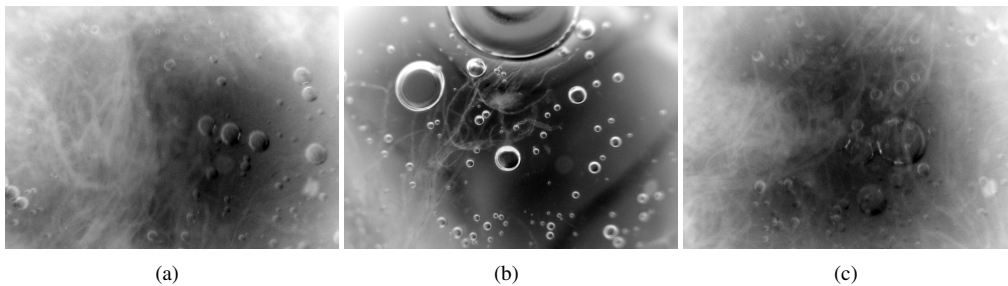


**Figure 4.1:** Examples of the original pulp suspension images (provided by FiberLaboratory).

centric arrangements of circular arcs, see Fig. 4.2. In this work the set of concentric circular arcs is noted as Concentric Circular Arrangement (CCA), that are modeled by an annulus parametrized

by a radius, a center, and an annulus width. Therefore, the bubble detection problem is formulated as a search for CCA. The problem is solved in a hypothesize-optimize-verify framework, sampling from the connected components of linked non-maximum suppressed responses of oriented ridge filters. The latter two steps use a novel cost-function and the simplex optimization method [72] for precise center and scale estimation.

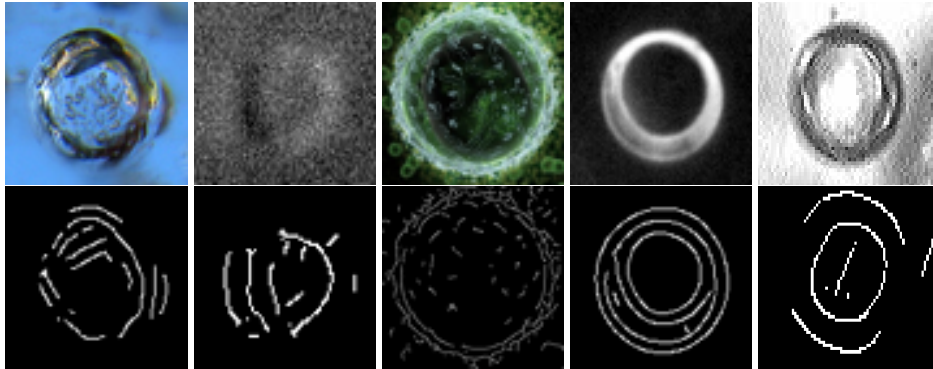


**Figure 4.2:** Examples of images of bubbles and local maxima (in spatial and orientation domains) of oriented ridge filters.

The problem of bubble detection appears in a number of applications, such as the dispersion of oil drops in water [13] and air bubble detection in dense dispersion [105]. Bubbles or drops manifest themselves as roughly circular objects, which motivates the researchers to solve the problem as the detection of circles. There are two common approaches that are used to detect circular objects: geometry-based and appearance-based approaches. In the geometry-based approach (see Fig.4.3(a)), a circular model parameterized by its center  $c = (x_c, y_c)$  and radius  $r$  is fitted to the image edge map. In the appearance-based approach, a template of a bubble is created, the test grayscale image is convolved with the template, and the local maxima of the convolution are sought. An example of such a template is shown in Fig. 4.3(b).

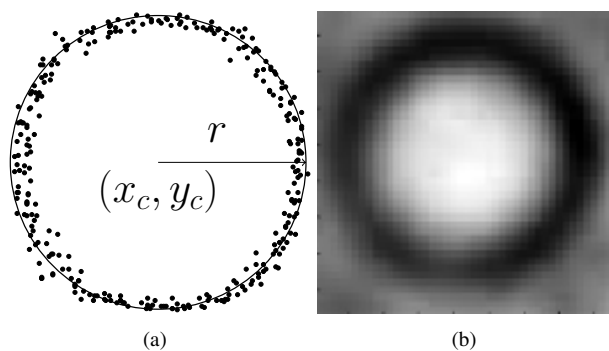


**Figure 4.3:** Detection of circular objects: (a) Circular model fitting; (b) An example of a bubble template [105].

### 4.1.1 Geometry-based approaches

The geometry-based approaches typically use a voting technique, such as the Hough Transform (HT) [17] or its modifications [53]. The HT for circle detection [104] describes a circle by its center coordinates  $(x_c, y_c)$  and radius  $r$  as

$$(x - x_c)^2 + (y - y_c)^2 = r^2. \quad (4.1)$$

Each point  $(x_i, y_i)$  in an image corresponds to a circular cone in the  $(x_c, y_c, r)$  parameter space. If points lie on one circle, their cones in the parameter space will intersect in one point that describes the center coordinates and the radius of the circle. To address the main weaknesses of the HT, such as computational complexity and storage requirements, several revisions of the basic HT have been proposed (see e.g. [44]). The Randomized and Probabilistic Hough Transforms utilize random sampling techniques to sample the hypothesis of the circles from the edge pixels and remove verified hypotheses from the image to accelerate the process. HT and its modifications have been utilized in several applications (e.g., segmentation of spherical particles in transmitted light image stacks [77], segmentation of bubbles and drops in complex dispersions in bioreactors [91], and detection of circular objects in pulsative medical video [75]).

In [68], Pan et al. use the gradient information to produce a projection line in the  $(x_c, y_c, r)$  space from each edge pixel (see Fig.4.4). If the projection lines of two pixels intersect in one point, they belong to the same circle. This is, however, rare in real life images. If the projection lines of two pixels do not intersect, they produce a hypothesis of a circle. The likelihood of each such hypothesis is modeled as a Gaussian distribution dependent on the distance between the two projection lines, equal to the length of a line perpendicular to the both projection lines.

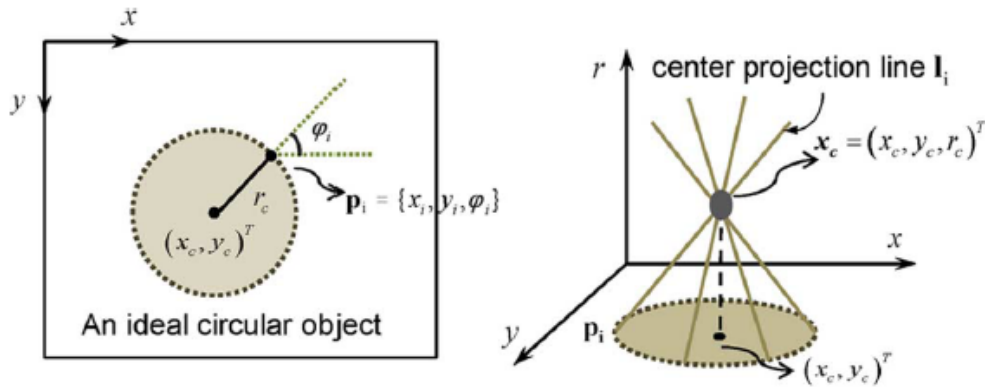


**Figure 4.4:** Circular object detection with probabilistic pairwise voting [68].

The score of a hypothesis is computed by marginalization over all edge point pairs that contribute to the hypothesis. The method has been shown to give good results in human iris detection, but only examples of the algorithm's performance on other natural images have been presented.

In [91], Taboada et al. presented a semi-automatic image analysis method for the segmentation of bubbles and drops. In the method, false positives were manually removed after CHT. The work was continued by [13] who focused on the detection of oil drops in dispersion images and

automatic elimination of the false positives. Since the oil drops were not the only circular objects in the images, the authors designed a feature to distinguish between the oil drops and other objects. They exploited the average value of the difference between the exterior and the interior gradient orientations with respect to the drop border. The classification procedure utilizing the designed feature was applied after the HT, and the classifier was trained by using the preselected oil drop hypotheses generated by the HT.

In the method presented in [10], a random line generated in an input image intersects with two pixels producing a hypothesis of a circle. The HT accumulator space is incremented with the value which measures the degree of matching between the gradient directions in the sampled points. Although the method demonstrated good results, it would be problematic to apply it to objects with multiple ridge edges since they produce the hypotheses with multiple different radii.

#### 4.1.2 Appearance-based approaches

The appearance-based approach works with grayscale images, or in some cases, with edge maps. The approach is based on the sliding-window approach [95], where a template of the object of interest is created and the grayscale image is convolved with the template. In order to find the objects, the maxima of the filtration responses are searched.

An appearance-based approach for bubble detection has been employed by [105]. Based on the visual evaluation of the results, the method outperformed the standard HT. The authors improved the standard appearance-based approach by convolving the image at multiple scales, by utilizing multiple prototypes (templates) of a bubble, and by detecting the rotated prototypes. However, the authors reported a relatively large computational time for the correlation step.

#### 4.1.3 Drawbacks of the existing methods

Despite the fact that the existing solutions for circular object detection are used in a number of applications, they do not provide a unified framework for bubble-like object detections, providing high accuracy and precision. The CHT-like approaches suffer from a large number of false positives and are sensitive to noise. Moreover, they do not take into account the appearance of the bubbles as an object with multiple light inter-reflections. Template matching techniques are difficult to apply to bubble detection since the bubbles appear differently (bright ring-like edge or dark moon-like shape, see Fig. 4.1(a)) in the suspension, depending on bubble location and lighting. Furthermore, increasing the number of templates dramatically increases the computation time.

### 4.2 Detection of bubbles as Concentric Circular Arrangements (CCA)

The steps of the proposed CCA detection are illustrated in Fig. 4.5 and summarized in Algorithm 4. Due to the fact that bubbles manifest themselves as objects with ridge edges, the first step in CCA detection is to perform direction-sensitive filtering with second derivative zero-mean Gaussian filters in eight directions. In order to estimate the direction of an edge more precisely and to obtain better non-maximum suppression results, an algorithm of the dominant orientation selection described in Section 4.2.1 is applied. After that, the standard algorithm of the non-maximum suppression of edges [9] is applied together with the thresholding of the filter response. As the result, an oriented edge map of the grayscale image is obtained.

In the second stage, the hypotheses of CCA centers and radii are established and optimized with respect to the cost-function proposed in Section 4.2.2. Finally, the hypotheses are selected based on their scores.

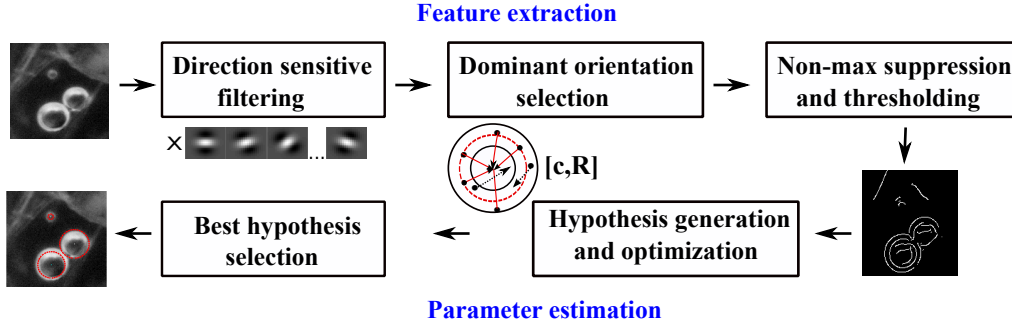


Figure 4.5: The proposed method for bubble detection.

---

**Algorithm 4** The CCA bubble detection approach

---

**Input:** a grayscale image  $I$ , a set of filter masks  $M = \{M_j\}$  (see Fig. 4.5)

**Output:** a set of detected CCA  $H = \{h_i = [c_i, R_i, f_i]\}$  with center  $c_i$ , radius  $R_i$ , and support  $f_i$ .

**Parameters:** threshold for filter response  $T$ , number of sectors  $N_s$ , minimal length of an arc  $L_{min}$ , width of an annulus  $\theta$ , minimal sector support  $T_s$ .

- 1: Filter the image with a set of oriented masks:  $R_j = I * M_j$ .
  - 2: For each pixel  $p_i(x_i, y_i)$ , select the dominant orientation  $d_i$ , corresponding to the maximum response of the filtration  $q_i = \max(R_j(x_i, y_i))$ .
  - 3: Perform non-maximum suppression of the pixel values in the dominant orientation.
  - 4: Threshold the filter response values by setting pixels with the filter response lower than  $T_{filt}$  to zero.
  - 5: Generate, optimize, and select the CCA hypotheses (Algorithm 5 with parameters  $N_s, L_{min}, \theta, T_s$ ), obtaining the set of CCA  $H$ .
- 

#### 4.2.1 Oriented edge map computation

Since bubbles manifest themselves as objects with ridge edges, the solution for ridge detection from [58] was adopted. The images are filtered by a second derivative zero-mean Gaussian filter in eight directions (see the filter masks in Fig. 4.5). For further processing, the absolute value of the responses is taken to capture both bright and dark edges. Generally, the dominant orientation of the edge normal in each point is computed as the maximum of the eight filter responses. In some cases, however, an edge has multiple dominant orientations. For example, in Fig. 4.6(a), the edge orientation can be clearly determined, while in Fig. 4.6(b), instead of a single maximum there is a flat region where it is unclear which orientation should be considered as the dominant

one. It is also possible that there are two dominant orientations (see Fig. 4.6(c)). This may occur, for example, when two bubble edges are intersecting. To solve these problems, the following heuristics are applied: (i) in the case of a single local maximum (see Fig. 4.6(a)), the dominant orientation corresponds to the maximum; ii) if the difference between two successive highest values is lower than 5% of the highest value (see Fig. 4.6(b)), the dominant orientation is determined as the mean value between the first and the second maxima; iii) in the case of two dominant orientations, the first is selected.

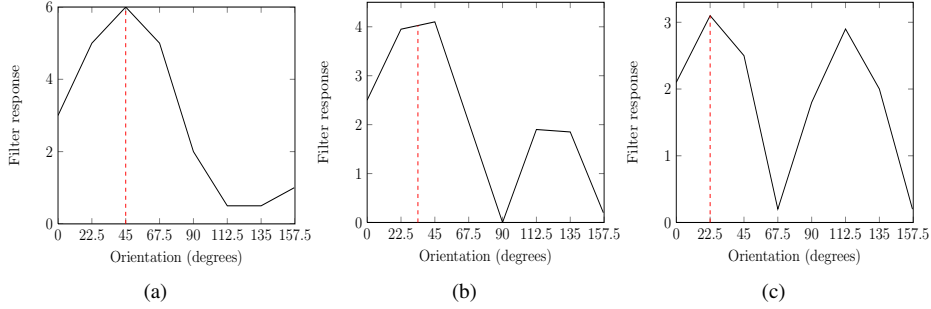


**Figure 4.6:** Edge orientation examples: (a) One dominant orientation; (b) Flat maximum region; (c) Two maxima;

After the orientation of each edge pixel has been computed, the non-maximum suppression [9] is performed as demonstrated in Fig.4.7. When two neighboring pixels in the dominant orientation have a filter response lower or equal to the current pixel, their values are set to zero. The values with the filter response lower than the threshold  $T_{filt}$  are set to zero as well.

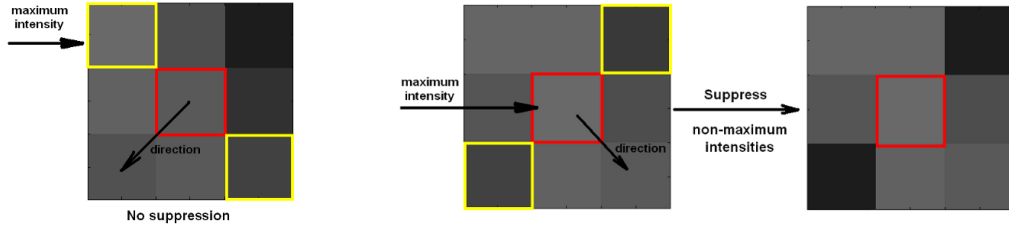


**Figure 4.7:** Non-maximum suppression.

#### 4.2.2 CCA hypothesis generation, optimization, and selection

The hypotheses are generated using the RANSAC procedure modified from [23]. The triples of points needed to specify circular regions are sampled non-uniformly from the edge arcs (connected components). In the previous work [87], a hypothesis of a bubble was generated when the normals at the three sampled edges were pointing approximately to the same center, in other words, supporting the hypothesis. In this work, this requirement is extended by determining the number of directions from which a hypothesis gets support in order to ensure the evidence of a

bubble from multiple directions. The edges, voting for a hypothesis  $H$  with radius  $R$ , are divided into  $N$  sectors. The decision, whether the hypothesis should be rejected, is made based on the value

$$\tau = \frac{N_s}{R}, \quad (4.2)$$

where  $N_s$  is the number of sectors supporting the hypothesis. If  $\tau$  is lower than the threshold  $T_s$  then the hypothesis is rejected. The smaller the bubble is, the less supporting sectors are needed in order to accept the hypothesis.

The contribution of an edge point  $p(x_p, y_p)$  with an orientation  $\alpha_p$  to support a CCA center  $c(x_c, y_c)$  is defined as

$$f_p = g(\Delta\alpha) \cdot q(r), \quad (4.3)$$

where  $r = \sqrt{(x_c - x_p)^2 + (y_c - y_p)^2}$  is the Euclidean distance from the edge  $p$  to the center  $c(x_c, y_c)$ ,  $\Delta\alpha = |\alpha_p - \arctan(\frac{x_c - x_p}{y_c - y_p})|$  is the absolute difference between the edge direction  $\alpha_p$  and the direction of the edge normal pointing to the center (see Fig. 4.8(a)). The parameter  $\theta$  [4], shown in Fig. 4.8(a), is learned from the training data. It determines the width of the annulus from which the arcs are sampled. The weight function for the edge distance from a center  $q(r)$  is presented in Fig. 4.8(b). Its shape reflects the fact that the inner structure of a bubble also votes for a hypothesis. The weight function for the edge direction is computed as  $g(\Delta\alpha) = \frac{1}{1+\Delta\alpha}$  to give less weight to the edges with inconsistent orientation.

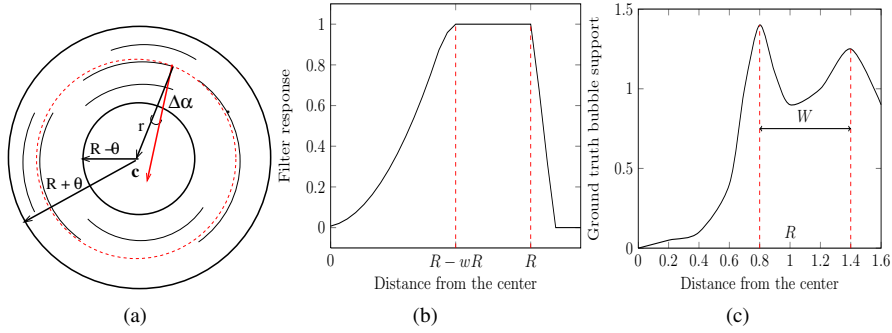


**Figure 4.8:** CCA: (a) The model; (b) The weight function for the edge distance from the center; (c) Average bubble support at the different distances from the center.

For each CCA hypothesis, a function

$$f_h = \frac{1}{R} \sum_{i=1}^N f_{p_i} \quad (4.4)$$

is computed:  $N$  is the number of supporting edges and  $R$  is the hypothetical radius. For each CCA hypothesis, the center and the radius are optimized by maximizing the support function  $f_h$  with the Nelder-Mead Simplex method [72].

Finally, the non-maximum suppression is performed on the CCA parameters to prevent multiple hypotheses for a single bubble. A hypothesis  $h_i = [c_i, R_i, f_i]$  is rejected if there is a hypothesis  $h_j = [c_j, R_j, f_j]$  such that  $|R_i - R_j| < 0.5R_j$ ,  $|c_i - c_j| < 0.5R_j$ , and hypothesis  $h_j$  received greater support than hypothesis  $h_i$ .

**Algorithm 5** Bubble hypothesis generation, optimization, and selection**Input:** an oriented edge map  $\mathbf{E}$ .**Output:** a set of CCA hypotheses  $\mathbf{H} = \{\mathbf{h}_i = [c_i, R_i, f_i]\}$  with center  $c_i$ , radius  $R_i$ , and support  $f_i$ .**Parameters:** minimal length of an arc  $L_{min}$ , width of an annulus  $\theta$ , minimal sector support  $T_s$ .

- 1: Determine the set  $\mathbf{C}$  of edge arcs of length  $l \geq L_{min}$  for CCA hypothesis generation.
- 2: **for** all the randomly selected arcs from  $\mathbf{C}$  **do**
- 3:     Choose three edge pixels belonging to the arc.
- 4:     Generate a CCA hypothesis  $H_i$  from the triplet within an annulus  $[R_i - \theta, R_i + \theta]$  as a least-squares estimation problem.
- 5:     For the hypothesis  $H_i$ , compute the sector support  $\tau_i$  (Eq. 4.2) and keep the hypothesis if  $\tau_i \geq T_s$ .
- 6:     Optimize the center and the radius of the CCA hypothesis with the Neadler-Mead simplex method.
- 7:     Compute the hypothesis support function  $f_i$  (Eq. 4.4).
- 8: **end for**
- 9: Sort the hypotheses according to  $f_i$  in the descending order.
- 10: **for** all the hypotheses in the ordered set **do**
- 11:     Remove the pixels supporting the stronger hypotheses from the support of the weaker hypotheses
- 12:     Recompute the hypothesis support  $f_i$ .
- 13: **end for**
- 14: Do maximum suppression of the CCA hypothesis: reject a hypothesis  $[R_i, c_i, f_i]$  if there is a hypothesis  $[R_j, c_j, f_j]$  such that  $|R_i - R_j| < 0.5R_j$ ,  $|c_i - c_j| < 0.5R_j$ , and  $f_i < f_j$ .

### 4.3 Experiments and discussion

The first group of the experiments was performed on the pulp suspension images to compute the gas volume. The performance of the CCA method was compared to the standard Circular Hough Transform and the sliding window approaches. The second group of experiments included validation of the method performance on other types of data: in this work, oil dispersion images and wet foam images.

#### 4.3.1 Gas volume estimation in the pulp bleaching process

##### DATA AND METHOD PERFORMANCE EVALUATION

The experiments were performed on 23 fully annotated microscopic images with a resolution of 1600x1200 pixels (see Fig. 4.1(a)). The images, provided by the FiberLaboratory, were obtained from the pilot mixing setup. In total, 1141 bubbles in the images were marked as circles by an expert. The ground truth volume was computed from the marked bubbles. The data was divided into a training set containing eight randomly selected images (397 bubbles) and a test set containing the rest of the images, 15 images (744 bubbles). The volume estimation error was selected as the performance criteria. The mean relative error of volume estimation for  $M$  images

was computed as

$$V_{err} = \frac{1}{M} \sum_{i=1}^M \left( \frac{|V_{est_i} - V_{gt_i}|}{V_{gt_i}} \right), \quad (4.5)$$

where  $V_{gt_i}$  is the ground truth volume and  $V_{est_i}$  is the estimated volume. The experiment was repeated 4 times and the results corresponding to the selected parameter set are presented in Table 4.1. The selected parameters are presented in in Table 4.2. There is no big variation in the parameters selected in four different experiments. The variation of the gas volume estimation error  $V_{err}$  can be caused by the fact that the quality of the images is different and the result depend on what images were selected for training.

**Table 4.1:** Volume estimation error for parameter selection.

| Experiment                      | 1  | 2  | 3  | 4  |
|---------------------------------|----|----|----|----|
| Training set, mean accuracy (%) | 18 | 19 | 28 | 10 |
| Training set, Std (%)           | 21 | 21 | 20 | 17 |
| Test set, mean accuracy (%)     | 20 | 19 | 15 | 24 |
| Test set, Std (%)               | 20 | 21 | 19 | 23 |

**Table 4.2:** The CCA method parameters.

| Parameter   | Notation   | Exp. 1 | Exp. 2 | Exp. 3 | Exp. 4 |
|---|------------|--------|--------|--------|--------|
| Number of CCA sectors   | $N$        | 7      | 8      | 7      | 7      |
| Maximum radius of bubbles, mm                                 | $R_{max}$  | 1.52   | 1.52   | 1.52   | 1.52   |
| Filter response threshold                                     | $T_{filt}$ | 0.90   | 0.85   | 0.90   | 0.85   |
| Width of the annulus  | $\theta$   | 0.3R   | 0.3R   | 0.3R   | 0.3R   |
| Minimum length of an arc from which a hypothesis is generated | $L_{min}$  | 20     | 20     | 20     | 20     |
| Sector support threshold                                      | $T_s$      | 0.09   | 0.10   | 0.09   | 0.09   |
| Parameter of the cost-function                                | $W$        | 0.6R   | 0.6R   | 0.6R   | 0.6R   |

The maximum radius of the bubbles was experimentally found from the ground truth to be 80 pixels. Given the number of CCA sectors and the maximum radius, the sector support threshold  $T_s$  was computed such that the support for the largest bubbles come from all the sectors. In the proposed method, a bubble hypothesis collects the votes from the edges according to their location and orientation. In order to restrict the location of the edges that can vote for the hypothesis, all the edges within a certain radius are considered and their votes are weighted using a weight function presented in Fig. 4.8(b). The weighting function depends on the parameter  $W$ , width of the edge, which was learned from the training data as well. The support that the ground truth bubbles receive at different distances from the center was studied. The edge width  $W$  is the average width of the ground truth bubbles, as it can be seen from Fig. 4.8(c), where two peaks denote the beginning and the end of a bubble edge profile.

In order to estimate the error landscape, gas volume estimation error  $V_{err}$  was computed fixing all parameters but two at a time and varying the two parameters. Fig. 4.9 demonstrates the results. The error varies smoothly in some areas, but there are peaks corresponding to high error values. It could be explained by the fact that there is a big variation in the provided images and with certain parameter values in some of the images the error significantly increases. There is also a

problem with big bubbles that could be mistakenly detected with some parameter configurations and can cause big gas volume estimation error. It should be also mentioned that the number of test images is quite low and additional testing is needed on more data. More dense sampling of the parameter values could also help to reveal more detailed information about the results.

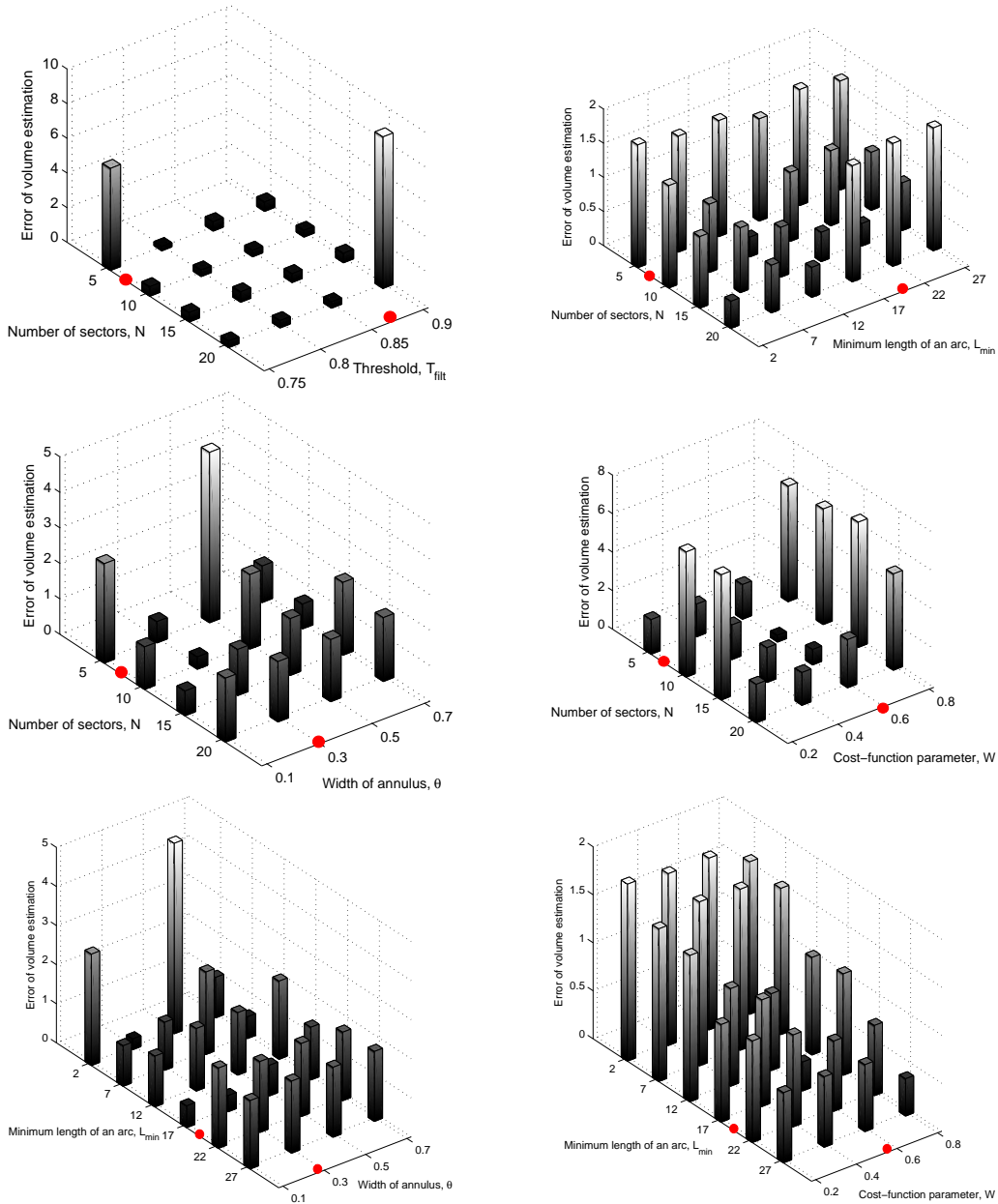


**Figure 4.9:** Parameter sensitivity experiments: varying two parameters at a time. The selected parameter values are marked by red color.

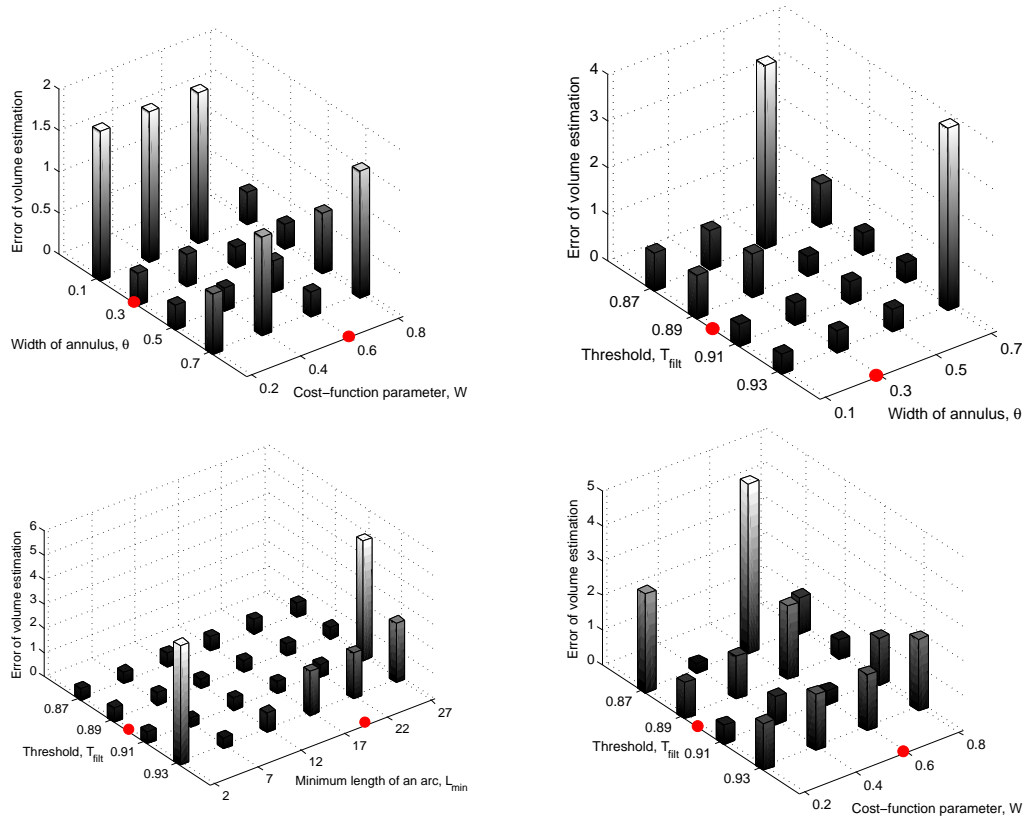


**Figure 4.9:** (Continued) Parameter sensitivity experiments: varying two parameters at a time. The selected parameter values are marked by red color.

## RESULTS AND DISCUSSION

The volume of a bubble with radius  $R$  was calculated as  $V = \frac{4}{3}\pi R^3$ , assuming that the bubbles have an approximately spherical shape. The experiments were performed on the test set. A bubble was considered as correctly detected if the distance of the centers of the detected and expert-marked bubble, and the difference of radii were less than 15% of the radius of the "ground truth" bubble. A "ground truth" bubble was matched with at most one detected bubble. To evaluate the results, the following notation is used:

- True Positive (TP) - a detected bubble is present in the ground truth;
- False Positive (FP) - a detected bubble is not found among the ground truth bubbles; and
- False Negative (FN) - a bubble from the ground truth was not detected.

The histograms of bubble sizes, summed over all images, for the ground truth bubbles, for the detection results, and for TP are shown in Fig. 4.10(a) and 4.10(b). Comparing the two histograms for the number of bubbles and the gas volume, it can be seen that although the number of

bigger bubbles (i.e., bubbles with radius larger than 1 mm) is small, the gas contained in them is considerable. For this reason, it is important that the bigger bubbles are detected correctly.

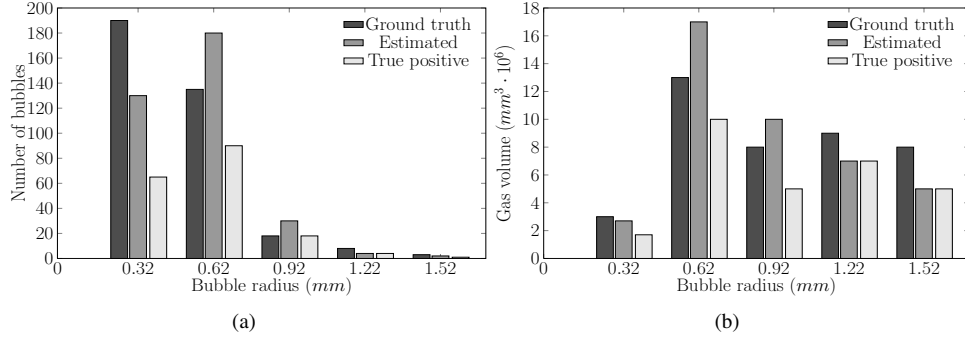


**Figure 4.10:** Detection of bubbles in pulp suspension images: (a) Number of bubbles as a function of a size; (b) Bubble volume as a function of a size.

In the dataset, most of the big bubbles (radius larger than 1 mm) were detected correctly. The size range 0.6 mm – 1 mm includes FP detections, but no FNs. In the small bubble range ( $< 0.5$  mm), both FP and FN are present. In the intended application, the precision of the gas volume estimation is the key parameter. Therefore, the importance of different size groups is shown in Fig. 4.10(b). It should be noted that the large bubbles are as important as the small ones which might be missed when looking just at Fig. 4.10(a). The mean relative error of volume estimation for  $M$  images was computed as  $\frac{1}{M} \sum_{i=1}^M \left( \frac{|V_{est_i} - V_{gt_i}|}{V_{gt_i}} \right)$ , which equals to 19% with standard deviation 21% and precision  $\frac{1}{M} \sum_{i=1}^M \left( \frac{V_{tp_i}}{V_{est_i}} \right)$  of 63%. The precision value was imputed separately for the central parts of the images (676x676) and equals to 86%. The problem appears because the peripheral parts of the images are out of focus, as can be seen from the examples in Fig. 4.1(a). This produces FP detections.

The method works well for bubbles complying with the model (i.e., for bubbles with bright ridge edges as shown Fig. 4.11). However, small blob-like bubbles without a clear ridge edge are often undetected because they manifest themselves as blobs rather than objects with ridge edges, as shown, for example, in Fig. 4.11(a). Fortunately, such small bubbles contain very little gas, and therefore, these FNs have a notable effect only on the estimation of the bubble size distribution. Similar FNs are caused by fibers obscuring the bubbles as in Fig. 4.11(b). The presence of fibers in the images is also a source of false positives, as shown in Fig. 4.11(c) and Fig. 4.11(d). Examples of different images with the corresponding estimated gas volume error are illustrated in Fig 4.12.

The method was implemented in Matlab. Using a PC with a 2.6 GHz CPU, the running time can take a couple of minutes per image depending on the number of bubble hypothesis. With the selected optimal combination of parameters the computational time was about 40s per image. The computational time breakdown was as follows: orientation sensitive filtering 36%, non-maximum suppression 4%, thresholding and linking 4%, hypothesis sampling 5%, hypothesis optimization 50%, hypothesis selection 1%.

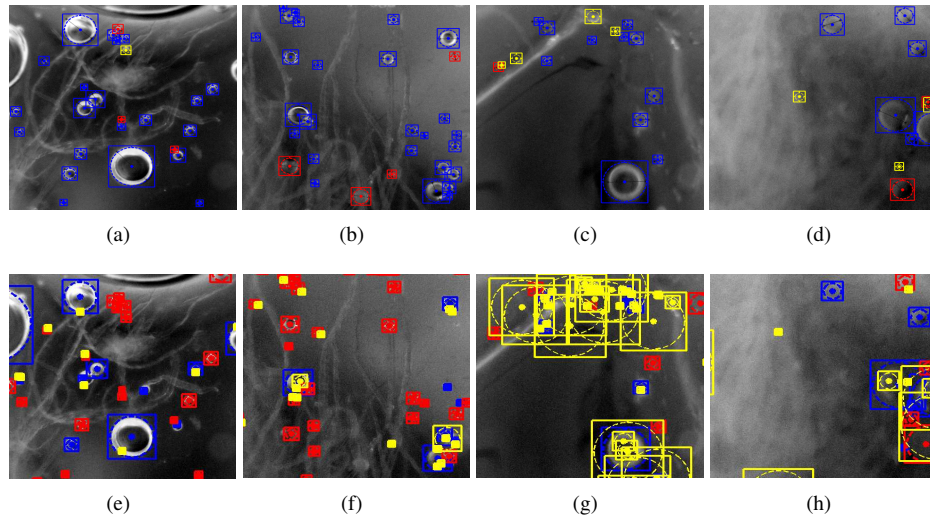


**Figure 4.11:** Detection of bubbles in pulp suspension images: (a)-(d) The CCA method; (e)-(h) CHT for bubble hypothesis generation (true positives (blue), false negatives (red), false positives (yellow)).

In order to see how the bubble hypothesis generation affects the results, the module of the hypothesis generation is substituted with the standard Circular Hough Transform, implemented as a Matlab toolbox in [103]. After the generation, the hypotheses were optimized and selected in the same way as in the original framework. The obtained results were as follows: the mean relative error of the volume estimation was 56% with the precision of 31%. Examples of comparative results are presented in Fig. 4.11. As it was expected, the number of false positives is high which can be also seen from the precision value.

#### 4.3.2 Gas volume estimation with a sliding window approach

A sliding window approach is a competitive method for object recognition and in this thesis it was experimented with the WaldBoost classifier for bubble detection. The results were provided by the Image and Video Processing Research Group of the Brno University of Technology utilizing their implementation of the method for object detection [43]. Half of randomly selected bubbles (570 bubbles) were used for training and half for testing. Each bubble from the training set was randomly rotated 10 times to enlarge the training data set. The following window sizes were used for detection:

- 20 px dataset - scales from 20 to 30 px;
- 30 px dataset - scales from 30 to 60 px; and
- 60 px dataset - 60 px and above.

Using a smaller window size was not feasible since the window does not contain enough features then, which leads to false detections. Three detectors were trained for each window size utilizing

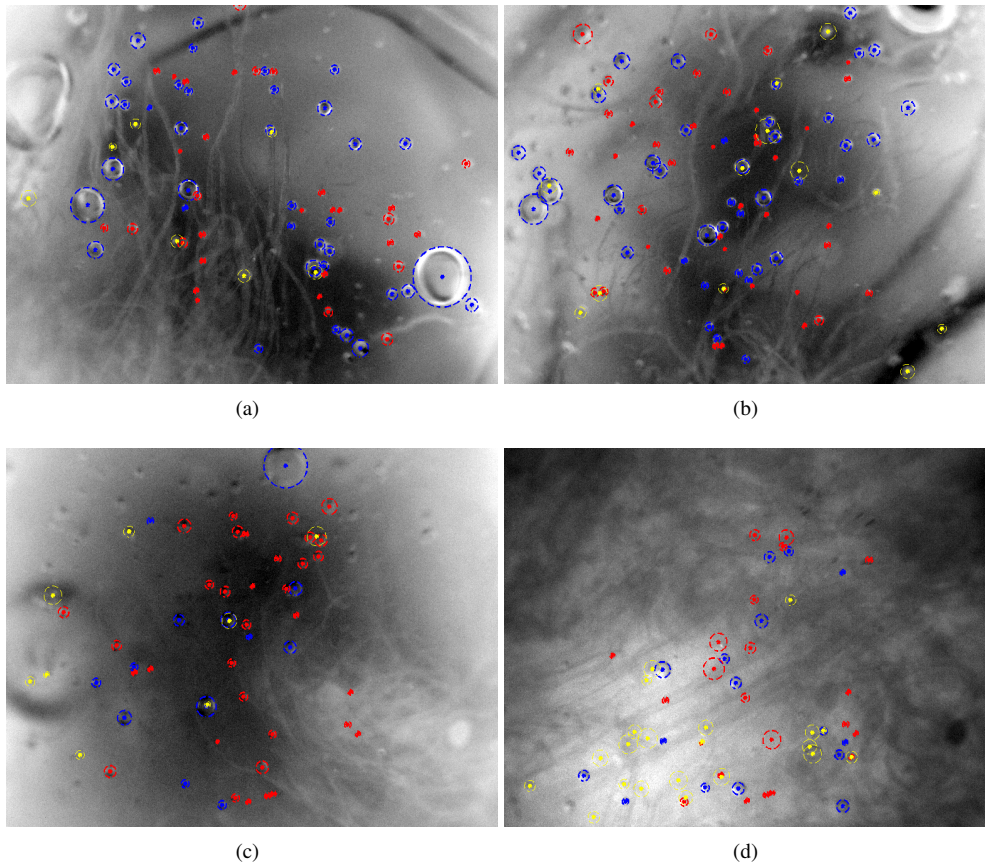


**Figure 4.12:** Bubble detection with the CCA method: (a) Gas volume estimation error of 3%; (b) Gas volume estimation error of 13%; (c) Gas volume estimation error of 10%; (d) Gas volume estimation error of 38% (true positives (blue), false negatives (red), false positives (yellow)).

the Waldboost classification algorithm [80] and LBP feature extractor [67]. Each classifier used 512 features. The target false negative rate was fixed to  $\alpha = 0.01$ , and each detector was trained and tested independently.

The responses of the three classifiers on the test data are obtained, merged and clustered to remove multiple detections. The average of every cluster with at least two detections is assumed to be a detected bubble. The detections are compared to the annotation and true positives, false positive, and false negatives are counted. As the three classifiers are independent, detection thresholds must be adjusted independently. There were three thresholds tuned from -2 to 6, and evaluation was performed for every combination. The best combination was selected according to F-measure from all combinations.

Precision Recall (PRC) and Receiver Operating (ROC) curves of different threshold settings are shown in Fig. 4.13, bubble counts and volume are presented in Fig. 4.14, and detection examples

are demonstrated in Fig. 4.15. The best setting of the detectors gives 286 true positive detections (correctly detected bubbles), 166 false negative detections (missed bubbles), and 98 false positive detections (patterns detected as bubbles but not annotated). There were 452 annotated bubbles in the testing images. In order to get about 65% of TP, about 100 extra bubbles are detected. In Fig. 4.15(b), one can see that with the precision of at least 75% the accuracy drops to about 65%. In Fig. 4.15, examples of bubble detection are presented. One can see that since there is no procedure for bubble parameter optimization radii are not always detected precisely. The histograms of bubble detection and volume estimation are demonstrated in Fig. 4.14. The mean average error of volume estimation is 45%, which can be seen from the volume histogram in Fig.4.14(b). The best detection results were obtained for the histogram bins corresponding to the window size. Thus, the method is sensitive to the window size. The sliding window approach allows to detect smaller bubbles more precisely, however, the volume was estimated with bigger error (45%) than by the CCA method (19%). The current C++ implementation of the sliding window approach takes about 20s per test image, which is comparable to the CCA method.

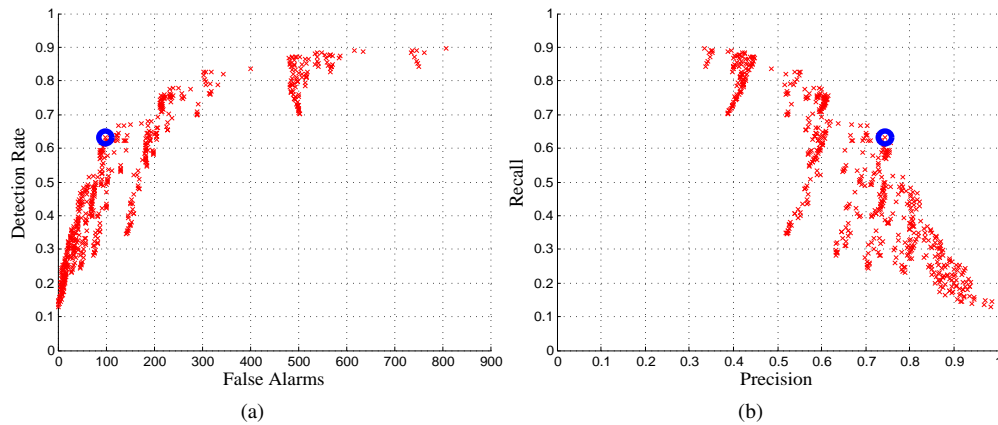


**Figure 4.13:** Detection of bubbles in pulp suspension images: (a) ROC; (b) PRC.

### 4.3.3 CCA performance on oil dispersion images

Performance of the CCA method on oil dispersion images was evaluated using data provided by [13]. Example images are shown in Fig. 4.16. In total, 236 images with the resolution of 319x240, containing 1114 oil drops marked by an expert, were provided. We applied the CCA method on the provided data, and the examples of the detection can be seen in Fig. 4.16. The parameter configuration was the same as in Section 4.3.1, except for the filter size for the oil drops being 10x10, the maximum radius was set to 30, and the segmentation threshold was 0.7.

In [13], Dominguez et al. focused on the detection of the oil drops only. The images also contain other circular objects such as air bubbles, but the provided ground truth contained only the parameters of the oil drops. The CCA method is oriented towards the detection of any kind of circular objects. Therefore, when using the provided ground truth, it was only possible to estimate the True Positive Rate (TPR). Since the main application of our method is volume estimation,

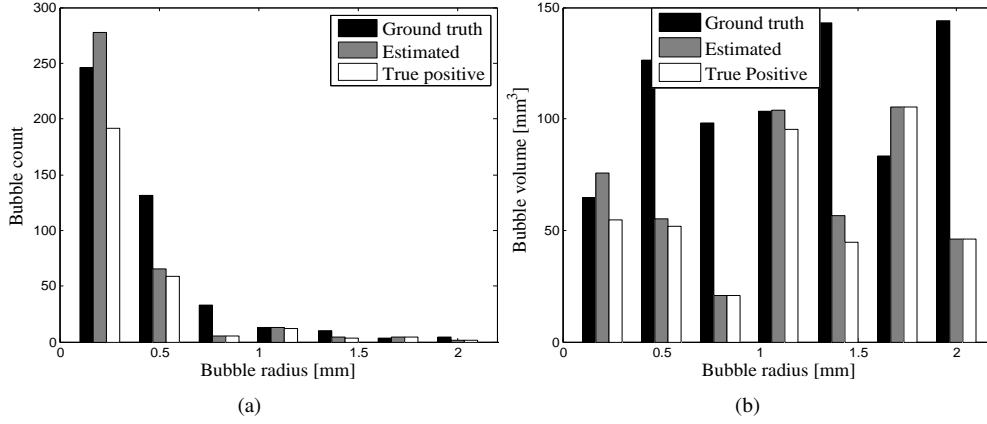


**Figure 4.14:** Detection of bubbles with the sliding window approach: (a) Number of bubbles as a function of a size; (b) Bubble volume as a function of a size.

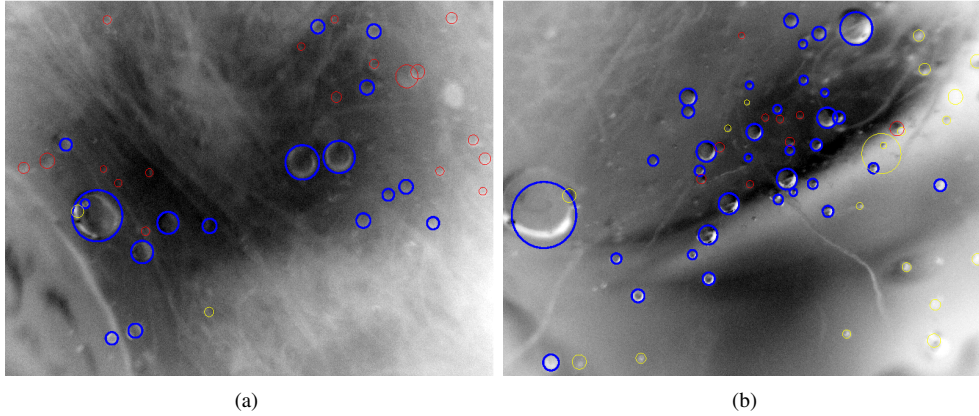


**Figure 4.15:** Detection of bubbles in pulp suspension images: (a) Examples of the original images; (b) Bubble volume as a function of a size.

the accuracy of oil volume estimation in the images is computed. The following results were obtained:

- True Positive Rate (number of oil drops)  $TPR = \frac{TP}{TP+FN} \cdot 100\% = 44\%$ ;
- True Positive Rate (oil volume)  $TPR_v = \frac{TP_v}{TP_v+FN_v} \cdot 100\% = 86\%$ ; and
- Mean relative error of volume estimation  $M = \frac{1}{M} \sum_{i=1}^M \left( \frac{|V_{est_i} - V_{gt_i}|}{V_{gt_i}} \right) \cdot 100\% = 13\%$ .
- The total error of volume estimation  $M_t = \frac{|V_{est} - V_{gt}|}{V_{gt}} \cdot 100\% = 3\%$ .

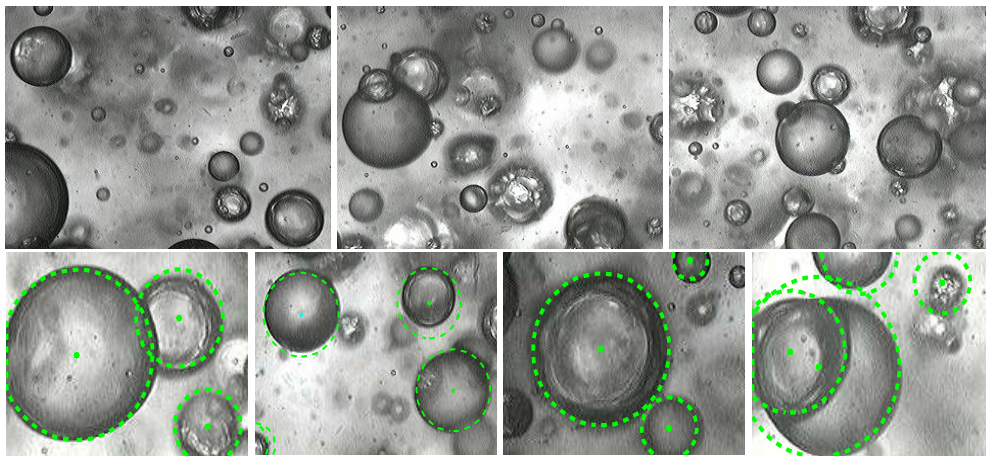


**Figure 4.16:** Examples of oil dispersion images. Detection examples on oil dispersion images.

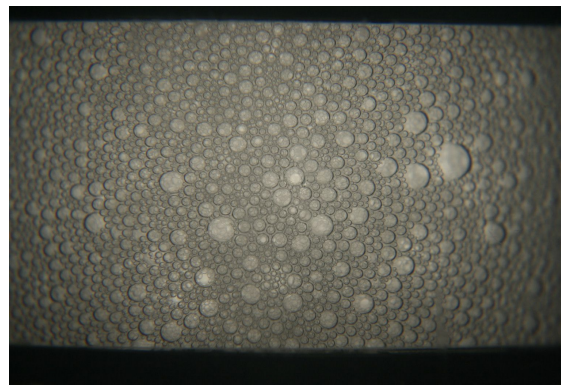
According to the results, the method succeeds in the task of oil volume estimation with a relatively small error of 3%. The low value of the TPR with regard to the number of the detected oil drops can be explained by the problems in detecting the small blob-like circular objects. According to [13], the oil drops manifest themselves as small objects with sharp dark edge.

#### 4.3.4 Wet foam images with dense dispersion

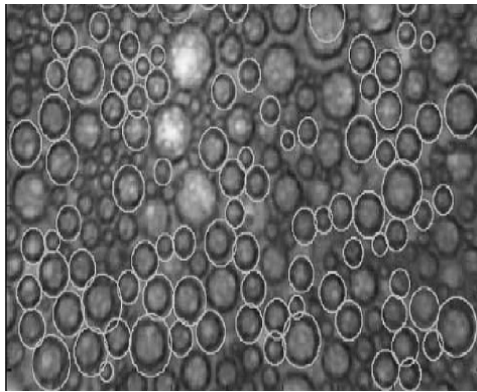
In [105], Zabulis et al. utilize an appearance-based method for the bubble detection in wet foam images with the resolution of 1536x1024. An example image is shown in Fig. 4.17(a) and an example of the adopted bubble template is shown in Fig. 4.3(b). Since the ground truth was not provided by the authors, only visual examples are demonstrated in Fig. 4.17. The example shows that the CCA method can be also applied to the analysis of dense dispersions. The computation time in our experiment was approximately 2 minutes on a PC with a 2.6 GHz CPU, while the reported time in [105] was approximately 15 minutes. However, the authors did not specify the computation platform. It is worth noting that the computational time of the CCA method depends on the number of generated hypothesis, and therefore, in dense dispersion images it was rather high. The parameters of the CCA method were the same as in the gas volume estimation problem (see Section 4.3.1), except that the filter size was 10x10.

## 4.4 Summary

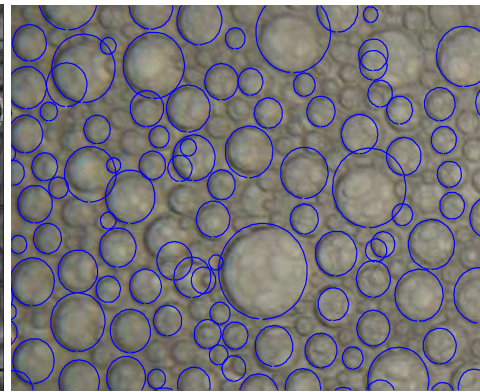
A method for the detection of bubbles, or more generally, transparent spherical objects in a liquid, was presented. The problem was formulated as the detection of Concentric Circular Arrangements (CCA) which are recovered in a hypothesize-optimize-verify framework. The proposed method for bubble detection showed good performance in an application requiring the estimation of the gas volume in pulp suspension, achieving the mean relative error of 19% with the precision of 64%. The method performance was demonstrated also on the images of the wet foam with



(a)



(b)



(c)

**Figure 4.17:** Detection examples on the wet foam images: (a) An example of a wet foam image; (b) Appearance-based method by [105]. The figure is represented with a permission from Elsevier Limited; (c) The CCA method.

dense dispersion and the oil dispersion images. In the future work, more research will be done on the method acceleration and methodology improvement to eliminate the false positives.

### 5.1 Problem statement and previous work

Pulp flow characterization implies the estimation of the flow velocity as well as the detection of anomalies (e.g., turbulence, vortices) in the flow that can signal process malfunctioning. Modeling of the flow can also assist in the development of manufacturing equipment. In-line characterization means that the flow is analyzed directly from the process enabling fast and more efficient process control. In this thesis, given a set of double-exposed images, dense 2D velocity vectors for pulp flow are estimated. The double-exposed images are utilized in the cases when the flow speed is high and it is needed to be captured fast. In Fig. 5.1 examples of the double-exposure images of the pulp suspension captured in a laboratory flow cell are presented.

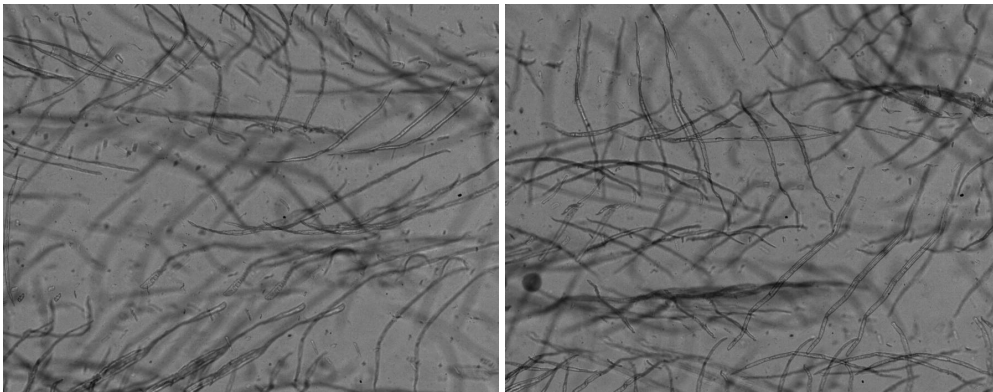


**Figure 5.1:** Example of images captured with a double exposure (provided by CEMIS-OULU).

Particle Image Velocimetry (PIV) is a common optical measurement technique for industrial fluid flow analysis [24]. Acting as indicators of motion, seed particles are added to the flow. Measuring the distance traveled by the particles allows the estimation of flow velocity, turbulence, and other

derived physical properties. The investigated area is typically illuminated by a laser light beam. Images are acquired within a short period of time, and therefore the PIV technique requires very high-intensity illumination [24]. One way is to record an illuminated image for each illumination pulse and to combine two or more illuminated flow images in a single frame, thus, obtaining a multiple exposure image. If the density of the seed particles is low, Particle Tracking Velocimetry (PTV) [47] is utilized where the particles are tracked individually. In this thesis, the role of particles is played by the fibers in the flow. To track individual fibers separately is infeasible since the consistency of the suspension is usually high. The task of the dense velocity vectors estimation is formulated as a task of the fiber displacement computation, which is not straightforward since fibers can change their orientation and appearance.

In order to reduce the background noise in laboratory conditions, particles of bigger size can be utilized, or an optimal angle between the camera and the light source can be found, which allows to decrease reflections from the background [46]. However, in many cases, before the methods for the flow velocity estimation can be applied, additional preprocessing of the acquired images is required. The noise can be smoothed out by median filtering [102], neighborhood average filtering [71], or Gaussian filtering [27].

The methods for flow velocity estimation can be divided into two groups [76]: image patch-based techniques [74] and methods utilizing the principles of optical flow [30], [11]. In the first group of methods, a PIV image is divided into overlapping or non-overlapping patches. For each patch from the current image a corresponding patch from the consecutive images is sought, utilizing the maximum of the cross-correlation. Flow velocity vectors are the vectors going through the centers of the found patches. The main problem of the patch-based methods is that the estimated vector field is often incoherent and unsmooth, which requires post-processing (e.g., median filtering [76]).

The connection between the fluid and optical flows was formally described by Liu and Shen in [60]. The majority of the developed methods, based on the optical flow estimation, were built upon the original Horn and Schunk (HS) method [34], as it is stated in [88]. The flow is modelled as a global energy function over an image. Optimizing this model function, the velocity vectors are found. The methods developed later differ by the modelled objective function, by its approximation, and by the computational method for the objective function optimization. For example, in [108], the optical flow constraint equation is compensated with the fitted higher-order term by matching the corner points extracted by the Harris corner point detector [29]. In [88] Sun et al. studied the state-of-the-art methods and carried out a systematic experiments varying the model and the optimization method. This experiment allowed the authors to conclude that none of the modifications significantly improved over the baseline HS method.

If the estimated velocity field is not smooth, the following post-processing practices, summarized in [88], can be applied: texture decomposition [96], temporal averaging of the derivatives [35], and median filtering [96]. In the case of large scale motions, a coarse-to-fine estimation technique can be applied to give a rough estimate of the large-scale motion and then to improve the result locally [6]. The median filtering improved the performance of all the methods tested in [88]. Alternatively, bilateral filtering [100] can be utilized to avoid smoothing across the motion direction.

In this thesis, the traditional autocorrelation technique [45] is compared to modified Particle Image Pattern (PIP) matching [36]. At first, a large scale motion is estimated by the global autocorrelation technique. Utilizing the results of the global estimate as a baseline, the local autocor-

relation and pattern matching result in a more precise velocity field. A framework utilizing global and local techniques for pulp flow velocity estimation is proposed, where a synthetic image set and a real-world image set were used for testing in [81]. In this work it is assumed that the motion of the pulp flow is planar, which allows to use the correlation-based techniques. Moreover, it is assumed that there are no big local variations in the velocity field vectors.

## 5.2 Pulp flow velocity estimation

### 5.2.1 Estimation of the global displacement

The estimation of the optical flow global displacement allows the measurement of a large-scale motion velocity not taking into account local anomalies. The method of global displacement estimation for double-exposed images is based on autocorrelation [46]. Before the autocorrelation matrix is computed, the background is subtracted, eliminating the background noise. In this work the mean value of all pixel intensities is subtracted from the image intensities.

After the image preprocessing, the correlation matrix is computed as

$$\gamma(\Delta X, \Delta Y) = \frac{\sum_{x,y} [I(x, y) - \bar{I}] [T(x - \Delta X, y - \Delta Y) - \bar{T}]}{\sqrt{\left\{ \sum_{x,y} [I(x, y) - \bar{I}]^2 \sum_{x,y} [T(x - \Delta X, y - \Delta Y) - \bar{T}]^2 \right\}}}, \quad (5.1)$$

where  $I$  is the original image,  $T$  is the same image in the case of autocorrelation or part of the image or template in the case of cross-correlation,  $\bar{T}$  is the mean of the template, and  $\bar{I}$  is the mean of the image  $I$  in the template region,  $\gamma$  is the value of the normalized cross-correlation coefficient of  $I$  and  $T$  with shift  $(\Delta X, \Delta Y)$ , and  $x, y$  are coordinates. The result of computation is a normalized autocorrelation matrix (see example in Fig.5.2). The second local maximum is localized providing the global displacement  $D_g$ . The autocorrelation function always contains a self-correlation peak located at the origin. Two peaks describing the global displacement of the pulp flow image locate symmetrically around the self-correlation peak [74]. Therefore, the direction of the flow, whether the flows moves right or left, cannot be determined.

### 5.2.2 Estimation of the local displacement

The computed global displacement gives a good estimate for the coarse motion in the images, but by nature the optical flow can contain irregularities which should be also detected. In this thesis, local displacement is estimated by the autocorrelation technique [46] and the pattern matching technique [36].

#### AUTOCORRELATION TECHNIQUE

As in the global displacement computation, the background noise is reduced by subtracting the mean intensity from the image. The image is subsequently split into parts, starting with four, and for each part the normalized autocorrelation matrix is computed, the second local maximum of the matrix is found, providing an estimate for the local displacements. The parts of the image are split into subsequent parts until the size of the part is less than the estimated global displacement  $D_g$ . The autocorrelation technique is summarized in Algorithm 6.

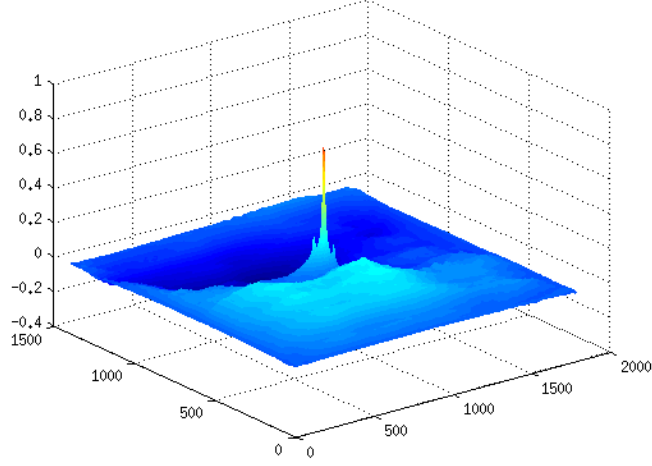


**Figure 5.2:** An example of the autocorrelation matrix.

#### PIP MATCHING TECHNIQUE

The original Particle Image Pattern (PIP) matching for individually exposed images was introduced in [37]. In [36] the PIP matching for the double-exposed images was presented and verified. Given a double-exposed image  $I(x, y)$ , the task is to estimate the flow displacement in the point  $(x_0, y_0)$ , restricted to the maximum displacement  $D_g$ .  $\Delta X$  and  $\Delta Y$  as the  $x$ - and  $y$ - components of the pulp flow shift between two exposures respectively. An interrogation PIP, or IPIP [36], of size  $2N + 1 \times 2N + 1$  equals to

$$\begin{aligned} IPIP(m, n) &= I(x_0 + m, y_0 + n), \\ m, n &= -N, -N + 1, \dots, N. \end{aligned} \quad (5.2)$$

The search PIP, or SPIP [36], of size  $2M + 1 \times 2M + 1$  equals to

$$\begin{aligned} SPIP(m, n) &= I(x_0 + \Delta X + m, y_0 + \Delta Y + n), \\ m, n &= -M, -M + 1, \dots, M. \end{aligned} \quad (5.3)$$

The background noise is compensated by the subtraction of the mean value. The normalized cross-correlation matrix (See Eq. 5.1) is computed for each image part (IPIP) and whole image (SPIP). In Eq. 5.1,  $I$  is SPIP and  $T$  is IPIP. In this thesis, the SPIP is equal to the whole double-exposed image. Therefore, the Eq.5.1 takes the following form

$$\gamma(\Delta X, \Delta Y) = \frac{\sum_{x,y} [SPIP(x, y) - \bar{SPIP}] [IPIP(x - \Delta X, y - \Delta Y) - \bar{IPIP}]}{\sqrt{\left\{ \sum_{x,y} [SPIP(x, y) - \bar{SPIP}]^2 \sum_{x,y} [IPIP(x - \Delta X, y - \Delta Y) - \bar{IPIP}]^2 \right\}}}. \quad (5.4)$$

**Algorithm 6** Autocorrelation method for the local displacement estimation**Input:** a double-exposed grayscale image  $\mathbf{I}$ , an estimate of the global displacement  $D_g$ **Output:** a set of computed local displacements  $D = \{D_i\}$ .

- 1: Compute the mean intensity of the image  $\bar{I} = \frac{1}{n} \sum_{i=1}^n I(x_i, y_i)$ , where  $n$  is the number of pixels in the image.
- 2: Extract the mean intensity from the image pixels  $I_m = I - \bar{I}$ .
- 3: Split the image  $I_m$  into  $n = 4$  parts  $J_1, \dots, J_4$  each of size  $N$ .
- 4: **repeat**
- 5:     **for all**  $J_i$  **do**
- 6:         Compute autocorrelation matrix (Eq.5.1).
- 7:         Compute the local displacement  $D_i$  as the second local maximum.
- 8:         Split the image  $I_m$  into  $n = 4n$  parts  $J_1, \dots, J_n$  each of size  $N$ .
- 9:     **end for**
- 10: **until**  $N \leq D_g$

The second local maximum is sought for each cross-correlation matrix to estimate the displacement. The image is subsequently split into parts and the cross-correlation is computed for each part until the size of the image part is less than the global displacement  $D_g$ . The PIP matching method is summarized in Algorithm 7.

**Algorithm 7** PIP matching method for the local displacement estimation**Input:** a double-exposed grayscale image  $SPIP$ , an estimate of the global displacement  $D_g$ **Output:** a set of computed local displacements  $D = \{D_i\}$ .

- 1: Compute the mean intensity of the image  $S\bar{PIP} = \frac{1}{N} \sum_{i=1}^N I(x_i, y_i)$ , where  $N$  is the number of pixels in the image.
- 2: Extract the mean intensity from the image pixels  $SPIP_m = SPIP - S\bar{PIP}$ .
- 3: Split the image  $SPIP_m$  into  $n = 4$  parts  $IPIP_1, \dots, IPIP_4$  each of size  $N$ .
- 4: **repeat**
- 5:     **for all**  $IPIP_i$  **do**
- 6:         Compute cross-correlation matrices between  $IPIP_i$  and the whole image  $SPIP$  (Eq.5.4).
- 7:         Compute the local displacement  $D_i$  as the second local maximum.
- 8:         Split the image  $SPIP_m$  into  $n = 4n$  parts  $IPIP_1, \dots, IPIP_n$  each of size  $N$ .
- 9:     **end for**
- 10: **until**  $N \leq D_g$

## POSTPROCESSING

In order to restrict the location of the maximum in the cross-correlation matrix and take into account the estimated global displacement, the low-pass Butterworth filter [7] is applied to the cross-correlation matrix. The size of the Butterworth filter is defined by estimated displacement from the previous level of splitting. When the image is split once, it is called the first level of splitting. The global displacement is the zero level of splitting. The radius of the Butterworth filter has to be more than the displacement computed in the previous level. In this case the Butterworth

filter does not remove the peak of the cross-correlation matrix, which corresponds to the local displacement. The Butterworth filter should be applied to the cross-correlation matrix such that the center of the Butterworth filter matches the global maximum value of the cross-correlation matrix.

As the post-processing step the local displacement is compared to the global displacement and if the difference exceeds 10% the value of the local displacement is replaced by the global displacement. Due to the directional ambiguity in the double-exposed image all vectors are redirected to the left-to-right direction.

#### PIP MATCHING VS. AUTOCORRELATION

The signal-to-noise ratio of PIP matching is determined by the number of particles in the IPIP image [36], whereas the signal-to-noise ratio of autocorrelation depends on number of particle pairs within the autocorrelation window. It is the main difference between the PIP matching and autocorrelation. The number of particles within the IPIP is determined by the fiber concentration in the pulp flow and does not depend on the particle displacement in the image [36]. For each particle within the IPIP a pair can be found from the SPIP no matter how large the displacement is. Therefore, PIP matching solves the problem that autocorrelation encounters in the cases of large displacement with a small autocorrelation window. PIP matching has better signal-to-noise ratio than autocorrelation, which decreases with the increasing particle displacement in the image. The bigger signal-to-noise ratio of PIP matching technique allows the local displacement to be estimated more carefully using the smaller size of window.

### 5.3 Synthetic data generation

In order to evaluate the methods the experiments were performed first on the synthetic images which contain known ground truth. The Thin Plate Spline (TPS) is an effective tool for modeling coordinate transformations and it is applied to the set of single exposure images to produce the second exposure [56]. Utilizing the warping technique [99], the second exposure image is produced and combined with the original image. The TPS is a commonly used basis function for representing coordinate mappings from  $\mathbb{R}^2$  to  $\mathbb{R}^2$ . The TPS models deformations by interpolating displacement between the source and target points [56]. For the set of reference points  $P_0 = \{p_i = \{x_i, y_i\} | i = 1, 2, \dots, n\}$  the TPS transformation [15] is defined as

$$f(x, y) = \Phi_s(x, y) + R_s(x, y) = a_1 + a_x x + a_y y + \sum_{i=1}^n \omega_i U(r_i), \quad (5.5)$$

where  $U(r_i) = r_i^2 \log r_i^2$ ,  $r_i = |p_i - (x, y)| = \sqrt{(x_i - x)^2 + (y_i - y)^2}$ . TPS transformation consist of two parts the affine part and the elastic part. The affine part  $\Phi_s(x, y)$  is a sum of polynomials with coefficients  $\mathbf{a} = [a_1 \ a_x \ a_y]$ . A sum of Radial Basis Functions (RBF) with coefficients  $\omega = [\omega_1 \ \omega_2 \ \dots \ \omega_n]$  corresponds to the elastic parts  $R_s(x, y)$ . It is assumed that the locations  $(x_i, y_i)$  are all different and are not collinear. The TPS interpolant  $f(x, y)$  minimizes the bending energy

$$E_{TPS}(f) = \iint \left| \frac{\partial^2 f}{\partial x^2} + \frac{\partial^2 f}{\partial x \partial y} + \frac{\partial^2 f}{\partial y^2} \right|^2 dx dy \quad (5.6)$$

In order to find the coefficients  $(\mathbf{a}, \omega)$  the linear system for the TPS needs to be solved:

$$\begin{cases} \mathbf{K}\omega + \mathbf{P}\mathbf{a} = v \\ \mathbf{P}^T\omega = \mathbf{0} \end{cases} \quad (5.7)$$

where  $\mathbf{K}$  is the  $n \times n$  matrix given by  $K_{ij} = U(r_{ij})$ ,  $f(x_i, y_i) = v_i$ ,  $i = 1, 2, \dots, n$ ,  $\mathbf{P}$  is the  $n \times 3$  matrix and the  $i$ th row of  $\mathbf{P}$  is  $[1 \ x_i \ y_i]$ ,  $\mathbf{0}$  is a  $3 \times 1$  column vector of zeros, and  $v = [v_1 \ \dots \ v_n]$  [15]. After that, the transformation is applied to the reference points  $P_0 = \{(p_i = \{x_i, y_i\} | i = 1, 2, \dots, n)\}$ .

In this work, the reference points are located on a uniform grid. After computing the target image, the synthetic double-exposed image is produced by computing the mean value of the gray levels for each pixel in the target and reference images.

## 5.4 Experiments and discussion

### 5.4.1 Synthetic data

Images of the birch pulp flow produced by the CEMIS-OULU Laboratory were taken as the source images. There were 100 images of 896x704 pixel size taken with 5x magnification and 80 ns exposure. Two datasets of the synthetic images were produced using the method described in Section 5.3. The datasets differed in the way the target point locations were computed. In the first dataset the target points were computed by adding a constant shift value to  $x$ -coordinate of the source points. The second set was generated using polar coordinates, which are more natural in the case of rotation transformation. A shift for the second synthetic dataset had a normal distribution with  $\mu = 80$  and  $\sigma^2 = 10$ . The normal distribution of angle had parameters  $\mu = 0$  and  $\sigma^2 = \pi/32$ . Examples of the original and the synthetic images are presented in Fig. 5.3.

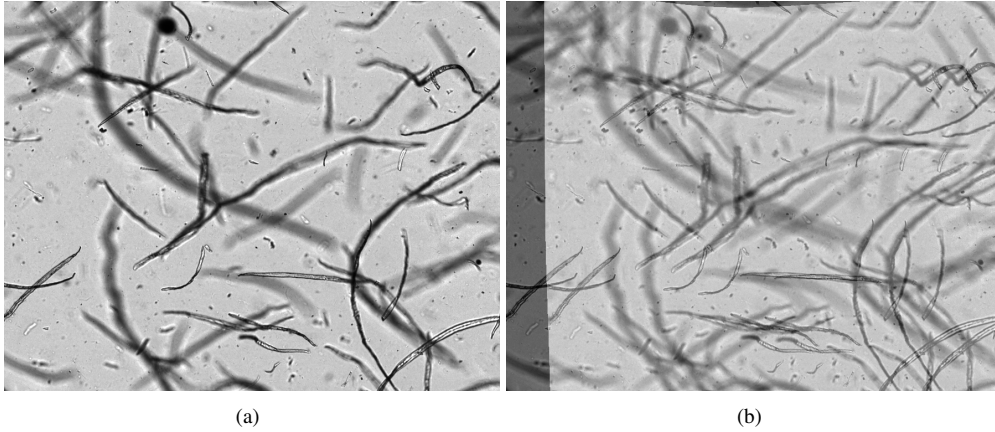


**Figure 5.3:** Synthetic data: (a) An original image with an individual exposure; (b) A synthetic double-exposed image.

The results are presented in Table 5.1, where 8500 displacement vectors were computed for the current dataset. The second column contains the percentage of the correctly computed vectors.

A correctly computed vector is a vector with a relative length error less than 10%.  $\delta\hat{L}$  is a relative error of the computed displacement vectors and  $\Delta\hat{\alpha}$  is an average angle between vectors. The last column contains the execution time of the method per image. The methods were implemented in Matlab and executed on a PC with a 2.6 GHz CPU.

**Table 5.1:** Performance of the methods on the synthetic images.

| The method and the dataset             | Total correct, [%] | $\delta\hat{L}$ , [%] | $\Delta\hat{\alpha}$ | $t$ , [s] |
|--|--------------------|-----------------------|----------------------|-----------|
| Autocorrelation, the 1st synthetic set | 83.3               | 2.9                   | -0.01                | 18        |
| Autocorrelation, the 2st synthetic set | 72.5               | 9.3                   | -0.04                | 17        |
| PIP matching, the 1st synthetic set    | 99.8               | 0.0                   | 0.00                 | 163       |
| PIP matching, the 2st synthetic set    | 80.1               | 4.3                   | 0.00                 | 220       |

Since the displacement in the first set of images was linear, the results of the both methods in the first dataset were better than in the second one. The relative error of the vector length computation for the autocorrelation method reached 2.92%, while the PIP matching produced the correct results in almost all the cases. The second dataset is more similar to the real dataset. The relative errors of the vector length computation for the second dataset are 4.30% for the PIP matching method and 9.32% for the autocorrelation method. On the synthetic datasets the PIP matching outperformed the autocorrelation technique but it required much more time for computation.

#### 5.4.2 Real world test data

There were two datasets of the real data, provided by the CEMIS-OULU Laboratory. The images were captured with a CCD camera QImaging Retiga-2000R. In the first set of images there were 100 images (896x704 pixels) of the birch pulp captured with 5x magnification and 100 us delay between laser pulses. The image in the first datasets had very little distortions in the pulp flow. Images in the second set were taken with different measurement setup. Most of the fibers in the images are blurred. This dataset contains 80 images (400x300 pixels) of eucalyptus pulp, captured with 2.5x magnification and 2 ms delay between the pulses. The ground truth was produced for each image manually by a non-expert. It contained a set of vectors, each corresponding to the displacement of fibers in that area. An example of the ground truth markings is presented in Fig. 5.4(a). Ground truth contains the length and location of the vectors.

The following procedure was utilized to compare the ground truth and the computed vectors. First, the nearest vector of the ground truth for each vector of the computed vector field was sought. After that, the lengths of vectors and angles to the  $x$ -axis were compared. If the difference between them is less than 10% of the absolute value of the length and the angle, it is considered that the vectors are correctly computed. Otherwise, the vector is computed incorrectly. The accuracy of the result is computed as the ratio between the vectors length. The results for the both datasets are presented in Table 5.2, where 8500 displacement vectors were computed. The second column presents the percentage of correctly computed vectors.  $\delta\hat{L}$  is the relative error between the computed vector length and the nearest vector length in the ground truth.  $\Delta\hat{\alpha}$  is the average angle between vectors. The last column in Table 5.2 contains the execution time of the method per image.

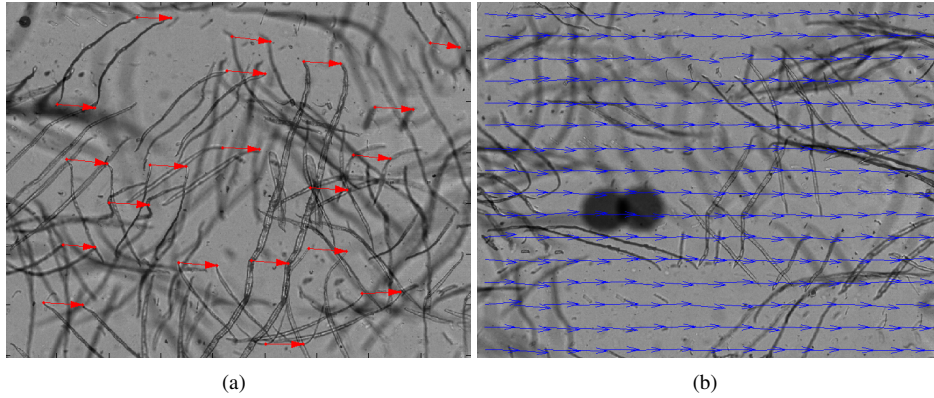


**Figure 5.4:** Real data: (a) An example of the ground truth image; (b) Velocity vectors obtained with the PIP matching.

**Table 5.2:** Performance of the methods on the real images.

| The method and the dataset   | Total correct, [%] | $\delta\hat{L}$ , [%] | $\Delta\hat{\alpha}$ | $t$ , [s] |
|------------------------------|--------------------|-----------------------|----------------------|-----------|
| Autocorrelation, the 1st set | 71.1               | 12.6                  | 0.00                 | 17        |
| Autocorrelation, the 2nd set | 66.2               | 30.1                  | 0.00                 | 3         |
| PIP matching, the 1st set    | 84.2               | 8.3                   | -0.01                | 193       |
| PIP matching, the 2nd set    | 74.1               | 19.7                  | 0.01                 | 10        |

An example of the velocity vector estimation is presented in Fig. 5.4(b). From Table 5.2 it can be seen that the percentage of the correctly computed vectors for both of the developed methods on the first dataset is greater than on the second. In 5% of cases the global displacement was computed incorrectly and caused errors in the local displacement estimation. The PIP matching outperformed the autocorrelation similarly to the experiments on the synthetic data. The accuracy for the PIP matching technique is higher than for the autocorrelation method. However, the autocorrelation required less computational time, since the PIP matching was implemented without optimization.

## 5.5 Summary

Two methods of flow velocity estimation were compared: the PIP matching and the autocorrelation technique. A set of experiments was performed on two synthetic datasets and two real data sets with manually marked ground truth. On the synthetic dataset, the PIP matching demonstrated an accuracy of 91.7% while the accuracy of the autocorrelation technique was 87.4%. On the real images the PIP matching and the autocorrelation methods achieved an accuracy of 80.3% and 69.0% correspondingly. The PIP matching method outperforms the autocorrelation method for estimation of the local displacements for each dataset. However, the autocorrelation requires less computation time than the PIP matching.



---

## Dirt particle detection and classification in dried pulp sheets

### 6.1 Problem statement and previous work

Dirt detection has always been an important part of pulp quality assessment. Several existing automated systems for dirt detection are described in Section 2.4. In this thesis the problem of dirt detection is extended to dirt classification, which, to the knowledge of the author, was not addressed in the literature. The accurate classification of particles would allow to adjust the process automatically to eliminate the impurities, thus enabling savings in chemicals and energy consumption. In a production problem situation, fast and precise information on the type of particles present in the process can reveal the source of the problem, and the process can be adjusted accordingly.

The images of the dried pulp sheets, provided by the pulp and papermaking experts from the FiberLaboratory, included three different types of pulp and four different types of dirt particles. Bleached hardwood, bleached softwood, and softwood pulp after the second chlorine dioxide bleaching stage ( $D_1$ ) were used to produce the pulp sheets. The color of the  $D_1$  pulp is not completely white (see Fig. 6.1) and, thus, more variation for the background was gained. Despite the fact that the number of different pulp and dirt types in this work cannot be considered to represent the full variation of pulp in the industry, the sample set was sufficient to develop the framework.

Four common types of dirt particles were selected based on the literature [28, 12] and expert knowledge: shives, bark, plastic, and sand (see Fig. 6.2). The dirt particles were either prepared or separated from the pulp in the paper laboratory. The shives were separated from reject pulp from brown stock screening. The bark particles were created by disintegrating pine bark mixed with water in a disintegrator. A plastic canister was ground to create excess plastic particles. The natural sand was washed to get rid of extra particles and dust. A small amount of sand was also obtained as reject pulp was washed.

One of the major problems in developing an automated dirt particle classification system is the collection of ground truth data essential for training of a supervised system. To obtain the ground truth, the exact location and type of each dirt particle need to be given. The identification of

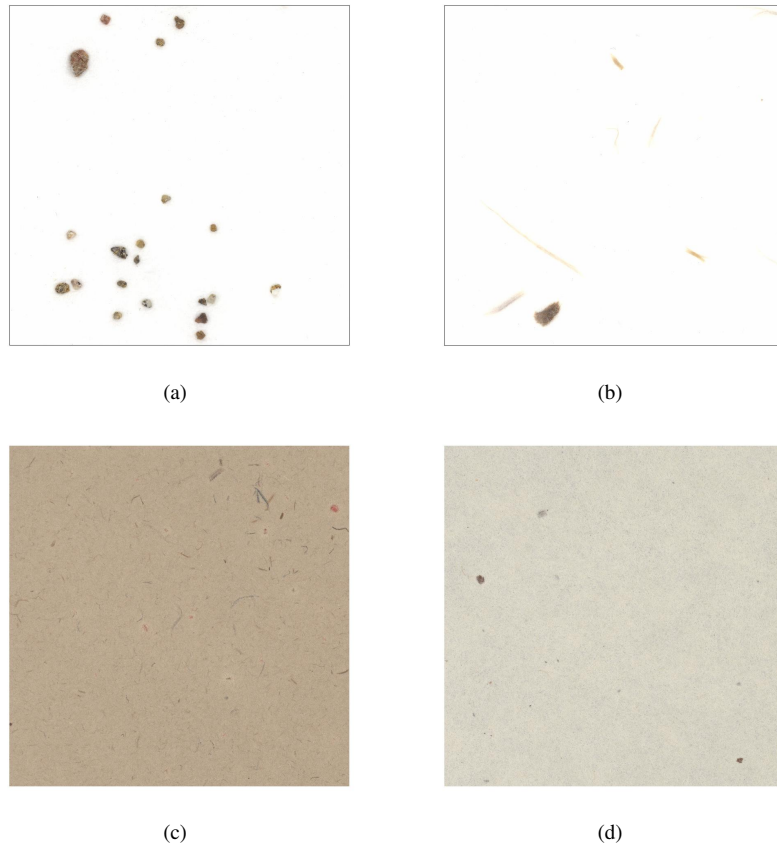


**Figure 6.1:** Pulp sheet images: (a) Bleached pulp with sand; (b) Bleached pulp with shive; (c)  $D_1$  pulp with bark; (d) Stock pulp with plastic.

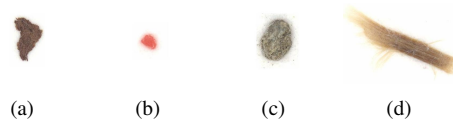


**Figure 6.2:** Clearly different examples of the dirt particles: (a) Bark; (b) Plastic; (c) Sand; (d) Shive.

specific dirt particles can be a very difficult task even for experts, and the large amount of data required makes collecting the ground truth a very laborious and time-consuming process. In some systems, the difficulties with the performance evaluation are mentioned. For example, in [70] there was no opportunity to compare the results with manually segmented particles. In [8] it is also shown that an inspection by humans may be subjective: the number of dirt particles detected by different inspectors was different.

Originally, the solution to ground truth generation using the semisynthetic approach was intro-

duced in [85]. Initial experiments on the dirt classification problem utilizing the proposed framework were presented in [83]. The previous studies were combined and extended to build a full framework for developing dirt particle detection and classification systems in [86]. The framework was designed using the provided laboratory paper sheets, but it can be transferred to the industrial scale. The expertise of the paper laboratory personnel is not used to provide the ground truth manually but for carrying out their most important task: produce dirt and pulp that is as clean as possible. In this thesis a method for generating the ground truth and methods for dirt particle classification are introduced. The framework was tested both with semisynthetically generated images based on real pulp sheets and with independent original real pulp sheets without any generation.

## 6.2 Framework for developing dirt particle classification

### 6.2.1 Workflow description

The basic idea of the proposed framework is illustrated in Fig. 6.3. The initial images with a single dirt type in each are used to produce the semisynthetic images. From each of the images, segmented dirt particles are collected to create a database of dirt particle images which are to be scattered on a generated background. The method to produce the semisynthetic background is discussed in Section 6.3. The actual ground truth is represented by a binary mask, containing the exact location of each particle and its type. After the semisynthetic images are obtained, one can segment and classify dirt, which can be evaluated using the semisynthetic ground truth.

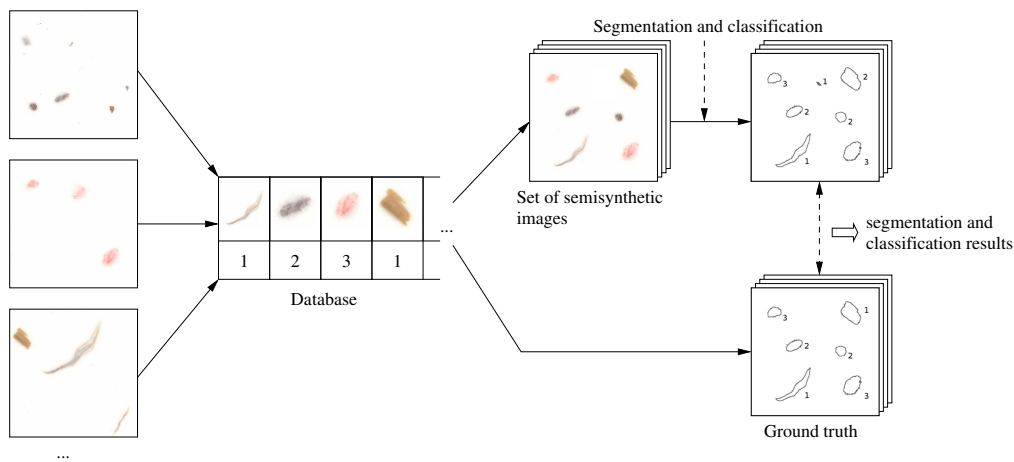


**Figure 6.3:** Framework for dirt particle segmentation and classification.

The semisynthetic images are processed using Algorithm 8, where a set of features is extracted from the segmented particles and the close-to-optimal feature set is determined to be used in further classification.

**Algorithm 8** General workflow for dirt particle segmentation and classification

- 1: Use a segmentation method such as the Kittler thresholding [48] to produce the dirt image segments (Sec. 6.3.1).
- 2: Manually validate the segmented dirt.
- 3: Extract features from the segments (Sec. 6.4).
- 4: Determine a close-to-optimal feature set for classification (Sec. 6.4).
- 5: Train and test of different classifiers (Sec. 6.4.2).
- 6: Evaluate the performance of the classifiers (Sec. 6.5).

### 6.3 Semisynthetic ground truth generation

In any classification system, it is important to have reference data to allow the evaluation of the classification result. As already mentioned, the ground truth can be, in several cases, laborious or even impossible to obtain. Therefore, there is a need to produce the reference data synthetically. Manual dirt annotation can be substituted by the semisynthetic procedure that is described in this section. The semisynthetic ground truth generation consists of the following stages: 1) dirt particle segmentation and database generation, 2) background generation to fill the holes left by the removed dirt particles, and 3) random scattering of the dirt particle images and creation of the corresponding ground truth image.

#### 6.3.1 Segmenting images of sheets with dirt

The first step of semisynthetic ground truth generation is to create a database of dirt particles. To accomplish this, dirt particles are segmented from the initial images. According to the survey [79], there exists a number of methods to segment foreground objects (dirt particles) from the background, but none of them can be universally used for segmentation problems. In this study, the Kittler thresholding method [48] is used. The choice is based on previous experimental studies on detecting small particles from fiber-based surfaces [25, 16]. The selected global thresholding approach is a reasonable choice in the image with a rather homogeneous background.

The segmentation was performed on the grayscale images because the segmentation method is based on the intensities. The separated foreground (dirt) and background are modeled as a mixture of two Gaussians [48]. The threshold is computed optimizing the cost function based on the Bayesian classification rule.

The segmented particle images are used to create the database. Table 6.1 illustrates the database outline. An image with a bounding box for each of the segmented particles is stored in the database, as well as its area and type.

**Table 6.1:** An outline of the dirt particle database.

| Particle 1  | Particles 2   | Particle 3  | ... |
|---|---|---|-----|
|  |  |  | ... |
| Type 1  | Type 2  | Type 3  | ... |

### 6.3.2 Background generation

The segmented dirt is removed from the images so that the area occupied by the dirt particles is substituted by white pixels. These holes in the image are filled with a synthetic background generated by the Markov Random Field (MRF) method [97], which is one of the common approaches for texture synthesis (e.g., in [49]). In the concept of MRFs [107], a random field is composed pixel by pixel. The probability of each pixel to have a certain intensity depends on the intensity or color of its neighboring pixels. A sample background image without any dirt particles is selected from one of the original images. This sample image is used as the ideal background for area filling. In Algorithm 9, the probability is not calculated explicitly to reduce the computational load. The number of iterations can be restricted, for example, by a threshold dependent on the standard deviation of color which should be close to the original background.

---

**Algorithm 9** Background generation

---

- 1: Construct the neighborhood of each pixel in the sample image.
  - 2: Repeat steps 3-5 until a satisfactory result defined by the threshold is obtained.
  - 3: Construct the neighborhood of the current pixel from the original image,
  - 4: Find the best matching neighborhood from the sample image,
  - 5: Substitute the current pixel by the pixel with the best matching neighborhood.
- 

There are several factors to consider in this algorithm: 1) how to determine the neighborhood, 2) how many iterations should be carried out, and 3) what the best matching neighborhood is. In the implemented version of the algorithm, the neighborhood is determined by the user, as well as the number of iterations. The best match is found by computing the distance between two neighborhoods and choosing the one with the shortest Euclidean distance.

### 6.3.3 Inclusion of dirt particles

After the dirt database has been created and the holes left by the removed dirt particles are filled, the dirt particles can be placed on the background images to create semisynthetic images. At this stage, a specified number of dirt particles is spread over the uniform synthesized background. According to [106], the particles should be placed randomly, and the implementation allows a random rotation of the particles. To prevent dirt particle overlaps, a binary mask is used to store the information on occupied areas in the image. In Algorithm 10, the place for a new particle is selected from the unoccupied area.

---

**Algorithm 10** Dirt particle placing

---

- 1: Initialize a binary mask to zeros.
  - 2: Repeat steps 3-6 to reach the desired amount of dirt particles.
  - 3: Randomly select a dirt particle from those that have not been placed yet,
  - 4: Find the place for the particle in the binary mask not occupied by any other particle,
  - 5: Place the dirt particle on the background,
  - 6: Update the binary mask.
- 

The amount of dirt in an image is controlled by the percentage of dirt covering the surface. To form the list of dirt particles to be positioned on the image, the user specifies what type of dirt is needed to be added onto the image and its proportion.

As a result, Algorithm 10 produces an image with a uniform background and dirt particles placed on it randomly. The information about the dirt particles is stored in the form of a labeled binary mask that represents the ground truth.

In some cases it might be useful to consider normalization of the colors [85] (e.g., when combining pulp sheets of different types). In this study, color normalization was not used.

## 6.4 Dirt features and their use in classification

The data used in this study cannot be considered to represent the full variation of pulp nor all characteristics of dirt types. To make the system stable when a new type of dirt is introduced or to adapt the system for completely new dirt types, a tool is required to tune the classification process. This calls for feature evaluation, which aims at estimating the feature importance and makes it possible to determine the set of features that describe the available data in the most efficient way.

### 6.4.1 Feature extraction and evaluation

The dirt features computed in this work are divided into two categories: geometric features and color features. The geometric features include characteristics related to the shape, form, and uniformity of dirt particles. To complement them, the color features include, for example, mean color, variation of color, and intensity. The features are presented in Table 6.2.

**Table 6.2:** The feature set. The equation numbers refer to the text.

|                  |              |         |
|------------------|--------------|---------|
| Maximum diameter | Extent       |         |
| Minimum diameter | Length       | Eq. 6.1 |
| Solidity         | Width        | Eq. 6.2 |
| Eccentricity     | Form factor  | Eq. 6.3 |
| Convex area      | Roundness    | Eq. 6.4 |
| Perimeter        | Aspect ratio | Eq. 6.5 |
| Std of color     | Elongation   | Eq. 6.6 |
| Mean intensity   | Curl         | Eq. 6.7 |
| Mean color       | Coarseness   | Eq. 6.8 |
| Area             |              |         |

For each dirt particle, a bounding box is determined, which is the smallest rectangle enclosing the dirt particle. The solidity specifies the proportion of the pixels in the convex hull that belong to the region. Eccentricity specifies the eccentricity of the ellipse that contains the same second-moments as the region. The convex area is the number of pixels in the convex hull of a dirt particle. The extent specifies the ratio of pixels in the region to pixels in the total bounding box. The mean color and mean intensity are calculated as the mean hue value and the mean intensity over a dirt particle area. Std of color describes the standard deviation of color within the area of a dirt particle. The other geometric features are calculated according to the following formulas:

$$Length = 0.25 \cdot (Perimeter - (\sqrt{|Perimeter^2 - 16 \cdot Area|})), \quad (6.1)$$

$$Width = \frac{Area}{Length}, \quad (6.2)$$

$$FormFactor = \frac{4 \cdot \pi \cdot Area}{Perimeter^2}, \quad (6.3)$$

$$Roundness = \frac{4 \cdot Area}{\pi \cdot MaxDiameter^2}, \quad (6.4)$$

$$AspectRatio = \frac{MaxDiameter}{MinDiameter}, \quad (6.5)$$

$$Elongation = \left| \frac{Length}{Width} \right|, \quad (6.6)$$

$$Curl = \left| \frac{MaxDiameter}{Length} \right|, \quad (6.7)$$

$$Coarseness = \frac{Perimeter^2}{4 \cdot \pi \cdot Area}. \quad (6.8)$$

In order to determine the feature set to be used in classification, a feature evaluation procedure is used. An exhaustive search (i.e. evaluating all the possible combinations of features) would be computationally infeasible. Therefore, the sequential feature selection [65] procedure is used instead. At each step, the method adds (forward selection) or removes (backward selection) a new feature to the feature set and calculates an objective function value to be minimized. Since the method only moves in one direction, adding or deleting features, it eventually evaluates only a subset of all possible feature combinations. Therefore, the optimal feature set cannot be guaranteed but rather a close-to-optimal feature set is produced. In this work, the sequential feature selection was applied using the forward selection and the linear discriminative function [18]

$$g(\mathbf{x}) = \mathbf{w}^t \mathbf{x} + w_0 \quad (6.9)$$

was selected. In Eq. 6.9 the weights  $\mathbf{w}$  in the linear combination of the features  $\mathbf{x}$  are optimized to minimize the linear discriminative function, taking into account the bias  $w_0$ . This provides the information how well the combinations of features can be distinguished.

#### 6.4.2 Classification methods

The classifiers used in the study are listed in Table 6.3. State-of-the-art generic classification methods, as well as the well-known structural approaches, are used to avoid being related to specific data. The K-NN classifier is used with neighborhoods of one, three, and five samples. The goal of the Linear Discriminant Analysis (LDA) is to maximize the separability of data classes, defining the transform to the space where the current features might be distinguishable in the most efficient way. The Gaussian Mixture Model (GMM) classifier is used with expectation maximization (GMMem) and Figueiredo-Jain (GMMfj) criteria [22]. With the Figueiredo-Jain criterion, the maximum number of 20 components was set and as a result each class was modeled with the most appropriate number of components, the maximum number being seven. For this reason, in the expectation maximization approach, seven components were used to model the data. The Support Vector Machine (SVM) was used with the radial basis function kernel.

**Table 6.3:** The list of used classifiers.

|  |      |
|--|------|
| K-Nearest Neighborhood (K-NN)                          | [92] |
| Support Vector Machine (SVM)                           | [18] |
| Naive Bayesian Classifier (Bayes)                      | [92] |
| Bayesian Classifier using Gaussian Mixture Model (GMM) | [18] |
| Linear Discriminant Analysis (LDA)                     | [26] |

## 6.5 Experiments and discussion

### 6.5.1 Data and performance evaluation

Sample sheets of the three different pulp types, introduced in Fig. 6.1, were prepared by the FiberLaboratory according to the ISO 5269-1 standard [39]. The amount of pulp equivalent to 1.63 g of dry pulp and an adequate amount of a single type of dirt particles were mixed before the sheet forming. Consequently, the prepared sample sheets contained an amount of fibers equivalent to a standard 60 g/m<sup>2</sup> sample sheet and an adequate amount of dirt particles. The amount of dirt particles was controlled so that there would be more than 20 particles per sample sheet, but not too many in order to avoid significant overlapping of the particles. All of the three pulp types were mixed with one of the four types of dirt particles, one at a time. Five sample sheets per test point and also one sample containing sand separated from industrial pulp were prepared. As a result, the sample set consisted of 61 sample sheets.

To image the samples, the pulp sheets were scanned with a professional Microtek ArtixScan 2500f scanner with 1250 dpi (A4) resolution, true 42 bit RGB colors, and under reflected light. According to the ISO 5350-1:2006 standard [38], the minimum size of particles that are to be detected is 0.04 mm<sup>2</sup>. The physical resolution was around 0.0004 mm<sup>2</sup> per pixel, which means that the smallest dirt particle occupies approximately 100 pixels.

To evaluate the performance of the proposed framework the following experiments were carried out: 1) the evaluation of the quality of the semisynthetic images, 2) the estimation of the performance of the classification approaches, 3) the analysis of how the semisynthetic data affects the segmentation and classification results, and 4) segmentation and classification of dirt particles in the real pulp sheets based on the semisynthetic training data. All of the experiments were carried out using the data presented in Section 6.1.

### 6.5.2 The semisynthetic data and the statistical evaluation of the generated background

Fig. 6.4 demonstrates the steps of the semisynthetic background generation. The dirt particles are removed from the target image and the holes are filled according to the procedure presented in Section 6.3.2. Fig. 6.5 demonstrates the examples of the generated semisynthetic images. The semisynthetic images contain dirt particles of a predetermined amount, which is set by the user. It defines what percent of the total image area the dirt occupies. The ground truth is stored as a mask with labeled components, where the dirt particles of the same type have the same label. Fig. 6.5(b) and (d) represent different types of dirt by different intensity values in the mask images.

In order to evaluate the quality of the generated background, the F-test was performed to compare the variances of the generated and original parts of the background. The null hypothesis, that

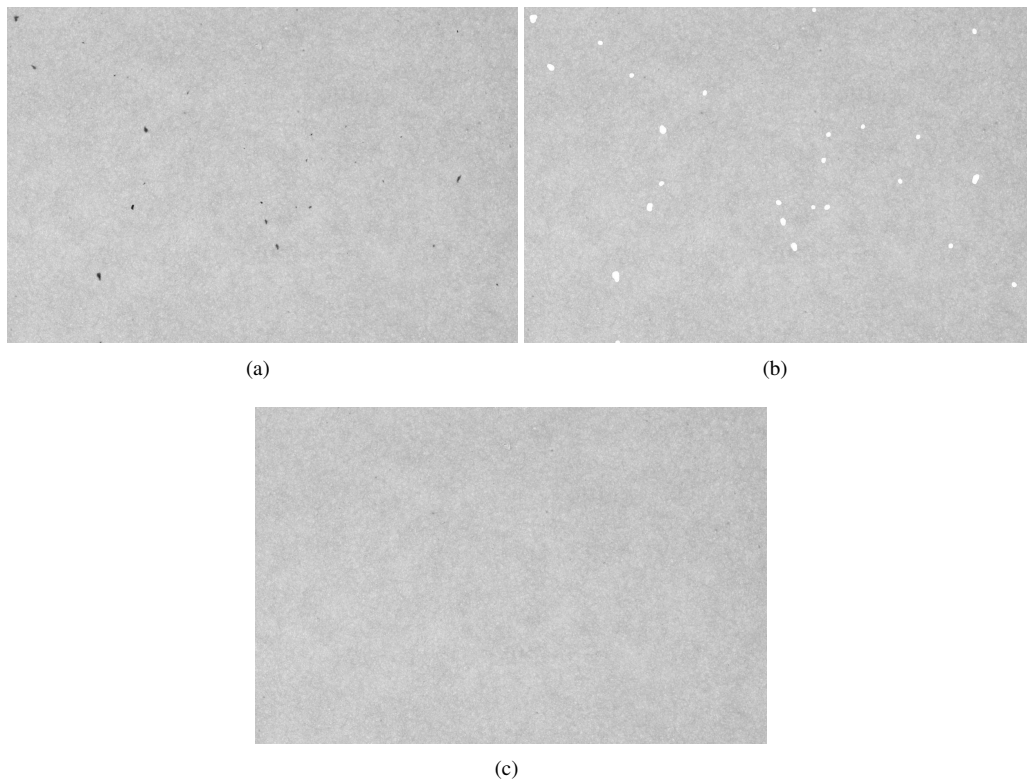


**Figure 6.4:** Background generation: (a) Initial target image; (b) Target image with removed dirt segments; (c) Semisynthetic background image.

the generated and original background have the same variance, could not be rejected at the 2% significance level, which means that the difference between the variances of the generated and original parts of the background is statistically insignificant.

### 6.5.3 The effect of the semisynthetic procedure on segmentation

The semisynthetic procedure has an influence on the background intensity values as the particles are rotated and shifted, and therefore, it is important to know how the semisynthetic procedure affects segmentation. In the classification, on the other hand, only the segmented dirt particles are involved. Therefore, the classification is not significantly affected by the semisynthetic data generation. For the 12 original images, three per each dirt class, the corresponding semisynthetic images were generated so that the dirt from one image remains only in that image, and no other dirt particles were used. In other words, the semisynthetic images contained only those dirt particles which were located in the corresponding original ones, but the particles were moved and rotated according to the semisynthetic procedure. Subsequently, the dirt particles were detected and counted in both the original and generated images. The number of detected particles in the semisynthetic images was compared to the number of particles detected in the original ones, and the results are presented in Table 6.4. The table shows that the results differ insignificantly for

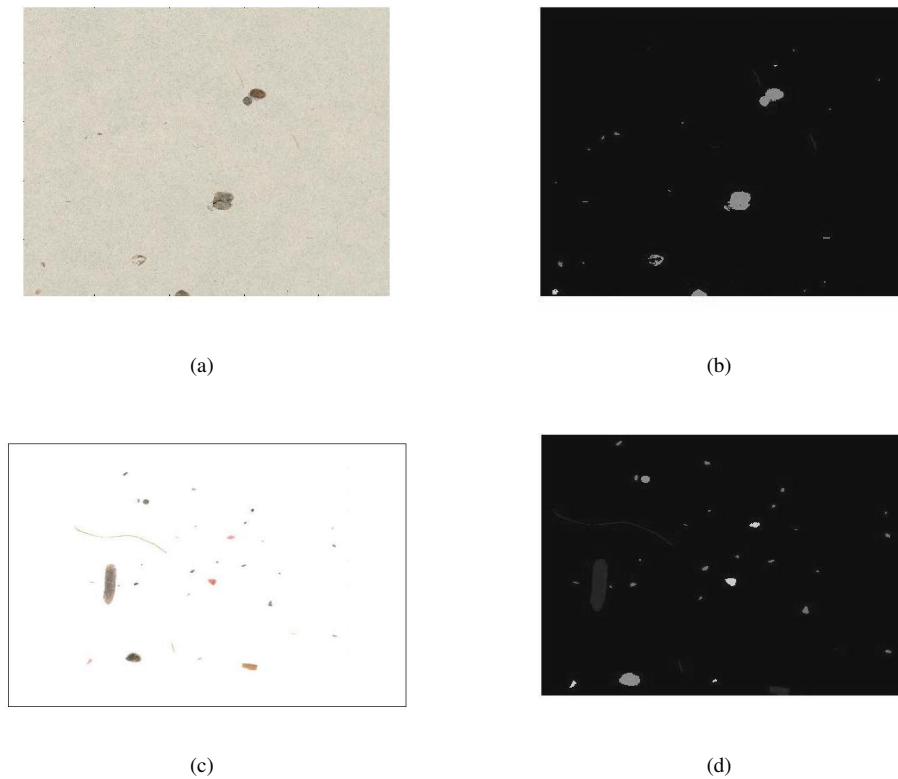


**Figure 6.5:** Example images: (a) Semisynthetic image with the unbleached pulp background; (b) Ground truth mask for the unbleached pulp image; (c) Semisynthetic images with the bleached pulp background; (d) Ground truth masks for the bleached pulp image.

the semisynthetic and original images. However, the reason for the different dirt counts is that, in some cases, the dirt particles are placed too close to each other and they are detected as a single particle. Since the background contains the synthetic parts, it can be a reason for losing some of the particles. One can also notice that for the larger particles (e.g., shives or sand) the difference in the counts is lower.

Additionally, the experiments were performed to compare the total area of the segmented particles in pixels, and Table 6.4 presents the results. One can see that not only are the counts of dirt different in the semisynthetic images, but also the area of the image segments as well as the geometric features. This means that either the features of some particles are modified, some particles can be lost or the wrong particles may be included in the class. This also shows that greater losses occur in the cases of smaller particles, such as plastic and bark.

#### 6.5.4 Dirt classification and the effect of the semisynthetic procedure on classification

The experiments were performed on the softwood pulp after the second chlorine dioxide bleaching stage  $D_1$  pulp. The number of the dirt particles per each class is presented in Table 6.5.

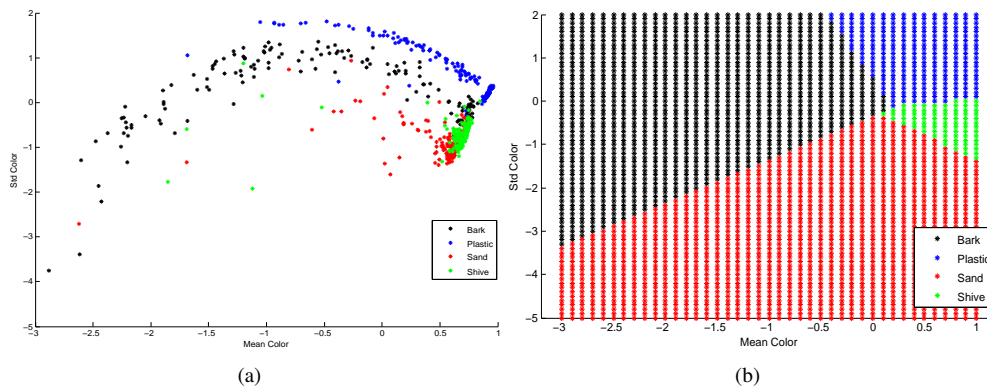
**Table 6.4:** Dirt counts and area for original and generated images.

| Image                          | Bark  | Plastic | Shive  | Sand   |
|--------------------------------|-------|---------|--------|--------|
| Original (Count)               | 445   | 387     | 309    | 213    |
| Semisynthetic (Count)          | 421   | 377     | 310    | 219    |
| Original (Area in pixels)      | 83830 | 89312   | 127611 | 384700 |
| Semisynthetic (Area in pixels) | 75293 | 75515   | 117324 | 376780 |
| Area computation error (%)     | 10.2% | 15.5%   | 6.2%   | 2.7%   |

**Table 6.5:** Number of particles for each dirt type.

|              | Bark | Plastic | Sand | Shive |
|--------------|------|---------|------|-------|
| Training set | 100  | 100     | 100  | 100   |
| Test set     | 751  | 158     | 138  | 66    |

For the sake of visualization, the size of the feature set was restricted to two features. In this case, the set of features includes "MeanColor" and "StdColor", which are illustrated in Fig. 6.6(a). The features were selected using the sequential search with a linear evaluation function.

**Figure 6.6:** Feature analysis: (a) A close-to-optimal feature set; (b) Data boundaries represented by the LDA analysis.

The results of the classification are presented in Fig. 6.7, including the performance of the classification methods on the training and test sets with separate results for different classes. For the 1NN classifier, the classification on the training set is trivial and therefore it is not shown. Fig. 6.8 demonstrates how the data was modeled by the GMM classifier with the Figueiredo-Jain criterion.

As expected, the classification methods, which model the data, give results better than the K-NN classification. For example, it can be seen from Fig. 6.6 that the boundaries between the classes are non-linear, whereas the LDA method models them as strict lines as shown in Fig. 6.6(b). On the other hand, SVM with the radial basis function kernel outperforms all other classification methods in almost all cases.

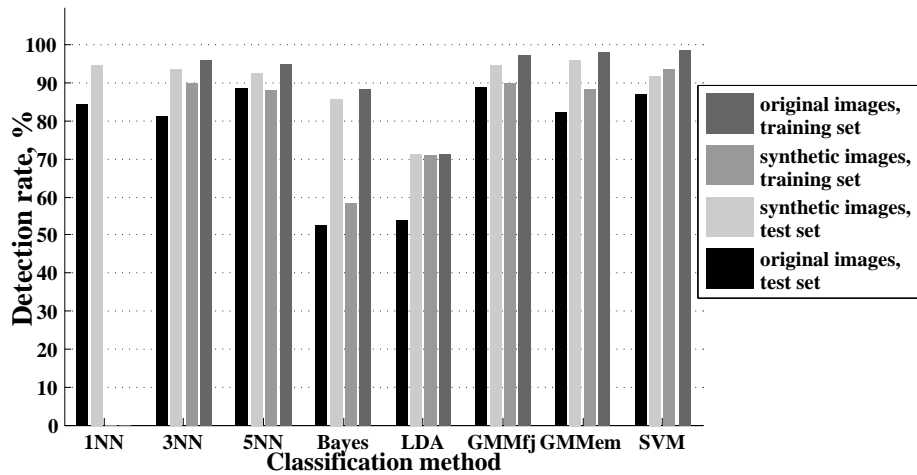


Figure 6.7: Classification results.

Fig. 6.7 presents the classification results on the dirt particles extracted from the original images. The same features were employed as in the experiment with the semisynthetic data. It can be seen that using the semisynthetic procedure impairs the performance, yet allowing to obtain satisfactory results.

### 6.5.5 Method performance introducing an unknown dirt type

Feature evaluation plays an important role when new type of dirt appears in the production. The close-to-optimal feature set, used in the classification, should be updated according to the dirt type that appears. To demonstrate how the classification results change if the feature set is not updated each time the new dirt type appears, the experiments were performed according to Algorithm 11.

---

#### Algorithm 11 Feature selection experiment procedure

---

- 1: Select the close-to-optimal feature set for the classification of two types of dirt.
  - 2: Repeat steps 3-7 until all the types of dirt participate in the classification.
  - 3: Add another type of dirt.
  - 4: Perform the classification of the new set of dirt types using the previously selected features.
  - 5: Select the close-to-optimal feature set for the new set of dirt.
  - 6: Perform the classification of the new set of dirt types using the new feature set.
  - 7: Compare the results of the classification using the previous and the new close-to-optimal feature sets.
- 

For each set of dirt types, the classification results of the close-to-optimal feature set and previous close-to-optimal feature set are compared. The amounts of dirt particles in the training and test set are presented in Table 6.6. The results of feature evaluation and selection can be found in Table 6.7, which shows how the close-to-optimal feature set changes after the new dirt appears or disappears.

Fig. 6.6 presents the detection rates in the situation when the new class appears. The percentage

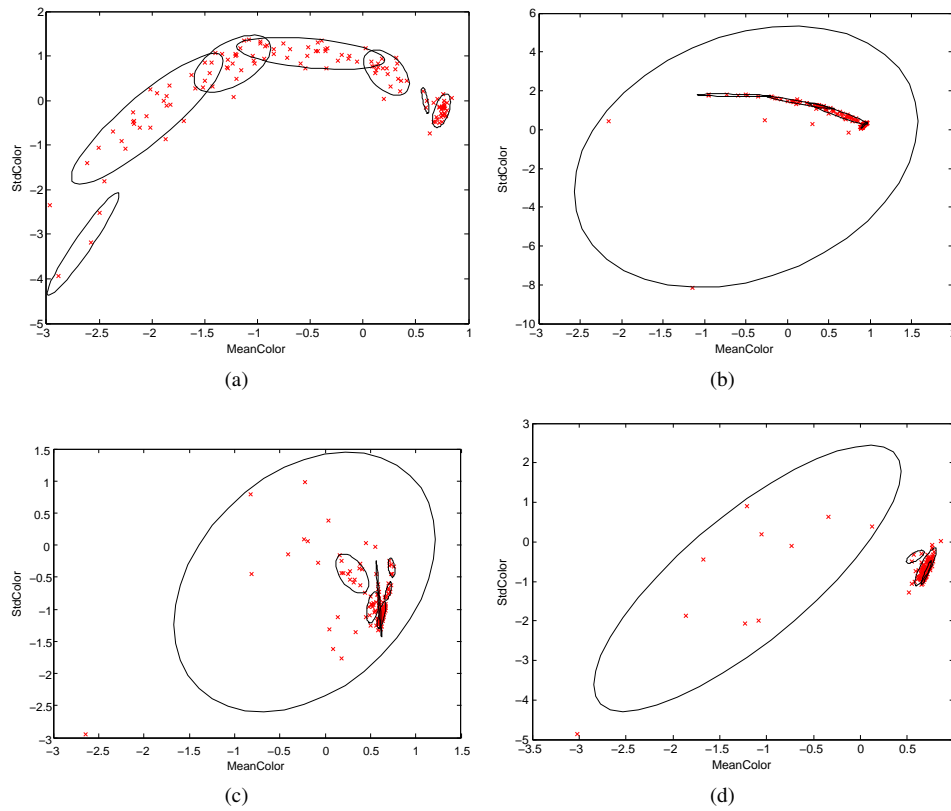


**Figure 6.8:** Classes modeled with the GMM classifier with the Figueiredo-Jain criterion: (a) Bark; (b) Plastic; (c) Sand; (d) Shive.

**Table 6.6:** Amount of particles for each dirt type.

|              | Bark | Plastic | Sand | Shive |
|--------------|------|---------|------|-------|
| Training set | 100  | 100     | 100  | 100   |
| Test set     | 969  | 244     | 233  | 201   |

of correctly classified dirt particles is higher, when the close-to-optimal feature set is used than when the feature sets are not updated.

### 6.5.6 Segmentation and classification of dirt particles in the real pulp sheets based on the semisynthetic training data

The proposed approach was tested with real independent images of dried non-bleached pulp sheets with dirt particles, marked by an expert. "Real" in this context means that the images contain the dirt particles from the real process, but not manually selected or synthetically generated. The set consists of eight images. Examples of the images are presented in Fig. 6.10.

Table 6.7: The selected features.

| Dirt types to be classified      | Close-to-optimal feature set                              |
|----------------------------------|---|
| Bark vs Plastic                  | Coarseness  |
| Bark vs Sand                     | Coarseness  |
| Bark vs Shive                    | Extent, FormFactor, MeanColor                             |
| Plastic vs Sand                  | ConvexArea, Coarseness                                    |
| Plastic vs Shive                 | MaxDiameter, MeanColor, StdColor                          |
| Sand vs Shive                    | AspectRatio, Curl   |
| Bark vs Plastic vs Sand          | MaxDiameter, MeanIntensity, Coarseness                    |
| Plastic vs Sand vs Shive         | MaxDiameter, MeanColor, StdColor                          |
| Bark vs Sand vs Shive            | Coarseness, MeanColor, StdColor                           |
| Bark vs Plastic vs Shive         | Coarseness, MeanColor, StdColor                           |
| Bark vs Plastic vs Shive vs Sand | MaxDiameter, MeanColor, StdColor, Coarseness, AspectRatio |

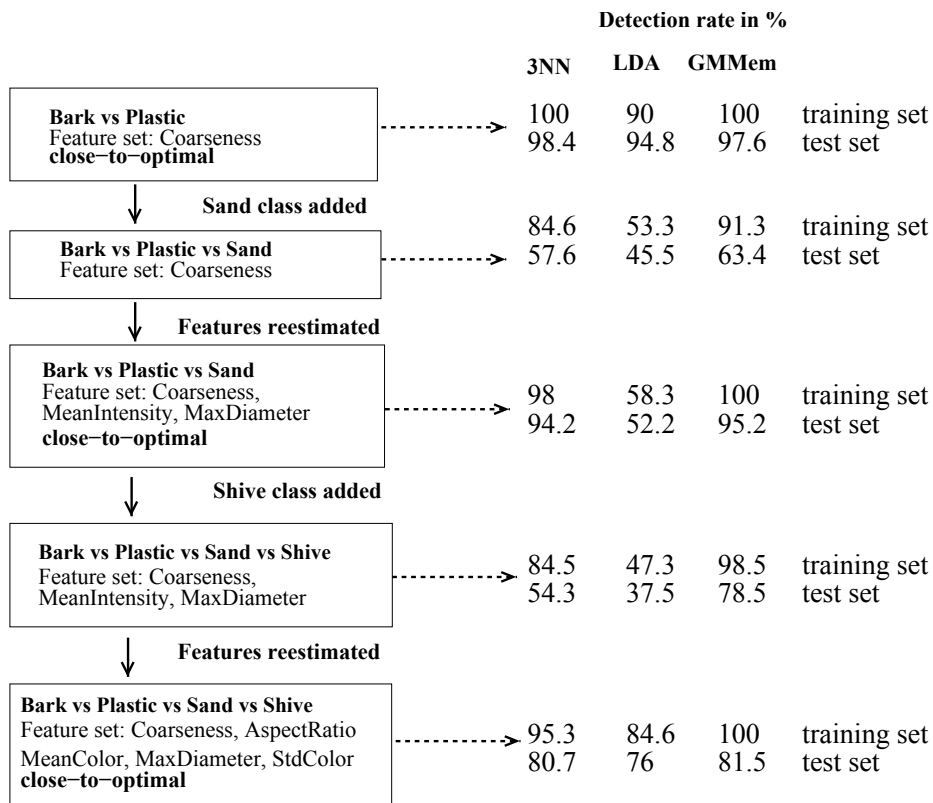
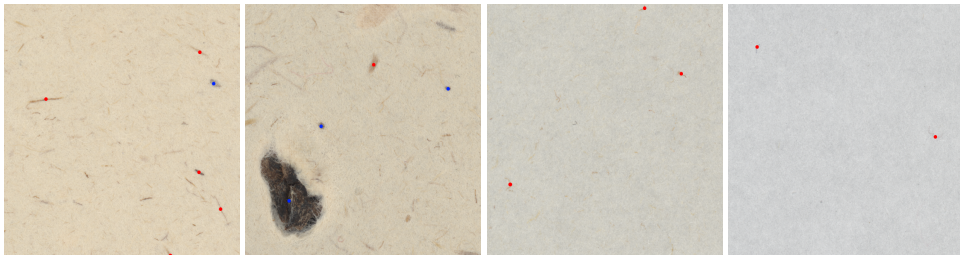


Figure 6.9: Classification results when the new classes appear.

The expert marked only those dirt particles which he was fully confident to be a dirt particle. From the presented images it can be seen that there are other dirt particles in the sheets that were not



**Figure 6.10:** Examples of the pulp sheets with real dirt particles. Bark particles are marked with blue. Shives are marked with red.

annotated by the expert since the expert was less confident about them. The total number of the marked particles was 69, including 57 shives and 12 bark particles. The system was trained on the semisynthetic particles of bark and shives. Each training set of a class consisted of 150 particles. The set of features for classification consisted of "MeanColor" and "Roundness". The classification of the marked particles was performed with 82% accuracy. Lower accuracy compared to the experiments with semisynthetic images can be explained by different imaging conditions causing different appearance of the dirt particles and mistakes made by the expert. It should be also noted that the segmentation method provides a larger amount of the detected particles. This happened since the expert could not decide about the class of each single particle in an image and marked only those about which he was fully confident.

## 6.6 Summary

In this chapter a framework for adaptive dirt detection and classification is proposed. The use of the framework begins with the problem of the ground truth generation and finishes with the analysis of the performance of the standard classification methods. Using the presented procedure for ground truth generation, there is no need for the manual annotation of the particles. The results proved that the semisynthetic procedure does not significantly affect the classification and segmentation results.

In order to make the system adaptable to the changes in dirt particle types, there is a feature evaluation stage where the most important features are determined. The experiments showed that the classification results improve significantly if the close-to-optimal feature set is used in the classification. The experimental part of the work presented the classification results for state-of-the-art and standard classifiers. It was shown that the methods modeling the data, such as GMM and SVM, outperformed other standard methods, such as k-NN.



## **7.1 Methods and results**

The objective of this thesis was to develop vision-based methods for raw material characterization in the pulping process. The material analysis would enable the quality assessment of the raw material and subsequently, the end-product as well as the process control. Analyzing images from the process, vision-based methods provide an efficient tool for on-line and in-line measurements. The work in this thesis was performed to develop methods for pulp analysis, thus assisting quality assessment and process control in pulping. Within the scope of the thesis, four practical tasks were addressed: fiber characterization, gas volume estimation at the bleaching stage, pulp flow velocity estimation, and dirt particle classification in dried pulp sheets. For each of the practical tasks, the research questions stated in the Introduction were answered: what is the origin of ground truth, what machine vision methods are developed to solve the task, and what are the limitations of the developed methods based on the data used in the thesis.

The characterization of fibers in pulp suspension provides information that enables operators to predict the pulp type and the quality of the end product. There are existing commercial solutions for fiber characterization but they are not appropriate for in-line measurements, where the consistency of fibers and the flow speed are high. In the scope of this thesis, a method to measure fiber length and curl index in the pulp suspension images was developed. The microscopic images from the pulp suspension were provided by CEMIS-OULU. The method developed for fiber detection is based on the tensor voting framework that allows a continuity condition on the points belonging to the curvilinear objects to be imposed. Having only one parameter, voting scale, the tensor voting detects the salient points in the images, providing information about the end points and the intersection points. Utilizing those three sets of points (salient points, intersections, and end points), the linking algorithm proposed in this thesis reveals the fibers as connected components. In the conducted experiments, 62% of fibers were detected correctly. The rest of fibers was detected in multiple pieces, at maximum four. The precision of the detection was 80.8%. Fiber length and curl index were estimated with accuracy of 71.5% and 70.7% correspondingly. This accuracy was influenced by the fact that the fibers were detected in multiple pieces. Since the linking algorithm is based on heuristic rules, intersecting fibers were, in some cases, sepa-

rated incorrectly which led to incorrect curl index estimation. It is worth to mention that the fiber consistency in the images used was lower than it is usually at the pulp mill. Therefore, additional testing and possible method development is required when the method is transferred to the industrial scale. However, a positive side of the method developed is that the information about the fiber intersections are revealed which is useful in analysis of the connected fiber network.

At the delignification stage a decisive factor in terminating the process is the gas volume contained in the process. To the author's knowledge until recently it was not possible to capture images from this part of the process. For this thesis, the FiberLaboratory provided images from the pilot unit simulating the process in laboratory conditions. The results obtained with the developed machine vision method help the specialists to learn about the process phenomena and develop the imaging set up. The gas volume was estimated from the bubbles in the images of pulp suspension. The bubbles were detected as Concentric Circular Arrangements (CCA) in the hypothesize-optimize-verify framework. The proposed method demonstrated good performance on the pulp suspension images with the mean relative error of volume estimation 19% and precision 64%. The CCA model, proposed in the thesis, was developed to detect the bubbles that manifest themselves as a set ridge edges. Small blob-like bubbles in many cases were not captured by the proposed method. In the experiments it was demonstrated that these bubbles do not have a significant impact on the total volume estimation. However, they cause an error in the volume distribution estimation. The proposed method for bubble detection was compared to the Circular Hough Transform and the sliding window approaches and demonstrated a better performance. Additionally, experiments were performed on two other sets of bubbles images to demonstrate the method performance on other types of data.

An important part of process control is pulp flow characterization. Irregularities in the flow can signal process malfunction or can affect the formation of the paper web. In this thesis, a dense velocity field was computed from double-exposed images. A global autocorrelation method was applied to get an estimate of a large-scale motion that was later used as a baseline for local estimates. In order to capture the local variations in flow, two methods were compared: autocorrelation-based technique and Particle Image Pattern (PIP) matching. The methods were tested on the synthetic images as well as on the real world data provided by CEMIS-OULU. The PIP matching demonstrated the better accuracy on the two real datasets of 84.2% and 74.1%. It, however, required higher computation time than the autocorrelation method.

Dirt particle detection from the dried pulp sheets has been studied earlier and a number of commercial solutions have been developed. However, a task of dirt classification was not addressed. Classification of dirt particles provides not only the information on the presence of dirt in the product but also assists in finding the source of the problem. In this thesis the framework for dirt particle classification was presented. Attention is paid to the ground truth generation that in many cases, as in the dirt particle classification, is a very laborious task. A method for semisynthetic ground truth generation was proposed that provided images of the pulp sheets with dirt of a known type. To make the dirt classification adaptable to situations when an unknown type of dirt appears, the framework includes a feature selection procedure to reveal the features of dirt particles that allow the best classification results. The performances of the state-of-the-art generic classification methods were compared. In the experiments, it was demonstrated that the synthetic generation of the ground truth insignificantly affects the detection and classification results. The performance of the classifiers was compared on the semisynthetic and real world images with the best classification rate on the real world images of 82%. The significance of the feature selection procedure was also demonstrated in the experiments. The classifiers were tested on the originally

provided images, semisynthetic images, and real independent images. The dried pulp sheets used in this work were prepared with the basis weight of  $60 \text{ g/m}^2$ . With such basis weight all the dirt particles are on the surface of the pulp sheet which allows to create a reliable ground truth and concentrate on dirt classification. At the industrial scale the basis weight can be higher which would cause the problem for the method developed since some particles would be submerged into the pulp and would not be even detected. However, after the ground truth is created and the method is trained in laboratory conditions it would be possible to test it in industrial conditions.

## 7.2 Future work

The developed methods demonstrated good performance in solving the research tasks formulated in this thesis. However, the following propositions can be considered as future work in the four main directions.

### 7.2.1 Fiber characterization

In order to improve the method performance after the heuristic local linking approach proposed in this thesis, a post-processing step, such as fiber verification, can be utilized. A natural continuation of the research in fiber characterization is further development of the method so that it enables pulp type classification. This might, however, require a deeper study of fiber properties and computation of the selected properties. Similar to the dirt classification, a framework for fiber classification can be built, including feature evaluation and classification steps. The classification of the pulp suspension would allow more advanced prediction of end-product quality and properties.

The images used in this thesis were obtained in laboratory conditions. It would be useful to verify the method on different imaging setups and in different conditions. This would allow researchers to check the generalizability of the method on other types of data. As the experiments demonstrated, the problems in fiber detection and especially separation were caused by the linking procedure, which is main direction in the future work.

Transfer of the method to the industrial scale can offer new challenges to the method developed. The consistency of fibers is higher than in the laboratory environment and analysis of fiber network can be another task for automated methods.

### 7.2.2 Gas volume estimation

The imaging setup for the delignification stage of the pulping process is still in the process of development. The new data will be provided to test the CCA approach for bubble detection which will require possible improvement. For example, in order to achieve a better precision of the detection and get rid of the false positives, a hypothesis verification step can be applied. Despite the fact that the method gives a good estimate of the volume, detection of small blob-like bubbles is a weakness and should be addressed in the future. The CCA model is intended to model the bubble structure with multiple ridge edges but it contains a number of parameters, the effect of which should be studied.

### 7.2.3 Pulp flow characterization

The obtained results demonstrated that double-exposed images can be utilized for pulp flow velocity estimation with the methods that were compared: PIP matching and autocorrelation. However, in this work it was assumed that the motion of pulp is planar and there are no big local variations in the velocity field vector. In the future, systematic testing should be performed on the real images with turbulence, which will lead to the possible methods development. It will be interesting to compare the patch-based methods to the optical flow methods utilizing the laws of fluid dynamics.

### 7.2.4 Dirt particle classification

In dirt particle classification, it would be worthwhile to test the method in real world conditions in the industrial process. The method for the ground truth generation can be considered for use in other applications which require tedious manual annotation and where it is difficult for an expert to make a decision (e.g., in bubble annotation). It can be further developed by utilizing color normalization to combine different types of pulp and make the method more flexible (e.g., it would be possible to scale the particles or to allow overlapping). Similarly, particle segmentation should be developed to detect overlapping particles.

The purpose of the thesis was to develop methods suitable for pulp suspension analysis at different stages of the process. The four main tasks were addressed in this scope: fiber characterization, gas volume estimation, pulp flow characterization, and dirt particle classification. The research performed in these four directions resulted in the following contributions:

1. A method for detecting fibers as curvilinear structures in the pulp suspension images. The method is based on the tensor voting framework with the formalized linking procedure proposed in this thesis. The method was tested on the laboratory images for which an average fiber width and curl index were computed. The method has a potential to be extended to more general curvilinear structures.
2. A method for detecting bubbles as concentric circular arrangements that was tested on the pulp suspension images to estimate the volume of gas at the bleaching stage. The proposed method was additionally tested on the two independent sets of images and the results of the bubble detection methods on the pulp suspension images were compared to the results of the Hough transform and template matching.
3. A comparison of the two methods for pulp flow velocity estimation, both of which demonstrated good results in the problem solving task.
4. In the task of dirt particle classification in dried pulp sheets:
  - (a) a method for a semisynthetic ground truth generation;
  - (b) a framework for dirt particle classification in the dried pulp sheets that includes the procedure of the close to optimal feature set selection that is important when a new dirt type appear. The performance of generic state-of-the-art classifiers was compared on the semisynthetic and real images.

The developed methods provide tools to build an integrated system for process control and product analysis at the industrial level.

- [1] Electromagnetic flowmeters from KROHNE. [online]. Available: <http://krohne.com/en/products/flow-measurement/electromagnetic-flowmeters/>. Accessed 2013-10-01.
- [2] On-line air content analyser sonica [online]. Available: <http://forest.savcor.com/solutions/sonica>. Accessed 2013-10-01.
- [3] The verity IA color image analysis software [online]. Available: <http://www.verityia.com/dirt-counter.php>. Accessed 2010-09-15.
- [4] ATHERTON, T., AND KERBYSON, D. Size invariant circle detection. *Image and Vision Computing* 17, 11 (1999), 795–803.
- [5] BARTL, A., AND PICO, D. Characterization of short fibers. In *Proceedings of the 9th International Conference on Chemical and Process Engineering, ICheaP-9*. (Rome, Italy, May 2009).
- [6] BRUHN, A., WEICKERT, J., AND SCHNÖRR, C. Lucas/kanade meets horn/schunck: Combining local and global optic flow methods. *International Journal of Computer Vision* 61 (2005), 211–231.
- [7] BUTTERWORTH, S. Theory of filter amplifiers. *Experimental wireless and the wireless engineer* 7 (1930), 536–541.
- [8] CAMPOY, P., CANAVAL, J., AND PENA, D. Inspulp: An on-line visual inspection system for the pulp industry. *Computers in Industry* 56 (2005), 935–942.
- [9] CANNY, J. A computational approach to edge detection. *IEEE Transactions on Pattern Analysis and Machine Intelligence*, 8, 6 (1986), 679–698.
- [10] CHENG, Y., AND LIU, Y.-S. Polling an image for circles by random lines. *IEEE Transactions on Pattern Analysis and Machine Intelligence* 25, 1 (2003), 126–131.
- [11] CORPETTI, T., HEITZ, D., ARROYO, G., MÉMIN, E., AND SANTA CRUZ, A. Fluid experimental flow estimation based on an optical-flow scheme. *Experimental Fluids* 40, 1 (2006), 80–97.
- [12] DENCE, C. W., AND REEVE, D. W., Eds. *Pulp Bleaching, Principles and Practice*. TAPPI Journal, 1996.

- [13] DOMINGUEZ, R. A., AND CORKIDI, G. Automated recognition of oil drops in images of multiphase dispersions via gradient direction pattern. In *Proceedings of the 4th International Congress on Image and Signal Processing, CISP* (Shanghai, China., October 2011), vol. 3, pp. 1209–1213.
- [14] DON, G., SUTHERLAND., N., AND RANTANEN, W. Comparison of fiber length analyzers. In *Proceedings of the TAPPI Practical Papermaking Conference* (Milwaukee, Wisconsin. Atlanta, GA, USA, May 2005).
- [15] DONATO, G., AND BELONGIE, S. Approximate thin plate spline mappings. In *Proceedings of the 7th European Conference on Computer Vision-Part III, ECCV* (London, United Kingdom, 2002), Springer-Verlag, pp. 21–31.
- [16] DROBCHENKO, A., KAMARAINEN, J.-K., LENSU, L., VARTAINEN, J., KÄLVIÄINEN, H., AND EEROLA, T. Thresholding-based detection of fine and sparse details. *Frontiers of Electrical and Electronic Engineering in China* 6, 2 (2011), 328–338.
- [17] DUDA, R., AND HART, P. Using the hough transform to detect lines and curves in pictures. *Communications of the ACM* (1972), 11–15.
- [18] DUDA, R., HART, P., AND STORK, D. *Pattern Classification*. Wiley, 2001.
- [19] DURAK, N., AND NASRAOUI, O. Extracting salient contour groups from cluttered solar images via markov random fields. In *Proceedings of the 18th IEEE International Conference on Image Processing, ICIP* (Brussels, Belgium, September 2011), pp. 2825–2828.
- [20] FARDIM, P., Ed. *Chemical Pulping Part 1, Fiber Chemistry and Technology*. Paperi ja Puu Oy, 2011.
- [21] FASTENAU, H., HAGEDORN, J., AND JOUSIMAA, T. Automatic dirt counting during the production of market pulp. *TAPPI JOURNAL* 74, 6 (1991), 73–78.
- [22] FIGUEIREDO, M., AND JAIN, A. Unsupervised learning of finite mixture models. *IEEE Transactions on Pattern Analysis and Machine Intelligence* 24, 3 (2002), 381–396.
- [23] FISCHLER, M. A., AND BOLLES, R. C. Random sample consensus: A paradigm for model fitting with applications to image analysis and automated cartography. *Communications of the ACM* 24, 6 (1981), 381–395.
- [24] FOCK, H., AND RASMUSON, A. Computation of fluid and Particle Motion From a Time-Sequenced Image Pair: A Global Outlier Identification Approach. *Nordic Pulp & Paper Research Journal* 23, 1 (2008), 120–125.
- [25] FOULADGARAN, M., MANKKI, A., LENSU, L., KÄYHKÖ, J., AND KÄLVIÄINEN, H. Automated counting and characterization of dirt particles in pulp. In *Proceedings of the International Conference on Computer Vision and Graphics, ICCVG* (Warsaw, Poland, 2010), pp. 166–174.
- [26] FUKUNAGA, K. *Introduction to Statistical Pattern Recognition*. Academic Press, 1990.
- [27] GONZALEZ, R. C., AND WOODS, R. E. *Digital image processing*. Prentice Hall, 2001.

- [28] GULLICHSEN, J., AND LEVLIN, J. *Chemical Pulping. Papermaking Science and technology*. Fapet Oy, 1999.
- [29] HARRIS, C., AND STEPHENS, M. A combined corner and edge detector. In *Proceedings of the Fourth Alvey Vision Conference* (1988), pp. 147–151.
- [30] HEITZ, D., HÉAS, P., MÉMIN, E., AND CARLIER, J. Dynamic consistent correlation-variational approach for robust optical flow estimation. *Experimental Fluids* 45, 4 (2008), 595–608.
- [31] HIRN, U., AND BAUER, W. A review of image analysis based methods to evaluate fiber properties. *Lenzinger Berichte* 86 (2006), 96–105.
- [32] HONKANEN, M. *Direct Optical Measurement of Fluid Dynamics and Dispersed Phase Morphology in Multiphase Flows*. PhD thesis, Tampere University of Technology, 2006.
- [33] HOOVER, A., KOUZNETSOVA, V., AND GOLDBAUM, M. Locating blood vessels in retinal images by piecewise threshold probing of a matched filter response. *IEEE Transactions on Medical Imaging* 19, 3 (2000), 203–210.
- [34] HORN, B., AND SCHUNCK, B. Determining optical flow. *Artificial Intelligence* 17 (1981), 185–203.
- [35] HORN, B. K. *Robot Vision*, 1st ed. McGraw-Hill Higher Education, 1986.
- [36] HUANG, H. An extension of digital PIV-processing to double-exposed images. *Experiments in Fluids* 24 (1998), 364–372.
- [37] HUANG, H. T., FIEDLER, H. E., AND WANG, J. J. Limitation and improvement of PIV. *Experiments in Fluids* 15 (1993), 168–174.
- [38] INTERNATIONAL ORGANIZATION FOR STANDARDIZATION. Pulps – estimation of dirt and shives – part 1: Inspection of laboratory sheets by transmitted light. ISO 5350-1:2006.
- [39] INTERNATIONAL ORGANIZATION FOR STANDARDIZATION. Pulps – preparation of laboratory sheets for physical testing – part 1: Conventional sheet-former method. ISO 5269-1:2005.
- [40] ISLEK, A., PARSHEH, M., AND YODA, M. The impact of turbulence and swirl on the flow in the tube bank part of a paper mill headbox. In *Proceedings of the TAPPI Spring Technical and International Environmental Conference* (Atlanta, USA, March 2004), pp. 417–428.
- [41] JANG, J.-H., AND HONG, K.-S. Detection of curvilinear structures and reconstruction of their regions in gray-scale images. *Pattern Recognition* 35, 4 (2002), 807–824.
- [42] JUNTUNEN, P., TORNBERG, J., AND AILISTO, H. Automated analysis of coloured ink particles in recycled pulp by machine vision. *Paperi ja Puu* 81, 5 (1999), 375–378.
- [43] JURÁNEK, R., HRADIŠ, M., AND ZEMČÍK, P. *Real-time Algorithms of Object Detection using Classifiers*. InTech - Open Access Publisher, 2012, pp. 1–22.
- [44] KÄLVIÄINEN, H., HIRVONEN, P., XU, L., AND OJA, E. Probabilistic and non-probabilistic hough transforms: overview and comparisons. *Image and Vision Computing* 13, 4 (1995), 239–252.

- [45] KEANE, R. D., AND ADRIAN, R. J. Optimization of particle image velocimeters. Part I: Double pulsed systems. *Measurement Science and Technology* 1, 11 (1990), 1202–1215.
- [46] KEANE, R. D., AND ADRIAN, R. J. Theory of cross-correlation analysis of PIV images. *Applied Scientific Research* 49 (1992), 191–215.
- [47] KHALIGHI, B., AND LEE, Y. H. Particle tracking velocimetry: an automatic image processing algorithm. *Applied Optics* 28, 20 (1989), 4328–4332.
- [48] KITTLER, J., AND ILLINGWORTH, J. On threshold selection using clustering criteria. *IEEE Transactions on System, Man, and Cybernetics* 12 (1985), 652–655.
- [49] KOMODAKIS, N., AND TZIRITAS, G. Image completion using efficient belief propagation via priority scheduling and dynamic pruning. *IEEE Transactions on Image Processing*, 16, 11 (2007), 2649–2661.
- [50] KURAKINA, T. Characterization of fiber and vessel elements in pulp suspension images. Master's thesis, Lappeenranta University of Technology, 2012.
- [51] LAAKSONEN, L. Image processing methods for particle analysis in pulp making process. Master's thesis, Lappeenranta University of Technology, 2010.
- [52] LAAKSONEN, L., STROKINA, N., EEROLA, T., LENSU, L., AND KÄLVIÄINEN, H. Improving particle segmentation from process images with wiener filtering. In *Proceedings of the 17th Scandinavian Conference on Image Analysis, SCIA* (Ystad, Sweden, May 2011), pp. 285–294.
- [53] LEAVERS, V. Which Hough Transform? *Graphical Models and Image Processing: Image Understanding* 58, 2 (1993), 250–264.
- [54] LEIVISKÄ, K. *Process and Maintenance Management*. Fapet Oy, 2009.
- [55] LEVLIN, J.-E., AND SÖDERHJELM, L. *Pulp and Paper Testing. Papermaking Science and technology*. Fapet Oy, 1999.
- [56] LI, J., YANG, X., AND YU, J. Compact support Thin Plate Spline algorithm. *Journal of Electronics (China)* 24, 4 (2007), 515–522.
- [57] LI, T., WELDON, M., AND ODBERG, L. Pipe flow behaviour of hardwood pulp suspension studied by NMRI. *Journal of Pulp and Paper Science* 21 (1995), 408–414.
- [58] LINDBERG, T. Edge detection and ridge detection with automatic scale selection. In *Proceedings of the IEEE Computer Society Conference on Computer Vision and Pattern Recognition, CVPR* (San Francisco, CA, USA, June 1996), pp. 465–470.
- [59] LINDBERG, T. Edge detection and ridge detection with automatic scale selection. *International Journal of Computer Vision* 30 (1998), 117–154.
- [60] LIU, T., AND SHEN, L. Fluid flow and optical flow. *Journal of Fluid Mechanics* 614 (2008), 253–291.
- [61] LÖNNBERG, B. *Mechanical Pulping*. Fapet Oy, 2009.

- [62] MEDIONI, G., AND KANG, S. *Emerging Topics in Computer Vision*. Prentice Hall, 2004.
- [63] MEDIONI, G., LEE, M., AND TANG, C. *A computational framework for segmentation and grouping*. Elsevier, 2000.
- [64] MING, Y., LI, H., AND HE, X. Connected contours: A new contour completion model that respects the closure effect. In *Proceedings of the IEEE Conference on Computer Vision and Pattern Recognition, CVPR* (Providence, Rhode Island, June 2012), pp. 829–836.
- [65] MOLINA, L., BELANCHE, L., AND NEBOT, A. Feature selection algorithms: A survey and experimental evaluation. In *Proceedings of the 2002 IEEE International Conference on Data Mining* (Washington, DC, USA, 2002), pp. 306–325.
- [66] MORDOHAJ, P., AND MEDIONI, G. Junction inference and classification for figure completion using tensor voting. In *Proceedings of the Computer Vision and Pattern Recognition Workshop, CVPRW* (Washington, DC, USA, June 2004), pp. 56–65.
- [67] OJALA, T., PIETIKÄINEN, M., AND MÄENPÄÄ, T. Multiresolution gray-scale and rotation invariant texture classification with local binary patterns. *IEEE Transactions on Pattern Analysis and Machine Intelligence* 24, 7 (2002), 971–987.
- [68] PAN, L., CHU, W.-S., SARAGIH, J., DE LA TORRE, F., AND X., M. Fast and robust circular object detection with probabilistic pairwise voting. *IEEE Signal Processing Letters*. 18, 11 (2011), 639–642.
- [69] PAPARI, G., AND PETKOV, N. Edge and line oriented contour detection: State of the art. *Image and Vision Computing* 29 (2011), 79–103.
- [70] PARKER, S., AND CHAN, J. R. Dirt counting in pulp: An approach using image analysis methods. In *Proceedings of the IASTED International Conference on Signal and Image Processing, SIP* (Kauai, HI, USA, 2002).
- [71] PENG, L. The analysis of typical method of digital image noise processing. *Journal of Lanzhou Polytechnic College* 11, 2 (2004), 23–26.
- [72] PRESS, W., FLANNERY, B., TEUKOLSKY, S., AND VETTERLING, W. *Numerical Recipes in C: The Art of Scientific Computing*. Cambridge University Press, 1992.
- [73] PROWLAGE. Knowpulp [online]. Available: <http://www.knowpulp.com/english/index.htm>. Accessed 2012-08-02.
- [74] RAFFEL, M., WILLERT, S., WERELEY, S., AND KOMPENHANS, J. *Particle Image Velocimetry: A Practical Guide*. New York: Springer-Verlag, 2007.
- [75] RANDIHA, K., AND BENES, R. Circle detection in pulsative medical video sequence. In *Proceedings of the 10th International Conference on Signal Processing*. (Beijing, China, October 2010), pp. 674–677.
- [76] RAY, N. Computation of fluid and particle motion from a time-sequenced image pair: A global outlier identification approach. *IEEE Transactions on Image Processing* 20, 10 (2011), 2925–2936.

- [77] RONNEBERGER, O., WANG, Q., AND BURKHARDT, H. Fast and robust segmentation of spherical particles in volumetric data sets from brightfield microscopy. In *Proceedings of the 5th IEEE International Symposium on Biomedical Imaging: From Nano to Macro, ISBI*. (Paris, France, May 2008), pp. 372–375.
- [78] ROSENBERGER, R. Using a spread sheet model to develop and evaluate thresholding setting techniques for digitized image dirt counting systems. *Progress in Paper Recycling* (1995), 39–54.
- [79] SEZGIN, M., AND SANKUR, B. Survey over image thresholding techniques and quantitative performance evaluation. *Journal of Electronic Imaging* 13(1) (2004), 146–165.
- [80] ŠOCHMAN, J., AND MATAS, J. Waldboost - learning for time constrained sequential detection. In *Proceedings of the Conference on Computer Vision and Pattern Recognition, CVPR* (Los Alamitos, USA, June 2005), vol. 2, pp. 150–157.
- [81] SOROKIN, M. Image-based characterization of the process flows in pulping. Master’s thesis, Lappeenranta University of Technology, 2012.
- [82] STENIUS, P., Ed. *Forest Product Chemistry*. Fapet Oy, 2000.
- [83] STROKINA, N., EEROLA, T., LENSU, L., AND KÄLVIÄINEN, H. Adaptive classification of dirt particles in papermaking process. In *Proceedings of the 17th Scandinavian Conference on Image Analysis, SCIA*. (Ystad, Sweden, May 2011), pp. 731–741.
- [84] STROKINA, N., KURAKINA, T., EEROLA, T., LENSU, L., AND KÄLVIÄINEN, H. Detection of curvilinear structures by tensor voting applied to fiber characterization. In *Proceedings of the 18th Scandinavian Conference on Image Analysis, SCIA* (Espoo, Finland, June 2013), pp. 22–33.
- [85] STROKINA, N., MANKKI, A., EEROLA, T., LENSU, L., KÄYHKÖ, J., AND KÄLVIÄINEN, H. Semisynthetic ground truth for dirt particle counting and classification methods. In *Proceedings of the 12th IAPR Conference on Machine Vision Applications, MVA* (Nara, Japan, June 2011), pp. 215–218.
- [86] STROKINA, N., MANKKI, A., EEROLA, T., LENSU, L., KÄYHKÖ, J., AND KÄLVIÄINEN, H. Framework for developing image-based dirt particle classifiers for dry pulp sheets. *Machine Vision and Applications* (2013), 1–13.
- [87] STROKINA, N., MATAS, J., EEROLA, T., LENSU, L., AND KÄLVIÄINEN, H. Detection of bubbles as concentric circular arrangements. In *Proceedings of the 21st International Conference on Pattern Recognition, ICPR* (Tsukuba, Japan, November 2012), pp. 2655–2659.
- [88] SUN, D., ROTH, S., AND BLACK, M. Secrets of optical flow estimation and their principles. 2432–2439.
- [89] SUTMAN, F. J. Sampling statistics applied to automated tappi dirt counting. *TAPPI Journal*, 77, 5 (1994), 179–182.
- [90] SUTTON, P., JOSS, C., AND CROSSELY, B. Factors affecting fiber characteristics in pulp. In *Proceedings of the TAPPI Pulping Process and Product Quality Conference* (Boston, MA, Atlanta, GA, USA, November 2000).

- [91] TABOADA, B., VEGA-ALVARADO, L., CÓRDOVA-AGUILAR, M., GALINDO, E., AND CORKIDI, G. Semi-automatic image analysis methodology for the segmentation of bubbles and drops in complex dispersions occurring in bioreactors. *Experiments in Fluids* 41 (2006), 383–392.
- [92] THEODORIDIS, S., AND KOUTROUMBAS, K. *Pattern Recognition*. Academic Press, 1999.
- [93] TONG, W.-S., TANG, C.-K., MORDOHAI, P., AND MEDIONI, G. First order augmentation to tensor voting for boundary inference and multiscale analysis in 3D. *IEEE Transactions on Pattern Analysis and Machine Intelligence*, 26, 5 (2004), 594–611.
- [94] TREPANIER, R. Automatic fiber length and shape measurement by image analysis. *TAPPI Journal* 81 (1998), 152–154.
- [95] VIOLA, P., AND JONES, M. Rapid object detection using a boosted cascade of simple features. In *Proceedings of the IEEE Conference on Computer Vision and Pattern Recognition, CVPR* (Kauai, HI, USA, December 2001), pp. 511–518.
- [96] WEDEL, A., POCK, T., BRAUN, J., FRANKE, U., AND CREMERS, D. Duality tv-11 flow with fundamental matrix prior. 1–6.
- [97] WEI, L. Y., AND LEVOY, M. Fast texture synthesis using tree-structured vector quantization. In *Proceedings of the 27th Annual Conference on Computer Graphics and Interactive Techniques* (New Orleans, LA, USA, 2000), pp. 479–488.
- [98] WIKLUND, J., PETERSSON, J., RASMUSON, A., AND STADING, M. A Comparative Study Between UVP and LDA Techniques For Highly Concentrated Pulp Suspensions in Pipe Flow. In *Proceedings of the 4th International Symposium on Ultrasonic Doppler Method for Fluid Mechanics and Fluid Engineering* (Sapporo, Japan, 2004), pp. 69–75.
- [99] WOLBERG, G. *Digital Image Warping*. IEEE Computer Society Press, 1990.
- [100] XIAO, J., CHENG, H., SAWHNEY, H., RAO, C., AND ISNARDI, M. Bilateral filtering-based optical flow estimation with occlusion detection. 211–224.
- [101] XU, H., AND AIDUN, C. Velocity profile of fiber suspension flow in a channel. In *Proceedings of the TAPPI Engineering/Finishing and Converting Conference* (San Antonio, TX, September 2001), pp. 357–359.
- [102] YANG, Q., WANG, J., LIU, Z., AND BAO, F. Application of median filtering on PIV images analysis. In *Proceedings of the 2011 International Conference on Computer Science and Service System, CSSS* (Xiamen, China, June 2011), pp. 2108–2111.
- [103] YOUNG, D. The Circular Hough Transform Matlab toolbox [online]. Available: <http://www.mathworks.com/matlabcentral/fileexchange/9168>. Accessed 2012-07-14.
- [104] YUEN, H. K., PRINCEN, J., ILLINGWORTH, J., AND KITTLER, J. Comparative study of hough transform methods for circle finding. *Image and Vision Computing* 8, 1 (1990), 71–77.
- [105] ZABULIS, X., PAPARA, M., CHATZIARGYRIOU, A., AND KARAPANTSIOS, T. D. Detection of densely dispersed spherical bubbles in digital images based on a template matching technique. application to wet foams. *Colloids and Surfaces A: Physicochemical and Engineering Aspects*, 309 (1-3) (2007), 96–106.

- 
- [106] ZEYER, C., VENDITTI, R., AND PUANGCHINDA, K. The distribution of impurities in pulp and paper - the effects of the random distribution of impurities on image analysis. *TAPPI Journal* 78 (1995), 168–175.
- [107] ZHANG, J., FIEGUTH, P., AND WANG, D. Random field models. *Handbook of Image and Video Processing* (2000), 301–312.
- [108] ZIYUN, L., AND WEI, L. The Compensated HS Optical flow Estimation Based on Matching Harris Corner Points. In *2010 International Conference on Electrical and Control Engineering, ICECE* (Hefei, China, June 2010), pp. 2279–2282.



## ACTA UNIVERSITATIS LAPPEENRANTAENSIS

502. KUTVONEN, ANTERO. Strategic external deployment of intellectual assets. 2012. Diss.
503. VÄISÄNEN, VESA. Performance and scalability of isolated DC-DC converter topologies in low voltage, high current applications. 2012. Diss.
504. IKONEN, MIKA. Power cycling lifetime estimation of IGBT power modules based on chip temperature modeling. 2012. Diss.
505. LEIVO, TIMO. Pricing anomalies in the Finnish stock market. 2012. Diss.
506. NISKANEN, ANTTI. Landfill gas management as engineered landfills – Estimation and mitigation of environmental aspects. 2012. Diss.
507. QIU, FENG. Surface transformation hardening of carbon steel with high power fiber laser. 2012. Diss.
508. SMIRNOV, ALEXANDER. AMB system for high-speed motors using automatic commissioning. 2012. Diss.
509. ESKELINEN, HARRI, ed. Advanced approaches to analytical and systematic DFMA analysis. 2013.
510. RYNNÄNEN, HARRI. From network pictures to network insight in solution business – the role of internal communication. 2013. Diss.
511. JÄRVI, KATI. Ecosystem architecture design: endogenous and exogenous structural properties. 2013. Diss.
512. PIILI, HEIDI. Characterisation of laser beam and paper material interaction. 2013. Diss.
513. MONTO, SARI. Towards inter-organizational working capital management. 2013. Diss.
514. PIRINEN, MARKKU. The effects of welding heat input usability of high strength steels in welded structures. 2013. Diss.
515. SARKKINEN, MINNA. Strategic innovation management based on three dimensions diagnosing innovation development needs in a peripheral region. 2013. Diss.
516. MAGLYAS, ANDREY. Overcoming the complexity of software product management. 2013. Diss.
517. MOISIO, SAMI. A soft contact collision method for real-time simulation of triangularized geometries in multibody dynamics. 2013. Diss.
518. IMMONEN, PAULA. Energy efficiency of a diesel-electric mobile working machine. 2013. Diss.
519. ELORANTA, LEENA. Innovation in a non-formal adult education organisation – multi-case study in four education centres. 2013. Diss.
520. ZAKHARCHUK, IVAN. Manifestation of the pairing symmetry in the vortex core structure in iron-based superconductors. 2013. Diss.
521. KÄÄRIÄINEN, MARJA-LEENA. Atomic layer deposited titanium and zinc oxides; structure and doping effects on their photoactivity, photocatalytic activity and bioactivity. 2013. Diss.
522. KURONEN, JUHANI. Jatkuvan äänitehojakautuman algoritmi pitkien käytävien äänikenttien mallintamiseen. 2013. Diss.

523. HÄMÄLÄINEN, HENRY. Identification of some additional loss components in high-power low-voltage permanent magnet generators. 2013. Diss.
524. SÄRKKÄ, HEIKKI. Electro-oxidation treatment of pulp and paper mill circulating waters and wastewaters. 2013. Diss.
525. HEIKKINEN, JANI. Virtual technology and haptic interface solutions for design and control of mobile working machines. 2013. Diss.
526. SOININEN, JUHA. Entrepreneurial orientation in small and medium-sized enterprises during economic crisis. 2013. Diss.
527. JÄPPINEN, EERO. The effects of location, feedstock availability, and supply-chain logistics on the greenhouse gas emissions of forest-biomass energy utilization in Finland. 2013. Diss.
528. SÖDERHOLM, KRISTIINA. Licensing model development for small modular reactors (SMRs) – focusing on the Finnish regulatory framework. 2013. Diss.
529. LAISI, MILLA. Deregulation's impact on the railway freight transport sector's future in the Baltic Sea region. 2013. Diss.
530. VORONIN, SERGEY. Price spike forecasting in a competitive day-ahead energy market. 2013. Diss.
531. PONOMAREV, PAVEL. Tooth-coil permanent magnet synchronous machine design for special applications. 2013. Diss.
532. HIETANEN, TOMI. Magnesium hydroxide-based peroxide bleaching of high-brightness mechanical pulps. 2013. Diss.
533. TYKKÄLÄ, TOMMI M. Real-time image-based RGB-D camera motion tracking and environment mapping. 2013. Diss.
534. PEKKOLA, SANNA. Performance measurement and management in a collaborative network. 2013. Diss.
535. PANOREL, IRIS CHERRY. Pulsed corona discharge as an advanced oxidation process for the degradation of organic compounds in water. 2013. Diss.
536. TORKKELI, LASSE. The influence of network competence of internationalization of SMEs. 2013. Diss.
537. MOLANDER, SOLE. Productivity and services – safety telephone services for the elderly. 2013. Diss.
538. SITARZ, ROBERT. Identification of research trends in the field of separation processes. Application of epidemiological model, citation analysis, text mining, and technical analysis of the financial markets. 2013. Diss.
539. KATTEDEN, KAMIEV. Design and testing of an armature-reaction-compensated permanent magnet synchronous generator for island operation. 2013. Diss.
540. HÄMÄLÄINEN, HARRI. Integration of learning supportive applications to development of e-portfolio construction process. 2013. Diss.
541. RATCHANANUSORN, WARIN. Development of a process for the direct synthesis of hydrogen peroxide in a novel microstructured reactor. 2013. Diss.
542. PERFILEV, DANIIL. Methodology for wind turbine blade geometry optimization. 2013. Diss.

